EXPERIMENTAL CHARACTERIZATION OF THERMAL TRANSPORT IN TWO-DIMENSIONAL MATERIALS AND THIN FILMS

A Dissertation
Presented to
The Academic Faculty

by

David Brandon Brown

In Partial Fulfillment
of the Requirements for the Degree
Doctor of Philosophy in the
The George W. Woodruff School of Mechanical Engineering

Georgia Institute of Technology
May 2019

EXPERIMENTAL CHARACTERIZATION OF THERMAL TRANSPORT IN TWO-DIMENSIONAL MATERIALS AND THIN FILMS

Approved by:

Dr. Satish Kumar, Co-Advisor
George W. Woodruff School of Mechanical Engineering
Georgia Institute of Technology

Dr. Baratunde A. Cola, Co-Advisor
George W. Woodruff School of Mechanical Engineering
Georgia Institute of Technology

Dr. Samuel Graham
George W. Woodruff School of Mechanical Engineering
Georgia Institute of Technology

Dr. Eric M. Vogel
School of Materials Science and Engineering
Georgia Institute of Technology

Dr. Matthew McDowell
George W. Woodruff School of Mechanical Engineering
Georgia Institute of Technology

Date Approved: January 10, 2019

To my parents

ACKNOWLEDGEMENTS

First and foremost, I would like to thank the Most High God for blessing me with the opportunity to complete this work in such an exciting field of research. I would like to thank my advisor Dr. Satish Kumar for his guidance and support throughout my time in the Woodruff school. Dr. Kumar showed great patience as I found my way as a researcher and faced experimental struggles early on. I am extremely grateful, and I hope that I can extend that quality to other aspects of my professional and personal life. I would also like to thank my co-advisor Dr. Baratunde Cola for helping me navigate graduate school while keeping in mind "the big picture". His enthusiasm for science is inspiring and I am glad I was able to work so closely with him. I would like to thank Dr. Samuel Graham for serving on my thesis committee and for many discussions about research and life. A special thank you to my additional committee members Dr. Matthew McDowell and Dr. Eric Vogel for their valuable input to this thesis.

I would like to thank my outside collaborators: Xiang Zhang and Dr. Pulickel Ajayan at Rice University, and Dr. Xufan Li, Dr. Kai Xiao, and Dr. David B. Geohegan from Oak Ridge National Lab. I could not have completed this work without my colleagues at Georgia Tech. A very special thank you to Dr. Thomas Bougher for helping me learn TDTR in the early days of our setup. A special thank you to the MiNDS Lab members: Dr. Man Prakash Gupta, Dr. Liang Chen, Dr. Banafsheh Barabidi, Dr. Zhequan Yan, Dr. Jialuo Chen, Wenqing Shen, Nitish Kumar, Matthew Redmond, Owen Sullivan, and Matthew Barry. A special thank you to the NEST Lab members: Dr. Matthew Smith, Eric Tervo, Zhe Cheng, Daron Spence, and Erik Anderson. Thank you to EMRL lab members: Dr.

Georges Pavlidis, Dr. Wale Odukomaiya, Luke Yates, and Nick Hines. A special thank you to Neha Kondekar. I also want to thank the cleanroom staff: Dr. Mikkel Thomas, Charlie (Suh), Ben, Vinny, Devin, Walter, Rathi, Eric, and Charlie (Turgeon). Thank you to the ME staff members: Glenda Johnson and Camellia Henry. To the many others I am forgetting, I appreciate our interactions and thank you.

Next, I would like to thank my support system outside of academia. I was blessed to be able to complete my PhD in my hometown of Atlanta, GA surrounded by friends and family. I was not always available to them, but they always understood and continued to support me. There are too many people to name, but I would like to thank them all! A special thank you to my big brother Jonathan for continuing to be a positive role model.

Finally, I would like to thank my parents for their unconditional love, support, and for belief in me. I want to thank my mother for her kindness and her selflessness throughout my life. I want to thank my father for challenging me and teaching me how to be a man. I would not be where I am today without them. Words cannot express how much love and appreciation I have for them.

TABLE OF CONTENTS

LIST OF TABLES

LIST OF FIGURES

LIST OF SYMBOLS AND ABBREVIATIONS

Symbols

A	Laser power
C	Volumetric heat capacity
c_p	Specific heat
d	Thin film thickness
D	Thermal diffusivity
E	Energy
f	Modulation frequency
$f(E)$	Fermi-Dirac probability distribution function
$f(\omega)$	Bose-Einstein probability distribution function
g	Frequency-domain thermal response
G	Hankel transform of frequency-domain thermal response
G_{T}	Total thermal conductance of a thin film
G_{TBC}	Combined interfacial thermal conductance
$\hbar$	Reduced Planck's constant
H	Phonon irradiance
k	Thermal conductivity, wave vector
k_B	Boltzmann constant
k_D	Debye cutoff wave vector
k_{eff}	Effective thermal conductivity
k_{i}	Intrinsic thermal conductivity
l	Thermal penetration depth

L_{K}	Kapitza length
N	Number of atoms in primitive unit cell
p	Gaussian intensity distribution of pump beam
Q''	Heat flux
r	Radial coordinate
R	Reflectivity
s	Hankel transform variable
S_p	Sensitivity to parameter in TDTR experiments
t	Probe delay time
T	Temperature
TBC	Thermal boundary conductance
U	Internal energy
v	Carrier velocity
v_s	Speed of sound
V	Total lock-in amplifier voltage
$\cancel{V}$	Volume
V_{in}	In-phase lock-in amplifier signal
V_{out}	Out-of-phase lock-in amplifier signal
w_0	Radius of pump beam
w_1	Radius of probe beam
x	Dimensionless phonon energy

Greek Symbols

α	Phonon transmission coefficient
Δ	Delta
Γ	Gamma point of first Brillouin zone
λ	Wavelength
Λ	Mean free path
K	K point of first Brillouin zone
μ	Chemical potential
ω	Angular frequency
π	Pi (constant)
ρ	Density
σ	Electrical conductivity
τ	Period of TDTR laser
θ	Temperature rise in TDTR experiment
θ_D	Debye temperature

Abbreviations

2D	Two-dimensional
A-DMM	Anisotropic diffuse mismatch model
AFM	Atomic force microscope
AGF	Atomistic Green’s function
ALD	Atomic layer deposition
AMM	Acoustic mismatch model

CMOS	Complementary metal-oxide-semiconductor
CVD	Chemical vapor deposition
DFT	Density functional theory
DMM	Diffuse mismatch model
DOS	Density of states
FBZ	First Brillouin zone
FDTR	Frequency-domain thermoreflectance
FET	Field-effect transistor
FFT	Fast Fourier transform
HOPG	Highly-oriented pyrolytic graphite
LA	Longitudinal acoustic mode
LO	Longitudinal optical mode
LPCVD	Low-pressure chemical vapor deposition
MC	Monte Carlo
MD	Molecular dynamics
M-G	Metal-graphene
M-G-M	Metal-graphene-metal
M-M	Metal-metal
MTL	Maximum transmission limit
PDMS	Polydimethysiloxane
PMMA	Poly(methyl methacrylate)
PWA-DMM	Piecewise anisotropic diffuse mismatch model
RL	Radiation limit
RT	Room temperature
SLG	Single-layer graphene

SThM	Scanning thermal microscopy
TA	Transverse acoustic mode
TBC	Thermal boundary conductance
TDTR	Time-domain thermoreflectance
TL1	Recomposed ellipsoidal quasi-TA phonon mode
TL2	Recomposed ellipsoidal quasi-LA phonon mode
TMD	Transition metal dichalcogenide
TEM	Transmission electron microscope
TO	Transverse optical phonon mode
XPS	X-ray photoelectron spectroscopy
ZA	Flexural acoustic phonon mode
ZO	Flexural optical phonon mode

SUMMARY

Increased power density in modern microelectronics has led to thermal management challenges which degrade performance and reliability. The power consumption and heat removal are limited by the thermal boundary conductance (TBC) at the interfaces of dissimilar materials and the change in properties such as thermal conductivity and heat capacity for thin films at the nanoscale. New materials such as two-dimensional (2D) graphene and transition metal dichalcogenides (TMDs) are being investigated for applications in next generation devices, but the interfaces will play a critical role in the overall performance of these materials. In addition, high dielectric constant insulators such as hafnia (HfO_2) are promising for many future applications, and the impact of the thermal properties cannot be overlooked. A fundamental understanding and precise characterization of the thermal transport properties at the interfaces and in the bulk of these materials is of the utmost importance to ensure energy efficient operation and long lifetime in future electronic devices.

In this work, time-domain thermoreflectance (TDTR) is used to explore the TBC at metal-graphene interfaces. Transition metals Ti and Ni have been categorized as having a strong interaction with graphene and are expected to exhibit high TBC, but this was not observed due to formation of native oxide layer on the surface. The native oxide also reduced the TBC well below what is observed for the electron dominated metal-metal interfaces. In addition, the insertion of single-layer graphene significantly diminished the electronic contribution at Au-Au interfaces. The results highlight important design considerations for metal-graphene-metal interfaces in future devices. The interfaces of 2D

hexagonal boron nitride (h-BN) and graphene were investigated using TDTR. The phonon transmission and TBC were calculated using two forms of the diffuse mismatch model for highly anisotropic materials. The findings of this investigation include experimental estimation of TBC and contributions of different phonon modes to transmission at h-BN-graphene interface.

The spatial variation of TBC at interface of the 2D semiconducting TMD $MoSe_2$ and metal was demonstrated using a modified TDTR technique. The results indicate enhanced TBC at Ti-$MoSe_2$ interface compared to Al-$MoSe_2$. Additionally, image clustering revealed increased TBC in single-layer regions compared to bilayer. Both findings are crucial to the design and performance of next generation devices featuring $MoSe_2$. Finally, the thermal conductivity and heat capacity of HfO_2 films of varying thickness was estimated using TDTR. A 20% reduction in bulk heat capacity observed for a 215 nm layer compared to thinner films is attributed to density differences originating from combined amorphous and crystalline film composition. The thickness-independent thermal conductivity of HfO_2 layers from 12 to 215 nm was observed and the measured conductivity was close to the bulk value, a vital observation for the design and performance of electronic devices in the future.

CHAPTER 1. INTRODUCTION

This chapter introduces the relevant properties and potential applications of the materials that are the subject of this dissertation. First, two-dimensional materials are featured with an emphasis on graphene, hexagonal boron nitride, and transition metal dichalcogenides. Next, the allure of thin film hafnia is discussed, followed by the motivation for this work. The chapter concludes with the overall objectives and outline of the dissertation.

1.1 Two-Dimensional Materials

1.1.1 Graphene

The isolation of stable, two-dimensional (2D) crystals [1] began a revolution in condensed matter physics and materials science. Graphene, a single-layer of sp^2 bonded C atoms in a honeycomb lattice, has been studied extensively since its fabrication was made practical by mechanical exfoliation from highly-oriented pyrolytic graphite (HOPG) [2]. A 2D semimetal [3], graphene has been an area of intense research over the past decade attracting immense interest because of its exceptional electrical and thermal transport properties. High intrinsic carrier mobilities of 10^4 cm^2/V-s have been reported for suspended graphene with an order of magnitude increase in some samples [4-7]. In-plane thermal conductivities up to 5000 W/m-K have also been reported for suspended graphene at room temperature (RT) [8-10], in a similar range with individual carbon nanotubes [11-13] and higher than the best bulk thermal conductor, diamond [14-16]. Figure 1-1(a) shows a schematic of the suspended geometry used to measure intrinsic thermal conductivity of graphene with Raman spectroscopy [8]. As a result, graphene has become a promising candidate for applications in next generation nanoelectronic devices.

Graphene field-effect transistors (FETs) have been demonstrated [17-23] with cutoff frequency up to GHz range. Lin et al. [19] reported FETs with 100 GHz frequency from epitaxial graphene on a SiC substrate. The study was extended to fabricate the radio-frequency mixers with 10 GHz cutoff frequency as shown in Figure 1-1(b) [21]. Cheng et al. [22] fabricated graphene transistors with frequency up to 427 GHz. The lack of intrinsic bandgap in graphene sheets make it more suitable for analog and radio-frequency

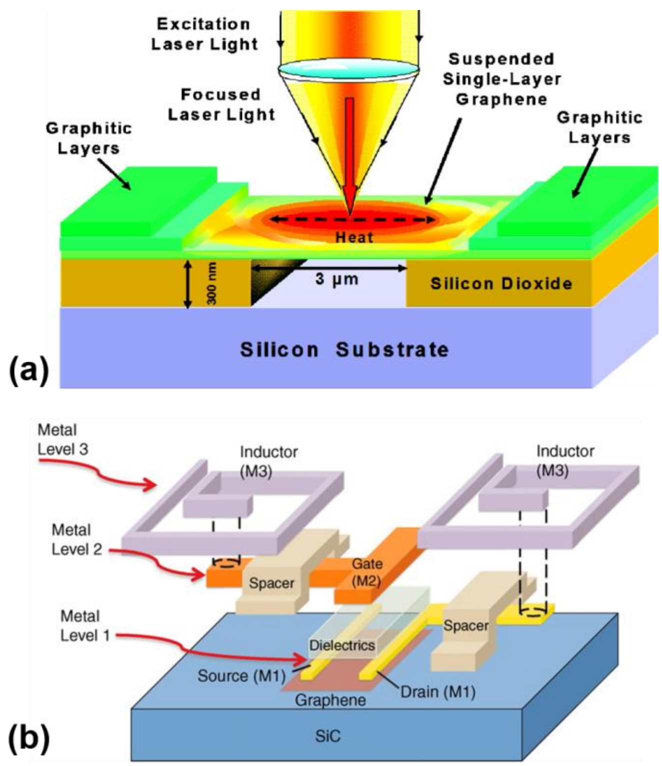

Figure 1-1 (a) Graphical representation of thermal conductivity measurement on suspended graphene layer. Thermal conductivity of ~5,000 W/m-K is the highest room temperature measurement for any material, comparable with carbon nanotubes and higher than best bulk thermal conductor diamond [8]. Copyright 2008 American Chemical Society. (b) Schematic of wafer-scale graphene radio-frequency mixer with up to 10 GHz cutoff frequency and good thermal stability [21]. Copyright 2011 American Association for the Advancement of Science.

transistors rather than logic applications [24-26], but graphene nanoribbons have been shown to overcome this deficiency [27-29]. The atomic force microscope image in Figure 1-2(a) shows a single-layer graphene nanoribbon (GNR) from Li et al. [28]. Properties of FETs fabricated from these similar GNRs are shown in Figure 1-2(b) and (c). ON-OFF ratios up to 10^7 were achieved at RT for sub-10 nm GNRs despite significant reduction in mobility. The combination of optical transparency [30-32], large mechanical strength [33, 34], and high electrical conductivity make graphene a potential transparent electrode material [35-38]. Kim et al. showed graphene with sheet resistance 280 Ω/□ and 80% transparency for transparent electrodes on flexible PDMS substrates [36]. High bandwidth photodetectors based on graphene have also been demonstrated [39-42], but the photoresponse is ultimately limited by its zero bandgap and low absorption. Graphene has

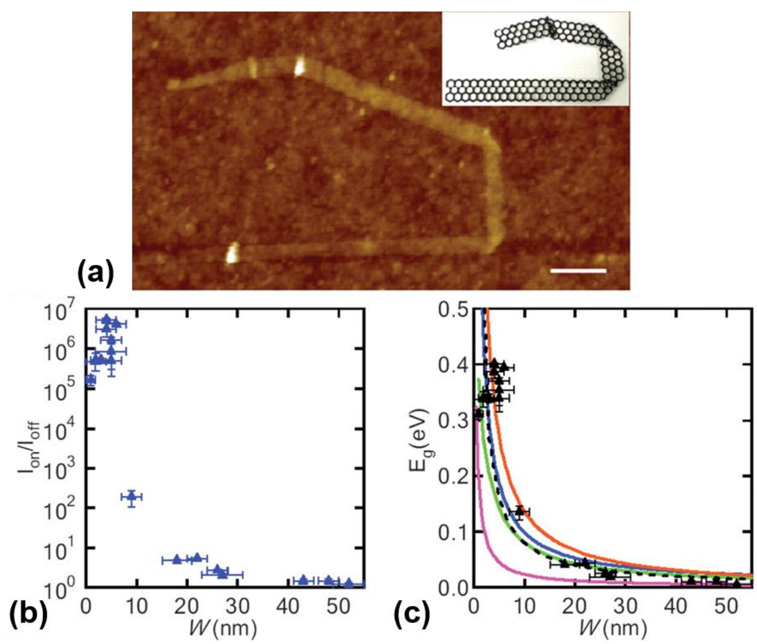

Figure 1-2 (a) Optical microscope image of single-layer graphene nanoribbons with schematic drawing shown in the inset. (b) Graphene nanoribbons in FET application showed improved ON-OFF ratio and (c) increased bandgap with decreasing nanoribbon width [28]. Copyright 2008 American Association for the Advancement of Science.

also been utilized in Li ion batteries [43, 44] showing the potential applications of graphene are virtually limitless.

1.1.2 Hexagonal Boron Nitride

Graphene can be combined with other 2D materials such as insulating hexagonal boron nitride (h-BN) or transition metal dichalcogenides (TMDs) like molybdenum disulfide (MoS_2) or tungsten disulfide (WS_2) to build layered, van der Waals heterostructures [45-57]. Figure 1-3(a) displays structure and stacking arrangement of 2D graphene, h-BN, and TMDs. These hybrid heterostructures introduce compositional and structural diversities to further enrich the properties and applications of 2D materials [58-60]. For example, the choice of supporting substrate is crucial to exploit graphene's intrinsic properties observed in the suspended geometry [61, 62] and maximize the performance of future devices. Surface charges and impurities, roughness, and surface

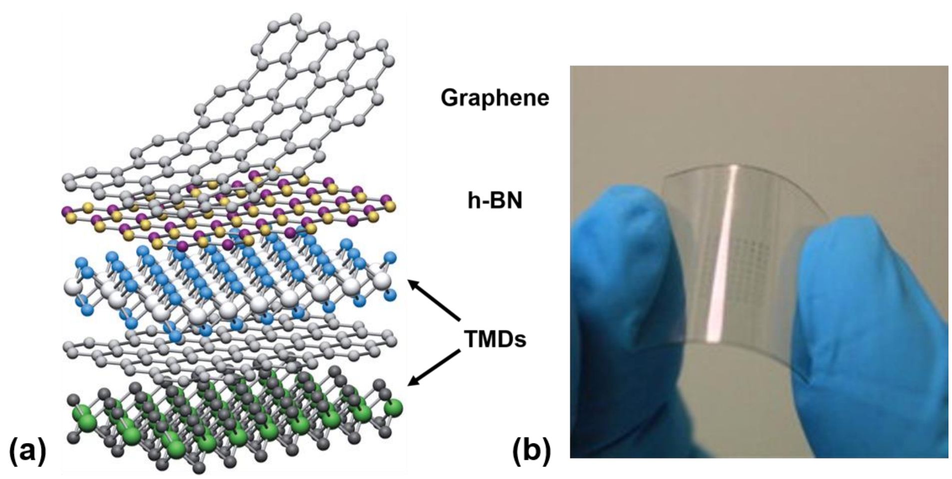

Figure 1-3 (a) Visual depiction of 2D materials graphene, h-BN, and semiconducting TMDs ($MoSe_2$, WSe_2) for van der Waals heterostructures. Adapted from [58]. Copyright 2013 Macmillan Publishers Limited. (b) 2D materials were used to construct flexible, transparent thin film transistor with graphene electrodes, h-BN gate dielectric, and WSe_2 channel on polymer (PET) substrate, a promising application for 2D van der Waals heterostructures [56]. Copyright 2014 American Chemical Society.

optical phonons in SiO_2 and similar substrates limits the mobility of graphene devices [63-68]. h-BN has diatomic (B and N), planar lattice structure nearly identical to graphene making it a promising substrate for graphene-based devices owing to its atomically smooth surface and small lattice mismatch (~1.7%) with graphene [69, 70], large bandgap [71], and comparable dielectric properties to SiO_2 [72]. Improved mobility of FET's channel compared to SiO_2 has been observed in several studies [45, 46, 48] which emphasizes the impact of material selection on the performance of graphene devices.

For graphene transistors, ON-OFF ratio is hindered by its small intrinsic bandgap limiting its application for logic devices [24-26]. Graphene/h-BN and graphene/TMD heterostructures showed improved ON-OFF ratio in FET operation due to quantum tunneling [47, 49, 51]. Britnell et al. [47] reported an order of magnitude increase in ON-OFF ratio for a graphene/h-BN heterostructure with ON-OFF ratio of ~10,000 in a graphene/MoS_2 device. In addition, graphene electrodes were implemented in flexible devices featuring semiconducting WS_2 (direct bandgap of 2.0 eV in monolayer form [73]) as the channel material to achieve ON-OFF ratio of 10^6 [47]. A flexible, transparent WSe_2 transistor (Figure 1-3(b)) with graphene electrodes and h-BN gate dielectric was fabricated on polyethylene terephthalate (PET) substrate [56] and maintained device characteristics for up to 2% in-plane strain. The thermoelectric properties of graphene/h-BN heterostructures have also been investigated [74, 75], and though efficiency is low, the thermionic response may play a role in other applications of these devices. Also, the weak van der Waals interaction between stacked 2D layers may invoke additional phonon scattering reducing the thermal conductivity, k, which is desired to boost the figure of merit, $ZT \propto 1/k$, for thermoelectric devices.

1.1.3 Transition Metal Dichalcogenides

The absence of a bandgap in pristine graphene has led to increased interest in other 2D materials. Transition metal dichalcogenides (TMDs) with the chemical formula MX_2 (M = transition metal atom, X = chalcogen) [76, 77] exhibit a range of properties covering the full spectrum from insulators (HfS_2), semiconductors (MoS_2, WSe_2, $MoSe_2$), semimetals (WTe_2, $TiSe_2$), to metals (NbS_2, VSe_2) [78]. Many exist as layered structures with hexagonal lattice, but unlike planar graphene and h-BN, the metal atoms are sandwiched between two layers of chalcogen atoms. TMDs with semiconducting properties, such as MoS_2, are promising for many applications including field-effect transistors [79-82] and optoelectronic devices [83-86].

MoS_2 has a direct bandgap of 1.8 eV in single layer form [87-89], and multilayer MoS_2 transistors have displayed high carrier mobility of 700 cm^2/V-s [82] with ON-OFF current ratios of 10^7-10^8 [80, 81] for MoS_2 layers of varying thickness. In addition, the strong photoluminescence [88-90] make it attractive for optical applications, and the thickness-dependent bandgap can be used to tune the photoresponse as illustrated by the schematic in Figure 1-4 for a top-gated MoS_2 phototransistor [83]. Monolayer MoS_2 photodetectors with very high photoresponsivity of 880 A/W [84] up to 2200 A/W [85] have already been demonstrated. $MoSe_2$ is another promising TMD with similar properties [88, 89, 91] and applications [92-96] as MoS_2. In the solar spectrum, the optical response of $MoSe_2$ is expected to be greater than MoS_2 [88, 97], thus, making it the TMD of choice for applications such as solar cells. The large Seebeck coefficient of TMDs has also created interest in thermoelectric applications [98-101].

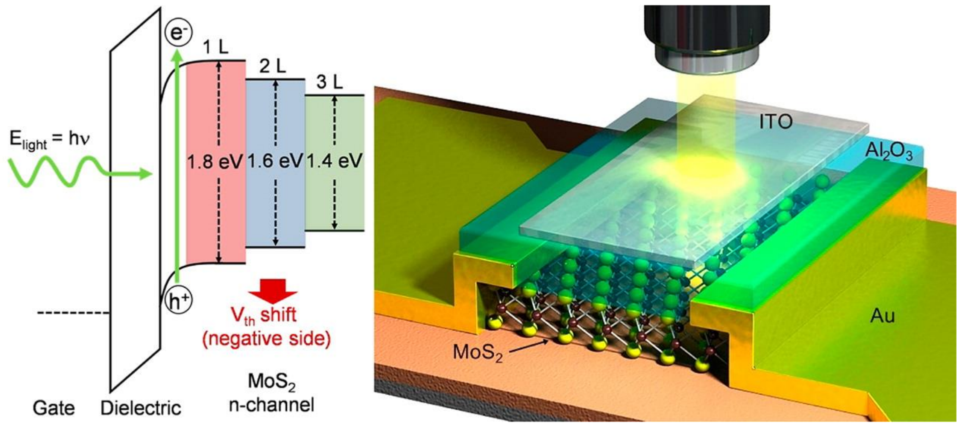

Figure 1-4 Top-gated MoS_2-based phototransistor with transparent gate electrode. Thickness-dependent mobility and bandgap of MoS_2 (or $MoSe_2$) enables application-specific modulation of the photoresponse [83]. Copyright 2012 American Chemical Society.

1.1.4 Xenes and other 2D Materials

Interest in the 2D material class known as Xenes has increased dramatically in recent years. The monoatomic 2D-Xenes comprised of group IV elements (X = P, Si, Ge, Sn) termed phosporene (i.e., monolayer black phosphorus), silicene, germanene, and stanene are arranged in a honeycomb lattice like graphene and h-BN [102-104]; however, the increased atomic distance causes in-plane buckling or puckering (in the case of phosphorene) resulting in highly anisotropic transport properties. Layered bulk materials composed of silicene and germanene, while more technologically relevant, do not exist. Instead, they are grown epitaxially from metal substrates [105-109] and suffer from air stability issues [110, 111] making experimental study a more arduous task. Despite, silicene FETs with mobility of 100 cm^2/V-s were demonstrated experimentally [112].

On the other hand, bulk black phosphorus is a stable, layered material similar to graphite and phosphorene layers have recently been exfoliated for experimental studies [113-115]. Phosphorene has a band gap of 1.5 eV in monolayer form compared to 0.33 eV for bulk black phosphorus [116, 117]. Carrier mobility of up to 1000 cm^2/V-s and ON-OFF ratio of 10^5 at RT has been observed in few-layer black phosphorus [118] which is higher than TMDs. The thickness dependent bandgap make tunable photodetection another promising application [119, 120]. Other 2D material classes include group IV monochalcogenides (SnS, GeS, GaS, etc.) [121-124], transition metal and complex metal oxides (MoO_3, V_2O_5, CoO_2, $Bi_2Sr_2Co_2O_8$) [125-128], and transition metal carbides, carbonitrides, nitrides collectively termed MXenes [129-132]. Overall, the field of 2D materials is still in its infancy and will continue into the distant future as new materials and applications are continuously being discovered.

1.2 Thin Film Hafnia

Scaling of the gate dielectric in complementary metal-oxide-semiconductor (CMOS) FETs has followed Moore's law [133] for transistors, and recently issues arose with increased power dissipation and reliability [134-137]. The dielectric of choice had been SiO_2 which in turn propelled Si, along with its ubiquity, to the forefront of all CMOS devices because of desirable properties of bulk thermal SiO_2 as well as the Si-SiO_2 interface. Fundamental limits have been achieved whereby increased leakage current across SiO_2 make additional scaling impossible. The solution to this problem lies in high dielectric constant (high-*k*) materials which can maintain the performance of SiO_2 (i.e., high gate capacitance) without the inherent problems associated with its application in an ultrathin geometry [138, 139]. Hafnia (HfO_2) is an essential high-*k* ($k = 25$) transition metal oxide which replaces SiO_2 as the ultrathin gate-dielectric in Si-based FETs with small gate length [140, 141] allowing for use of thicker dielectric layers which reduces leakage current and lowers power consumption in the OFF state.

The family of circuit elements (resistors, capacitors, inductors) grew recently with the "discovery" of the memristor device [142], first theorized by Chua [143] in 1971 and studied by several prior to this [144, 145]. Memristors are two-terminal devices employing metal-insulator-metal geometries whose fundamental operation rely on the migration of charged dopants in the insulator layer (e.g., oxygen vacancies in transition metal oxides [146]) and are promising for many application such as non-volatile memory [147-150] and artificial neural networks [151-154]. HfO_2 has attracted immense interest because of low power and high speed when switching ON and OFF [155-161]. The transmission electron microscope image in Figure 1-5(a) shows an HfO_2-based memristor crossbar with 10x10 nm^2 area. Also, the applicability of HfO_2-based memristors for image processing was recently demonstrated (see Figure 1-5(b)) [162]. In addition, thicker HfO_2 layers are used as optical or thermal coatings because of high refractive index, low absorption, hardness, and thermal stability [163-169].

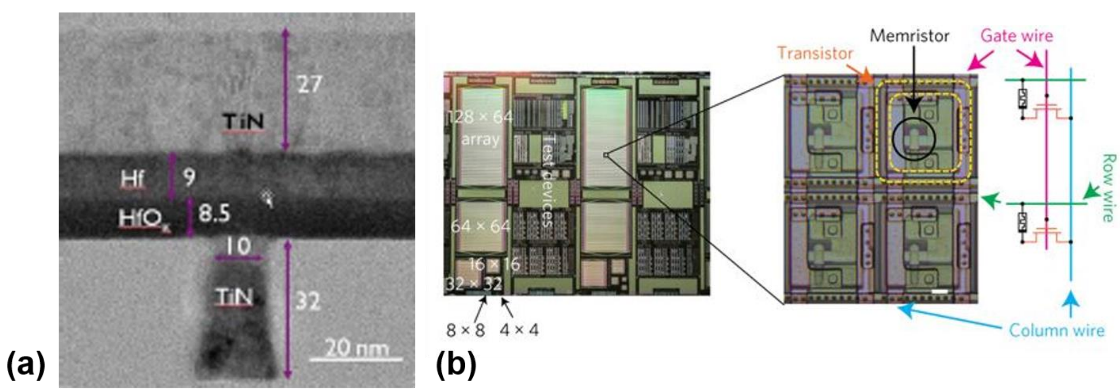

Figure 1-5 (a) Transmission electron microscope image of HfO_2-based memristor crossbars for resistive random-access memory cells fabricated down to 10x10 nm^2 area [157]. Copyright 2011 IEEE. (b) Photograph and microscope image for highlighted area of HfO_2-based, 128x64 memristor crossbar array integrated with metal-oxide-semiconductor transistor to perform image processing [162]. Copyright 2017 Macmillan Publishers Limited.

1.3 Motivation

The volume of research pertaining 2D materials is expansive; however, the thermal properties of 2D materials as well as their interaction with metals-insulators in typical device architectures have received much less attention. In general, the atomically-thin layer thickness of these 2D materials and their heterostructures dictates that the thermal transport across the interfaces (e.g., substrate, metal contacts) will limit heat removal [170-172] but is not completely understood. Thermal management of such devices must be addressed to ensure optimal performance and reliability. A fundamental understanding of thermal transport at these interfaces is of great importance to the design process and is essential for commercial applications to become viable in the future.

The miniaturization of modern electronics has significantly increased the power density which has important implications on device performance and reliability [173]. Elevated temperature and hotspot formation, caused by self-heating within the active region, can reduce battery life and shorten overall device lifetime. New geometries and decreasing film thicknesses makes proper thermal management critical as efficient heat extraction becomes increasingly difficult. Thermal conductivity is less than bulk when critical dimensions become less than mean free path of carriers [174] (e.g., phonons in Si [175-177]) and increased surface area to volume ratio heightens the importance of interfaces. As a result, accurate estimation of thermal properties of electronic materials (e.g., thin films and interfaces) is critical to improve design and analysis of future devices.

1.4 Objectives and Outline of Dissertation

This dissertation is intended to experimentally investigate the thermal transport at the interfaces of 2D materials and the properties of thin film HfO_2. Time-domain thermoreflectance is used to accomplish these goals. The following is the organization of the thesis. Chapter 2 presents the background material which is the foundation for the work. Included are some fundamental heat transfer theory which are vital to thermal properties at the nanoscale and a survey of relevant results in the literature. Also, the meaningful contributions of the current work are summarized. Chapter 3 discusses the experimental technique used to interrogate the samples in this study. The results pertaining to metal-graphene interfaces are included in Chapter 4. The study is extended to h-BN-graphene interfaces, including modelling, in Chapter 5. The spatial variation of thermal boundary conductance at metal-$MoSe_2$ interfaces is presented in Chapter 6. The thermal properties of thin film HfO_2 are examined in Chapter 7. Chapter 8 summarizes the findings presented in this dissertation and discusses the outlook for future work.

CHAPTER 2. BACKGROUND

This chapter discusses the fundamental concepts pertinent to the study of heat transfer at the nanoscale. Focus is given to the thermal properties associated with the conduction of heat in solid materials which dictate the performance of modern microelectronic devices. Next, recent experimental and theoretical work on metal-graphene, h-BN-graphene, and metal-$MoSe_2$ interfaces along with the thermal properties of thin HfO_2 are reviewed. The chapter concludes with a list of contributions of the current work.

2.1 Heat Transfer Fundamentals

Heat conduction in bulk solids is primarily due to low frequency, quantized lattice vibrations called acoustic phonons, so named because they resemble sounds waves. High frequency optical phonons can interact directly with electromagnetic radiation (i.e., photons), but do not contribute much to heat conduction [178-180]. For metals, the electron density is several orders of magnitude larger than typical dielectrics and semiconductors allowing electrons to play a significant role. The thermal conductivity, typically represented by the variable k, quantifies a materials ability to transport heat. Physically, the value represents the thermal power per unit distance per unit temperature, given in units of W/m-K, and is an important metric to the thermal design of electronic devices.

Thermal conductivity is related to the heat flux (Q'') and temperature gradient (∇T) in a solid by the heat diffusion equation [181], $Q'' = -k\nabla T$. A relationship for k is given by kinetic theory [182], $k = \frac{1}{3}Cv\Lambda$, where C is volumetric heat capacity (the product of mass density and specific heat, ρc_p), v is the average carrier velocity, and Λ is the carrier mean free path. Amorphous solids typically have low carrier mean free path and thus low thermal conductivity compared to crystalline solids. For comparison, the amorphous dielectrics SiO_2 (1.3 – 1.4 W/m-K) and HfO_2 (1.1 W/m-K) [183] have relatively low thermal conductivities compared to single crystal Si (~150 W/m-K [184]). Metals such as Cu and Ag have thermal conductivities of near 400 W/m-K [185]. Carbon allotropes diamond (2000 – 3000 W/m-K [14-16]) and graphite (2000 W/m-K, in-plane [186]) have the highest thermal conductivity of bulk materials, owing to the extremely light C atoms along with very strong atomic bonding which increases carrier velocity and mean free path.

At the interface of two dissimilar materials the total interface conductance is the combined contribution of two components: the thermal contact conductance and the thermal boundary conductance (TBC). Both are typically expressed in units of MW/m^2-K, or thermal power per unit temperature per unit area. The difference between the two quantities is illustrated in Figure 2-1(a) and (b). The thermal contact conductance [187, 188] is related to the mechanical quality (e.g., roughness) of the interface which, from a microscopic perspective, impedes heat flow by significantly reducing the contact area between the solids. The contact area of macroscopically smooth surfaces is generally less than 1% of the apparent area, and the remaining area is filled with low thermal conductivity air (0.026 W/m-K). The contact conductance is difficult to measure, but it is generally several orders of magnitude larger than the TBC. For materials in "perfect" contact, the TBC, or Kapitza conductance [189-191], arises from the difference in vibrational properties of the two materials. There can also be atomic mixing at "perfect' interfaces. As a result, a temperature drop, ΔT, will be experienced at the interface. This temperature drop

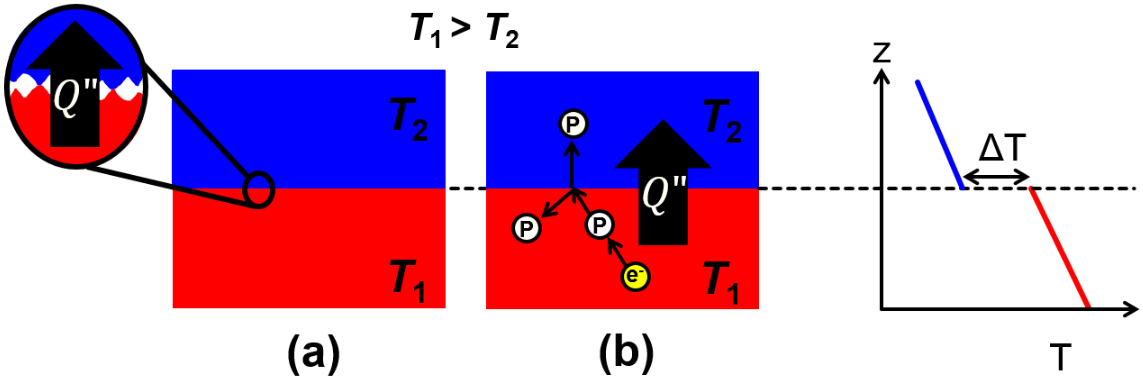

Figure 2-1 (a) Microscale surface roughness reduces the contact area creating a temperature drop, thus, limiting the total heat transport at the interface between two materials. This contribution to the total thermal conductance is termed thermal contact conductance. (b) At "perfect" interfaces, the difference in vibrational properties, and atomic scale mixing, is also a limiting factor. Incoming phonons are scattered giving rise to a temperate difference across the interface. This component of the total thermal conductance is known as the thermal boundary conductance.

is proportional to the heat flux across the interface, $Q'' = TBC \cdot \Delta T$, and the TBC is the constant of proportionality. Typical values of TBC range are on the order of 10^1 – 10^2 MW/m^2-K for phonon-dominated metal-dielectric and metal-semiconductor interfaces [192-194] at RT but can be as high as 10^3 MW/m^2-K for electron-dominated metal-metal interfaces [195, 196].

In addition to transport within the bulk and across the interfaces, solids possess an innate ability to store thermal energy [185]. The volumetric heat capacity, C, measures this ability in units of J/m^3-K, or the energy per unit temperature per unit volume. The heat capacity for solids (and liquids) is on the order of 10^6 J/m^3-K. The heat capacity is defined as, $C = \frac{1}{V\!\!\!/}\left(\frac{\partial U}{\partial T}\right)_{V\!\!\!/}$, where U is average internal energy of the material and $V\!\!\!/$ is volume [178]. In general, as with thermal conductivity, the heat capacity can include contributions from phonons and electrons. Statistical thermodynamics relates the allowable quantum states of energy carriers (i.e., phonons and electrons) to the macroscopic properties of matter (e.g., heat capacity) through the probability distribution function of the carriers [180]. The allowable quantum states of the energy carriers vary for every material and are given by the dispersion relations, and the density of states (DOS) is the total number of allowable states per unit volume per unit energy interval.

As an example, Figure 2-2(a) plots the phonon dispersion of graphite along the high symmetry Γ→K direction of the first Brillouin zone (FBZ) [197]. Phonons follow a Bose-Einstein distribution, $f(\omega) = \frac{1}{\exp(\hbar\omega/k_B T)-1}$, where ω is angular frequency and $\hbar$ and k_B are the reduced Planck's constant and Boltzmann constants, respectively, while electrons follow a Fermi-Dirac distribution, $f(E) = \frac{1}{\exp[(E-\mu)/k_B T]+1}$, where E in energy and μ is a property called the chemical potential [179]. Both functions give the probability of finding an energy carrier at a given energy level in a system at equilibrium temperature, T. Relationships for the internal energy and, thus, the heat capacity of electrons and phonons have been given elsewhere [178-180]. The previous discussion was merely intended to illustrate the origin of these properties. The heat capacity of graphite was calculated [179, 198] and plotted in Figure 2-2(b) along with published values from Desorbo et al. [199] and Bergman et al. [185] to show the accuracy with which macroscopic properties can be determined from the quantum phenomena. The thermal conductivity and heat capacity can be combined to define the thermal diffusivity, $D = k/C$, of a material which dictates the transient response to a thermal input and thus critical for thermal management of high-power microelectronic devices.

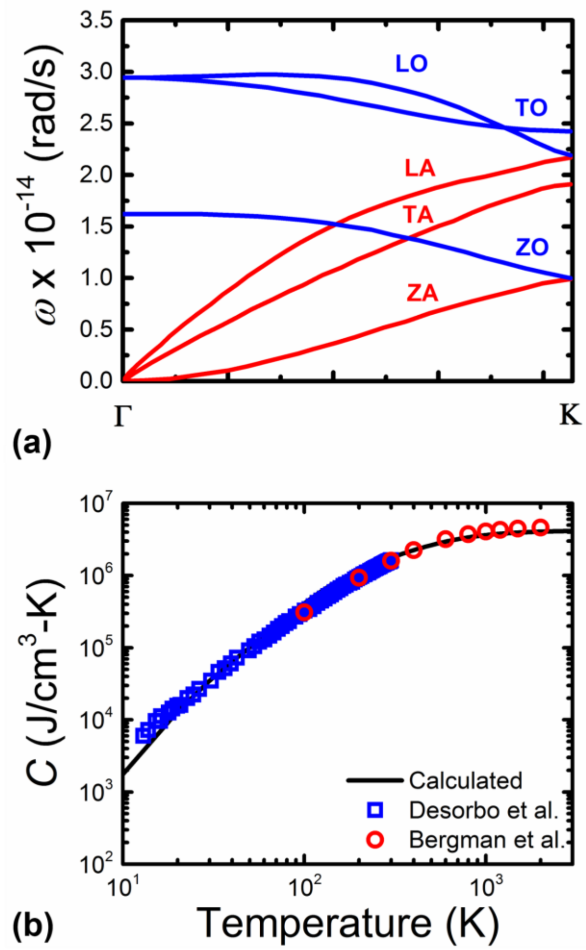

Figure 2-2 (a) Graphite phonon dispersion from literature along the high symmetry Γ→K direction of the FBZ [197]. (b) The phonon dispersion was used to calculate the heat capacity for graphite and shows good comparison with published values from Desorbo et al. [199] and Bergman et al. [185]

2.2 Oxidation Limited Metal-Graphene Interfaces

Heat removal in short channel graphene devices may be limited by metal-graphene (M-G) interfaces [200, 201] causing localized heating which can have a detrimental effect on performance and reliability of these devices. The M-G interaction is a mixture of covalent, ionic, and van der Waals interactions [202]. Metals have been categorized into two groups, weak adsorption (physisorption) and strong adsorption (chemisorption) [203-

205], based on their interfacial interaction strength with graphene. Interfaces between graphene and metals such as Ni, Co, Cr, Pd, and Ti result in chemisorption, which perturbs the electronic band structure of graphene due to hybridization of graphene π-bands with metal d-bands. These are favored over metals such as Cu, Al, Ag, Ir, Au, and Pt which result in physisorption. At physisorbed interfaces, the graphene electronic band structure is preserved; however, significant charge transfer may occur from metal to graphene, or vice versa, depending on the differences in work function causing a shift in graphene Fermi level and the formation of an interface dipole layer.

This difference is illustrated graphically in Figure 2-3 where Khomyakov et al. [204] used plane averaged electron density to visualize the electron redistribution around the interface. In Figure 2-3(a), the density of electrons on either side of the interface is high for physisorbed M-G interface such as Au but quite low at interface (i.e., dipole formation). However, Figure 2-3(b) shows that for chemisorbed Ni-G interface the electron density at the interface is high. Also, the charge per carbon atom was greater compared to physisorbed Au, and the graphene metal separation difference was lower. The graphene becomes n-type (Cu, Al, Ag, Ni, Co, Pd, Ti) or p-type (Au, Pt) doped depending on the selection of metal contacts and can be used to create p-n junctions [206, 207]. However, the thermal transport at the M-G interface has been attributed to phonons [208-210]. The M-G interaction has also been shown to affect the phonon dispersion of graphene [211-215], with more pronounced changes for chemisorbed interfaces (Ni, Ti) compared to physisorbed (Au, Cu, Pt).

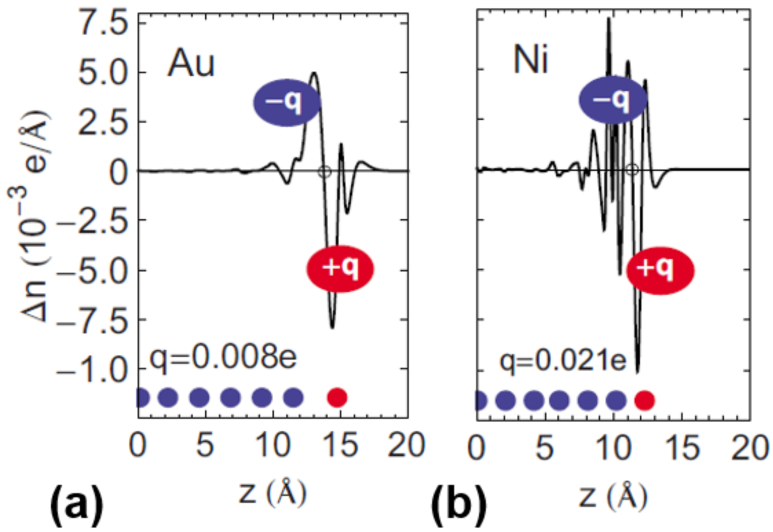

Figure 2-3 (a) Plane averaged electron density show formation of dipole characteristic of physisorbed Au-G interface. (b) At chemisorbed Ni-G interface, the distribution of electrons is significantly different, and the charge per carbon atom is higher and the separation distance smaller. Adapted from [204]. Copyright 2009 American Physical Society.

Previous studies have shown that metal-graphene-metal (M-G-M) sandwiched structure may enhance the M-G interface interaction. Gong et al. [216] varied the top and bottom metals in an effort to improve the interface interaction between graphene and physisorbed metals. The result was increased binding energy at Cu-, Ag-, Ir-, Au-, and Pt-G interfaces, which was attributed to different interface dipoles being formed at the top and bottom M-G interfaces. Franklin et al. [217], using 25 nm Pd-5 nm Ti as the bottom metal and 30 nm Au-30 nm Pd-0.5 nm Ti as the top metal, showed a 40% reduction in electrical contact resistance (Figure 2-4). This was attributed to enhanced M-G coupling and higher graphene doping. Using density functional theory (DFT), Liang et al. [215] showed a significant change in the phonon DOSs of single-layer graphene (SLG) sandwiched between Ti layers, which was attributed to strong interactions of SLG with Ti (chemisorbed) compared to Cu and Au (physiorbed). The result was much higher TBC at

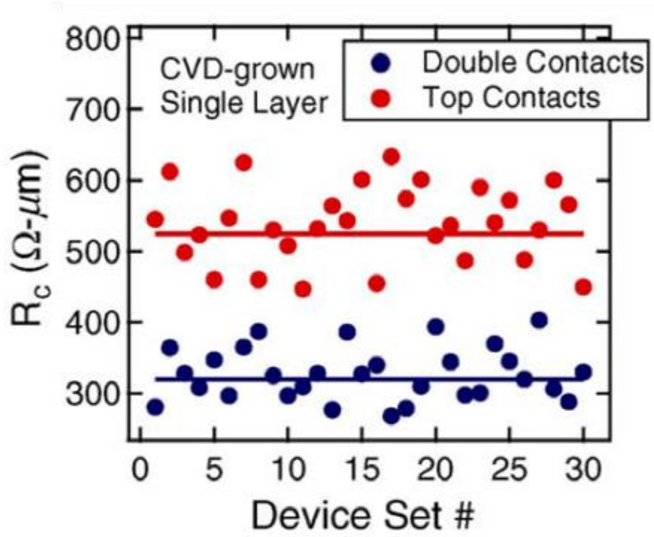

Figure 2-4 A 40% reduction in electrical resistance at metal-graphene-metal (i.e., double contacts) was observed compared to metal-graphene (i.e., top contacts) [217]. Copyright 2011 IEEE.

Ti-SLG-Ti interface compared to Au-SLG-Au and Cu-SLG-Cu interfaces calculated using DFT along with the atomistic Green's function (AGF) method. Mao et al. [218] also showed increased TBC at chemisorbed Ni-SLG interface compared to physisorbed Au- and Cu-SLG using first-principles calculations.

Time-domain thermoreflectance (TDTR) has been used previously to measure TBC at M-HOPG [219, 220], M-G-SiO_2 [208, 221-225], and M-G-M interfaces [209, 210, 226, 227]. Schmidt et al. [219] reported the TBC at Ti-HOPG interface to be three to four times higher than Au-HOPG interface and two to three times higher than Al-HOPG interface, indicating that chemisorbed interfaces can have much higher TBC. The inclusion of a 5 nm Ti adhesion increased TBC at Al-HOPG interface to values comparable to Ti-HOPG interface. Gengler et al. [220] measured TBC at several M-HOPG interfaces and found TBC increased with metal Debye temperature up to ~400 K and remained constant at ~60 MW/m^2-K above 400 K. The M-HOPG studies are insufficient to completely explain the M-G interaction since HOPG is essentially successive graphene layers bonded by van der

Waals forces, while isolated graphene must be supported by materials (e.g., SiO_2, metals) with very different vibrational properties, interface structure, and chemical interaction (if any).

Koh et al. [208] reported the TBC at Au-G-SiO_2 (2 nm Ti adhesion layer) interface to be 20-30 MW/m^2-K at RT for 1-10 graphene layers. In the same study, TBC was found to depend weakly on temperature above 100 K suggesting the dominant heat carriers across this interface were acoustic phonons. Hopkins et al. [221] chemically functionalized graphene with oxygen using O_2 plasma in an Al-G-SiO_2 structure [6], and TBC was increased from 30 to 40 MW/m^2-K at RT demonstrating that interfacial bonding plays important role in heat transport across this interface [228]. Foley et al. [223] and Walton et al. [224] also studied the effects of plasma-functionalization of graphene. Foley et al. [223] also observed no enhancement in TBC or electrical contact conductance at Au-G-SiO_2 interface with and without a Ti adhesion layer. The authors attributed this to the limited surface reactivity of the graphene surface, however, this effect was not investigated for additional metals such as Ni or even Cr.

Yang et al. [222] used frequency-domain thermoreflectance (FDTR) to create micron-scale maps of TBC as well as in-plane thermal conductance, which was used to determine thermal conductivity of graphene, encased between Ti and SiO_2. The TBC was reported to 20-25 MW/m^2-K at RT for one to seven graphene layers, similar to values at Au-G-SiO_2 interface. The effect of oxidation on transport properties at Ti-G interface has been reported recently by Freedy et al. [225], who showed TBC decreased with increasing oxide composition in a 5 nm Ti film on SiO_2 by varying Ti deposition rate. A similar result was observed at other metal-nonmetal interfaces [229]. Jiang et al. [226] combined X-ray photoelectron spectroscopy (XPS) and TDTR and observed enhanced TBC across Al-G-Cu, Cu-G-Cu, and Pt-G-Cu interfaces through controlled oxidation of graphene (Figure 2-5(a)). Huang et al. [209] showed that improving conformity of graphene to underlying metal increased TBC across Al-G-Cu interface by 35% despite oxidation of underlying Cu layer (Figure 2-5(b)). The contribution of electrons across M-G-M interfaces has been the subject of recent literature. Zhang et al. [227] reported an electronic contribution while the temperature-dependence of TBC reported by Huang et al. [210] for Pd-G-Pd seemed to confirm no electronic contribution. Despite numerous studies, the TBC at suspected physisorbed and chemisorbed M-G interfaces has never been directly compared.

2.3 Hexagonal Boron Nitride-Graphene Heterostructures

To date, the most popular approach to creating 2D material heterostructures has been mechanical stacking of exfoliated or chemical vapor deposition (CVD) grown layers

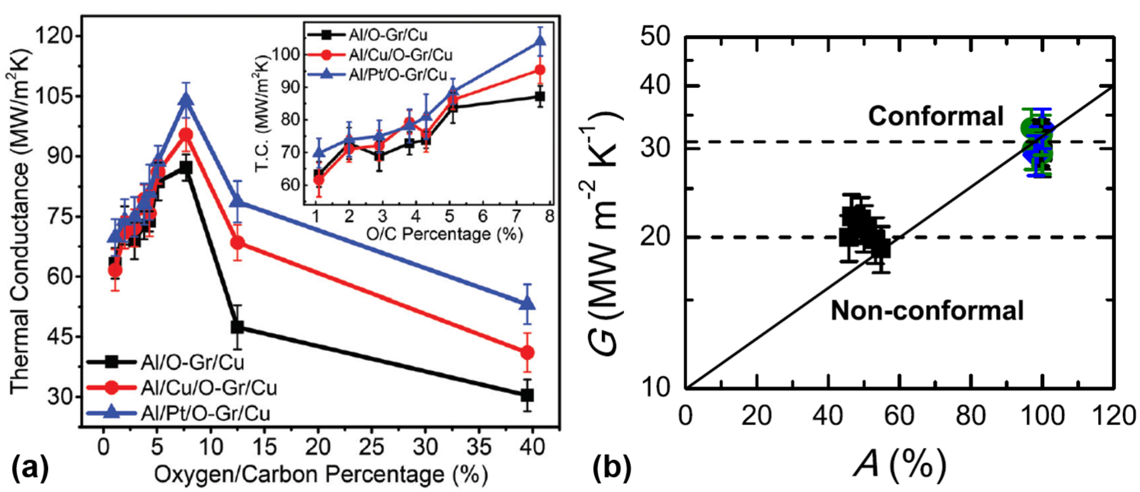

Figure 2-5 (a) Graphene surface oxidation enhanced TBC from 38 – 55% at various metal-graphene interfaces but decreased as oxygen/carbon atom percentage rose above ~7.7% [226]. Copyright 2016 Royal Society of Chemistry. (b) Improved surface conformity of graphene following anneal at 300 °C, led to a 35% increase in metal-graphene TBC [209]. Copyright 2016 Elsevier Ltd.

[45-48, 50-54, 57]; however, direct, sequential CVD growth [230-233] or epitaxial growth on exfoliated 2D layers [234-236] are also possible. Regardless of preparation method, different stacking arrangements in graphene-h-BN vertical heterostructures are possible resulting in different electronic and phononic properties [69, 237-241]. As stated earlier, heat dissipation from atomically-thin 2D layers is limited by interfacial transport [171], also making them an ideal material system for the study of interfacial thermal transport. Nevertheless, thermal transport across the interfaces in van der Waals heterostructures is not completely understood but is required to keep the device temperature below threshold and enable energy efficient operation. Also, interface quality can vary from sample to sample and across samples based on preparation method making it difficult to obtain an intrinsic measurement. Ultimately, proper control and characterization of the thermal interfaces in layered heterostructures is crucial for practical device applications.

The TBC at graphene-h-BN interfaces have been reported recently [241-246]. Using first principles AGF simulations, Mao et al. [242] reported a RT TBC of 187 MW/m^2-K for a multilayer graphene-multilayer h-BN structure. Zhang et al. [244] estimated the TBC at graphene nanoribbon-h-BN bilayer structure to be 5 MW/m^2-K at RT using classical molecular dynamics (MD) simulations. Yan et al. [241] used first principles simulations to study the effect of stacking arrangement on TBC for monolayer graphene sandwiched between layers of h-BN. The RT TBC values reported in this study ranged from 30-50 MW/m^2-K. The first experimental measurement was performed by Chen et al. [243] using Raman spectroscopy. The reported value of 7.4 MW/m^2-K was less than most theoretical results, which the authors attributed to trapped impurities resulting from the transfer process. Liu et al. [245] measured TBC at graphene-h-BN interface to be 52.2

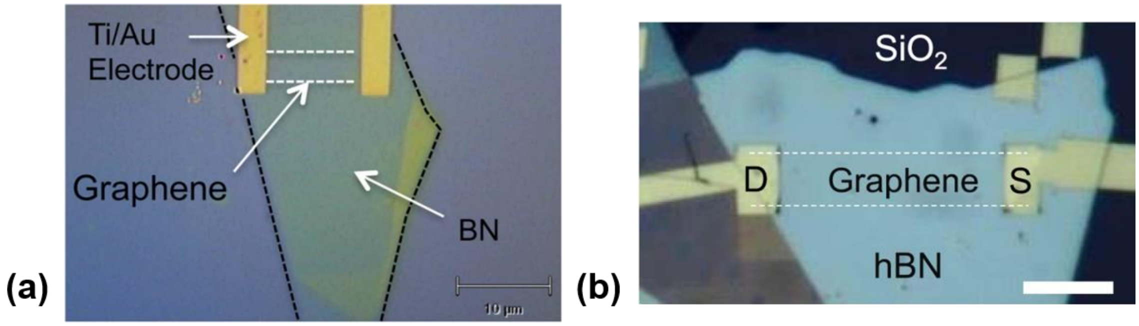

Figure 2-6 The Raman spectroscopy technique used to measure the TBC at graphene-h-BN interfaces requires a patterning step to form electrical leads for Joule heating of graphene layer. The above optical images of samples tested in studies by (a) Chen et al. [243] and (b) Kim et al. [246] with metal electrodes. The variation of TBC for independently measured samples with identical technique demonstrates the necessity for additional investigations of the graphene-h-BN interface. (a) Copyright 2014 AIP Publishing LLC. (b) 2018 IOP Publishing Ltd.

MW/m^2-K using the same Raman technique, while Kim et al. [246] predicted TBC of 5-10 MW/m^2-K in electrically biased graphene FET on h-BN substrate. Recently, Choi et al. [247] observed a two-fold reduction in hotspot temperature in graphene devices on h-BN compared to SiO_2 highlighting the potential impact of the graphene-h-BN interface. Variation in TBC values calculated using different atomistic simulation techniques such as AGF and MD may be expected due to different assumptions and limitations. However, there is discrepancy in results even when an identical measurement technique, Raman spectroscopy, is used. Also, the Raman technique requires a patterning step to form leads (Figure 2-6) for electrically heating the graphene to create a temperature difference.

2.4 Spatial Mapping of Metal-$MoSe_2$ Interfaces

The electrical properties of metal-TMD interfaces have been studied extensively [82, 248-251], but much less attention has been given to the thermal properties until recently. The metal contacts can be an important heat transfer pathway for flexible devices on polymer substrates [252]. In addition, operating temperature may affect the semiconducting properties of TMDs [88, 253] making proper thermal management critical to design and performance of TMD devices. Previous studies have looked at the effect of different work function metal contacts on electrical properties of the metal-$MoSe_2$ interface [254, 255]. The choice of metal contact can affect binding energy, charge redistribution, and doping resulting in varying Schottky barrier heights for carrier injection from metal to $MoSe_2$. In addition, the interfacial properties may change for face- and edge-contacted devices similar to graphene [256].

Theoretical and experimental studies have reported TBC at metal-MoS_2 [257-259] or substrate-MoS_2 interface [260-263]. Mao et al. [257] and Yan et al. [259] even reported enhanced TBC for chemisorbed (i.e., strongly adsorbed) metal-MoS_2 interfaces caused by orbital hybridization and electronic charge redistribution enhancing the phonon transmission at metal-MoS_2 interface. However, much less work has been reported on $MoSe_2$ despite its technological importance with an emphasis on the thermal conductivity [264-266]. Zhang et al. [267] used Raman spectroscopy to measure the TBC across $MoSe_2$-metal-SiO_2 interface and reported an extremely low value of 0.1 MW/m^2-K. The thermal properties of the metal-$MoSe_2$ interface have yet to be studied extensively beyond this study. The metal-$MoSe_2$-SiO_2 interface represents the electrical contact geometry in a typical TMD based device which is an important heat transfer pathway in short channel devices [200], thus the interface must be engineered to maximize heat removal.

2.5 Thermal Conductivity and Heat Capacity of Thin Film Hafnia

Amorphous HfO_2 films become partially crystalline as thickness of deposition increases which can affect surface morphology [268, 269] and electrical properties [270, 271]. While the thermal properties of polycrystalline and amorphous HfO_2 films have been reported [272-276], the effect of crystallization is not completely understood. Thermal property measurement of thin film samples can become relatively complex compared to measuring properties of bulk samples as contact resistances become comparable with the resistance of thin films. Thermal conductivity of thin film HfO_2 were reported by several studies. Lee and Cahill [272] measured the thermal conductivity of >500 nm polycrystalline HfO_2 using the 3ω method to be ~1.2 W/m-K at RT. Hinz et al. [273] used scanning thermal microscopy to estimate the thermal conductivity of a 3 nm a-HfO_2 layer to be 0.27 W/m-K.

Few measurements of RT heat capacity of thin film of HfO_2 can be found in literature. A very early study of bulk monoclinic HfO_2 (with 1.66% ZrO2 impurity) reported molar heat capacity of 60.25 J/mol-K [277], while a more recent study determined the molar heat capacity of monoclinic HfO_2 powder to be 58.63 J/mol-K [278]. These values correspond to volumetric heat capacity of 2.69 – 2.77 J/cm^3-K. The electronic application of HfO_2 typically uses amorphous phases, the properties of which may be affected by impurities, nanocrystalline structure, etc. The existence of nanocrystalline structure inside sample might lead to differences in heat capacity compared to bulk due to the modification in interatomic coupling as a consequence of variation in atomic structure [279] and excess volume due to grain boundaries [280]. Wang et al. [281] observed heat capacity enhancement for Al_2O_3. Microcalorimeters have been used to study heat capacity of thin films [282, 283] with few examples of heat capacity enhancement [284-286]. Accurate estimation of thermal properties is important to better understand and analyze HfO_2 based electronic devices.

TDTR and its counterpart FDTR have been used previously to determine the thermal conductivity and heat capacity of thin films and substrates [276, 287-290]. Schmidt et al. [287] used FDTR to simultaneously measure metal-substrate TBC, substrate thermal conductivity, and heat capacity in Si and sapphire samples. Liu et al. [288] used frequency-dependent TDTR to determine the thermal conductivity and heat capacity of Si and thin film SiO_2. The method was then extended to hybrid organic-inorganic multilayer thin films. Wei et al. [289] determined the thermal conductivity and heat capacity of several known materials by performing TDTR measurements at low (100 kHz) and high (10 MHz) frequencies and, also, as a function of delay time to isolate the different parameters of interest. Olson et al. [290] recently used TDTR to measure the thermal conductivity and heat capacity of thin fluorine tin oxide films.

Panzer et al. [274] used TDTR to estimate thermal conductivity of 5.6 to 20 nm HfO_2 films and values varied from 0.49 to 0.95 W/m-K at RT. The thickness dependency of conductivity was not yet clear. Scott et al. [275] measured thermal conductivity of thin (1 – 10 nm) HfO_2 films close to bulk value [183]. More recently, the effective thermal conductivity of 20 nm thick $Hf_{1-x}Zr_xO_2$ ($0\leq x\leq1$) and heat capacity for films with x=0.5 and x=0.7 were reported [276]. The thin nature of the films makes intrinsic thermal conductivity difficult to measure directly, thus effective thermal conductivity was determined which includes the contribution of the interfaces on both sides of the thin film. The heat capacity for x=0.5 was below the bulk value which was attributed to the presence of tetragonal and orthorhombic crystalline phases. Atomic layer deposition (ALD) was employed in the preceding studies using TDTR, but results for HfO_2 films of intermediate thickness (e.g., 100 – 200 nm) have not been reported.

2.6 Contributions

The major contributions and important findings of the current work are listed below.

In the study of thermal transport at metal-graphene interfaces:

(1) TDTR is used to investigate the effect of physisorption versus chemisorption on the TBC at M-G-M interfaces. No enhancement of TBC was observed, which was attributed to the presence of native oxide of several nm in the bottom layer of the M-G-M interface employing transition metals Ti and Ni. The TBC at the Ti-Ti and Ni-Ni interfaces was also reduced significantly compared to the Au-Au interface in this study confirming the effect of oxidation on the TBC. Also, the insertion of single-layer graphene into the Au-Au interface substantially reduced the electronic contribution to TBC which are the primary thermal carriers at M-M interfaces. These findings highlight a critical design consideration for the M-G-M interfaces in future device applications.

In the study of thermal transport in h-BN-graphene heterostructures:

(2) The TBC at the interface of h-BN and graphene is measured at RT using TDTR for the first time. At the time this thesis is being written, a Raman spectroscopy technique requiring lithographically patterned metal lines to electrically heat the graphene layer has been the lone method of interrogation. TDTR requires no special sample preparation only the deposition of thin metal film. The phonon transmission and TBC at h-BN-graphene interface is predicted using two forms of the diffuse mismatch model for anisotropic materials, which at the time of writing, has not been reported in literature. The results of this study have implications for heterostructures composed of 2D materials.

In the study on spatial mapping of TBC at metal-$MoSe_2$ interfaces:

(3) A direct-write photolithography technique is used to isolate $MoSe_2$ islands grown by CVD. A modified TDTR technique, requiring much less time than traditional TDTR scans, is used to create 2D maps showing the spatial variation of TBC across M-$MoSe_2$-SiO_2 interfaces. Analysis of images reveals higher TBC in single-layer regions compared to bilayer. Traditional TDTR scans show increased TBC at Ti-$MoSe_2$-SiO_2 interface compared to Al-$MoSe_2$-SiO_2, consistent with the 2D maps of TBC. The results emphasize the impact selection of metal contacts have on the thermal dissipation from electrical contacts in future $MoSe_2$ devices.

In the study of thermal conductivity and heat capacity of thin film hafnia (HfO_2),

(4) TDTR is used to measure the thermal conductivity and heat capacity of HfO_2 thin films of varying thickness. The thermal conductivity of 53, 106, and 215 nm films were near the bulk value; however, a 20% reduction in bulk heat capacity was observed for the 215 nm film compared to thinner films. Transmission electron microscopy revealed a combination of crystalline and amorphous regions in the thicker HfO_2 films. Decreased film density is expected to be the origin of the reduction of heat capacity for the 215 nm HfO_2 layer. The effective thermal conductivity, which includes the contribution of the interfaces on the top and bottom of the thin films, was used to determine the thickness-independent thermal conductivity of HfO_2 films from 12 to 215 nm.

CHAPTER 3. METHODOLOGY

In recent years, the research community has witnessed advances in the understanding of nanoscale heat transfer phenomena combined with development of experimental techniques to probe this regime. As a result, thermal metrology has become a critical area of research with emphasis on characterization of new materials and nanostructures. The following chapter presents the experimental setup and associated modeling for time-domain thermoreflectance (TDTR) method which is utilized to execute the studies in this dissertation. This is preceded by a brief discussion of some alternative experimental techniques. Lastly, the diffuse mismatch model (DMM) implemented in Chapter 5 is also presented.

3.1 Experimental Methodology

3.1.1 Overview

Scanning thermal microscopy (SThM) [291, 292] is a contact technique employing a sharp, temperature sensitive tip to scan the surface of a sample providing spatial temperature distribution, thermal property measurement, or thermomechanical strains [293-295]. Noncontact methods also exist which take advantage of near-field effects and conduction through air [296-298]. Atomic force microscopes (AFM) have become a popular platform for SThM driven mainly by advances in nanofabrication of cantilever-based probes [299-301] with small tip radius and understanding of nanoscale heat transfer phenomena [302, 303] (i.e., tip-sample interaction), which are the primary factors determining spatial resolution (~10 nm [304]) and confidence in results. Like AFM, SThM is a comparatively slow, low-throughput technique despite good spatial resolution. Resistive heating techniques take advantage of the temperature-dependent resistance of microfabricated metal heaters. Techniques such as the steady-state thermal bridge [176, 265, 305-309] or the frequency-domain 3ω technique [175, 310-312] provide direct measurements of the cross-plane and/or in-plane thermal conductivity of thin films and substrates following a straightforward calibration step. Techniques based on resistive thermometry measure total thermal resistance of a sample, and the properties are determined through precise knowledge of the sample geometry. As a result, the interfaces are not easily resolved without the use of multiple samples.

The use of non-invasive, optical techniques has grown tremendously in recent years. For example, Raman spectroscopy has become a popular thermal thermometry and metrology tool [8, 10, 74, 261, 267, 313]. The in-plane thermal properties of thin films and 2D materials can be determined by utilizing the Raman shift as a temperature-probe. Although the Raman laser interacts with optical phonons, which do not contribute much to heat transfer [178-180], they are very much affected by the local equilibrium temperature in a sample. However, there is a large uncertainty associated with stress-related peak shift and assumptions in the thermal model which can affect the resulting thermal properties [314]. While Raman is not altogether a time domain technique, temporal evolution of temperature can be acquired with the correct instrumentation. Time domain techniques, such as laser flash diffusivity [315], transient electrothermal [316], and thermoreflectance techniques (discussed in the next section), have the ability to resolve the bulk/thin film properties from interfaces because the thermal response is different for each component in a sample [317, 318].

3.1.2 Time-Domain Thermoreflectance

Among the time domain techniques, TDTR has become one of the most widely used to measure the thermal conductivity of thin films and substrates as well as TBC at interfaces. The nomenclature TDTR refers to the experiments performed at picosecond time-scales with modulated heating lasers, while alternative implementations employing nanosecond lasers are termed transient thermoreflectance [319]. FDTR differs from TDTR in that the experimental signal is recorded for various modulation frequencies rather than with delay time of the probe beam [287, 320-322]. Also, FDTR typically implements continuous-wave lasers as opposed to ultrafast pulsed lasers used in TDTR which generally have lower cost. Paddock and Eesley [323, 324] introduced TDTR for thermal diffusivity measurements in thin metal films. Capinski and Maris [325] described a method to improve the accuracy of measurements, while the current TDTR methodology was made popular by Cahill [326]. Combined with advances in ultrafast lasers, TDTR has since been widely implemented to study the thermal properties of thin films [193, 288, 327, 328], bulk substrates [329-331], and superlattices [332-335].

TDTR is a pump-probe optical technique which uses a modulated laser beam (pump) to heat the surface of a sample while the change in the reflectivity of the surface is monitored using an unmodulated beam (probe). A thin metal film (~100 nm) deposited on the sample converts the incoming photons to thermal energy over small distances (~10 nm) and, because of the temperature influence on its reflectivity, it also serves as a transducer to measure the temperature rise at the surface [317, 336]. Figure 3-1(a) shows an illustration of the pump and probe beam impinging on the sample surface at normal incidence, the most common setup for most TDTR experiments. Offset pump and probe

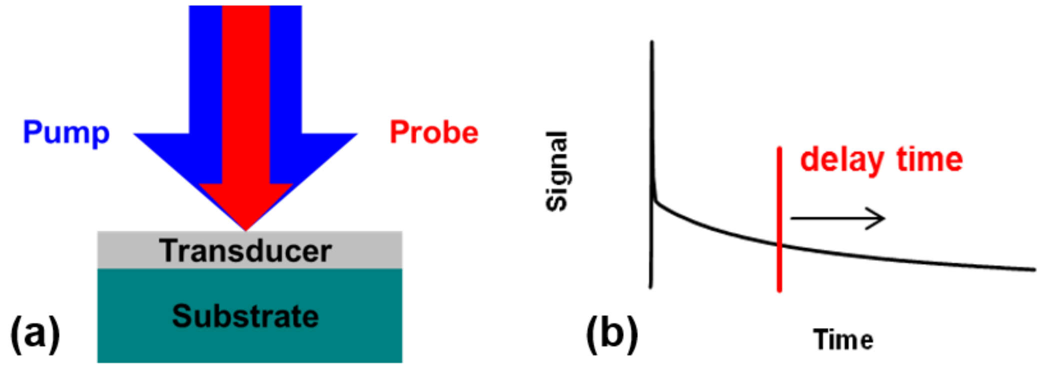

Figure 3-1 (a) Visual representation of pump and probe beams impinging on the sample surface in a typical TDTR experiment. Prior to a measurement, the sample of interest (e.g., thin film or substrate) is coated with a thin metal film which serves as a temperature transducer. (b) The probe beam measures the change in thermoreflectance of metal film. The probe is delayed relative to the pump beam, and the decay of the thermoreflectance signal is mapped as function of this delay time.

beams have been used previously to measure in-plane properties [337, 338]; however, modeling the thermal response is computationally expensive. Variable beam sizes and shapes have been used to measure in-plane thermal conductivity of highly-anisotropic materials more recently [339, 340]. Modulation of the pump beam allows the signal to be measured using a lock-in amplifier. The arrival of the probe beam is delayed relative to the pump to map the decay of the thermoreflectance signal, as shown in Figure 3-1(b), and the experimental data is fit to a thermal model [326, 329] to extract the thermal properties of interest (e.g., TBC). The known properties of the sample are used as inputs to the thermal model and unknown properties of interest are used as fitting variables.

TDTR samples are generally bilayer (metal-substrate) or trilayer (metal-thin film-substrate). The unknown properties typically include the substrate or thin film thermal conductivity and metal transducer-substrate or metal transducer-thin film and thin film-substrate TBC. Known properties of the sample are measured beforehand (e.g., metal transducer and thin film thickness) or bulk values are assumed (e.g., metal transducer, thin film, and/or substrate volumetric heat capacity). Modulation of the pump beam in TDTR measurements creates a thermal wave which heats the sample at the frequency of the modulated beam, and the amplitude and phase of this signal is measured using a lock-in amplifier [329]. The thermal penetration depth, l, is a function of this modulation frequency as well as the thermal diffusivity, D, of the sample, and is given by $l = \sqrt{D/\pi f}$, where f is the modulation frequency of the pump beam [328]. For a given sample higher modulation frequency results in lower penetration depth. In general, the cross-plane and in-plane directions can be considered for TDTR experiments on thin film samples.

An auxiliary use of TDTR systems is thin film measurement using picosecond acoustics [341, 342]. Thermal expansion near the surface of a layered sample (e.g., the metal transducer in TDTR measurements) following heating by the pump beam generates a strain wave which propagates through the film at the speed of sound in the material. The strain wave is partially reflected from an interface in the sample and creates a change in the reflectance upon returning to the surface. The result is an acoustic echo in the probe signal, the shape and intensity of which are dependent on the relative acoustic impedances of the two materials at the interface. It is commonly used as an accurate measure of transducer thickness in TDTR measurements but contains information about the interface quality as well [343]. Film thickness is determined through the relationship, $d = v_{\mathrm{s}} t_{\mathrm{echo}}/2$, where v_{s} is the longitudinal speed of sound in a material and t_{echo} is the time between the initial heating event and the first acoustic echo (or the time between successive echoes). The factor of two in the denominator accounts for the wave's propagation through the thickness of the film and return to the surface.

The two-color TDTR [344] system used in this study, pictured in Figure 3-2, utilizes a Spectra Physics Mai-Tai HP Ti:Sapphire (λ=800 nm, 40 nJ/pulse) laser with 3W average power output, ~150 fs pulse width, and repetition rate of ~80 MHz. The laser is split into two paths (pump and probe) where the pump beam is modulated with an electro-optic modulator (ConOptics Model 160) at a preselected frequency (typically 1 – 10 MHz) then frequency doubled using a BiBO crystal. Frequency doubling allows the pump beam to be spectrally filtered isolating the probe signal at the photodetector. This is necessary since the pump and probe strike the surface concentrically at a normal angle of incidence. Additionally, the probe signal can be isolated by modulating the reflected probe beam in the audio frequency regime (~200 Hz) [345] creating an additional frequency component to "lock-in" on which is not present in the pump beam. The arrival time of the probe is delayed up to 7 ns relative to the pump by adjusting its optical length using a double-pass mechanical delay stage in order to map the decay of the thermoreflectance signal. A resonant RLC circuit composed of Si PIN diode (Thorlabs DET10A) and inductor amplifies the signal and filters higher harmonics in reflected probe signal (discussed in the next section). The signal is again amplified (5x or 25x) with a Stanford Research Systems SR445a low-noise amplifier before reaching the lock-in (Stanford Research Systems SR844). Data fitting is performed using a Levenberg-Marquardt non-linear least squares regression [346].

In TDTR measurements, the error from the experimental factors is relatively small compared to the propagation of error from input parameters in the thermal model. This uncertainty is dependent upon the ratio of sensitivity of known and unknown parameters.

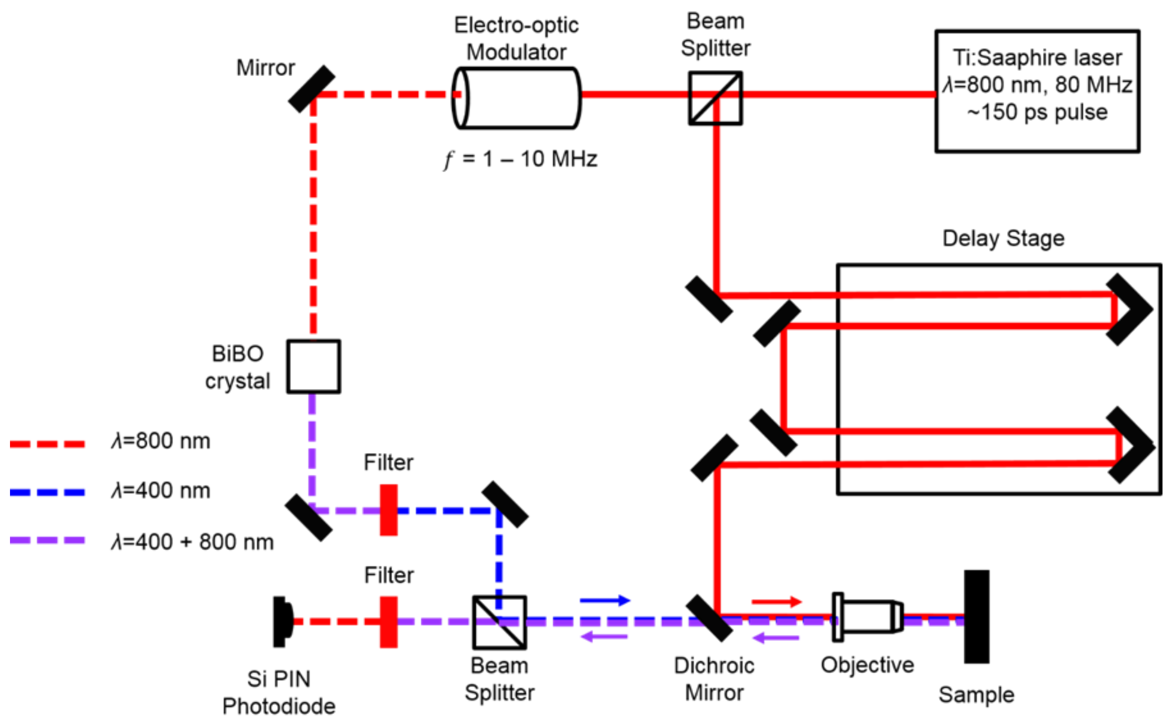

Figure 3-2 A schematic of the two-color TDTR setup used in our lab. The output of a femtosecond pulsed laser is split into two beam paths (pump and probe). The pump beam is modulated at preselected frequency (1 – 10 MHz) then frequency doubled before optically heating the sample. The frequency component of probe beam intensity is used to probe the temperature change of the sample which is then used to extract the thermal properties of interest.

Equation 1 below gives the sensitivity, S_p, to a parameter, p, in a TDTR measurement [193],

$$S_p = \frac{\partial \ln(-V_{\text{in}}/V_{\text{out}})}{\partial \ln p}, \tag{1}$$

where $-V_{\text{in}}/V_{\text{out}}$ is the ratio of in-phase and out-of-phase signals of the lock-in amplifier (discussed in more detail in the next section). A higher absolute value of sensitivity is desired for accurate data fitting, and we adjust the modulation frequency to achieve the highest sensitivity to the parameters of interest. The measurements in this study were performed at high modulation frequency to provide improved sensitivity to TBC compared to the lower frequencies.

Monte Carlo (MC) simulations [339, 347-349] to estimate the uncertainty of our measurements; these have been shown to be more accurate for low sensitivity parameters, as is the case for interfaces on SiO_2 and Ti samples in this work. The MC simulations include uncertainties due to background noise, error in setting the phase shift of the lock-in amplifier, noise in the measurement signal, and uncertainty in the fixed parameters in the model. The process is described briefly next, and a graphical representation is shown in Figure 3-3. Values for each parameter in the model are randomly sampled from a normal distribution based on their uncertainty to create a set of N initial guess values, while a series of N experimental data sets are created within the experimental uncertainty of the TDTR measurements. The value for N is generally 500-1000. Data fitting is performed for each of the N randomly generated experimental data sets using a single set of the N initial guess values to create a distribution of probable values for the parameter of interest (e.g., TBC). A 90% confidence interval is created by taking the 5th and 95th percentiles as lower and upper bounds, respectively.

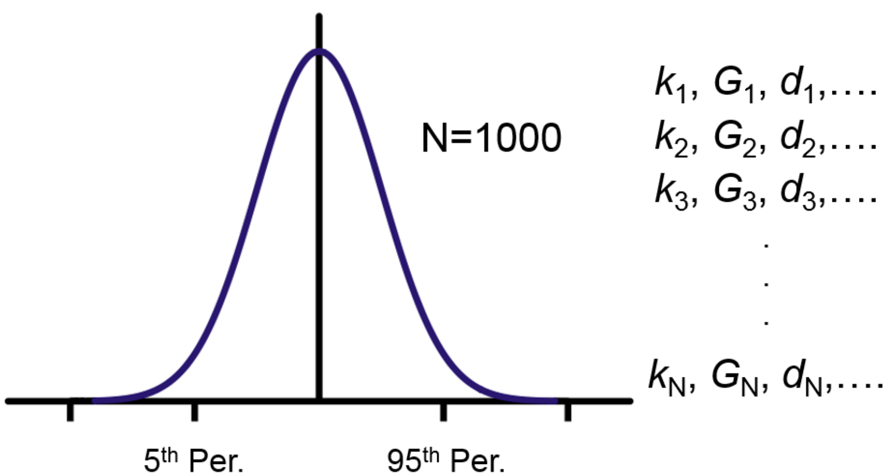

Figure 3-3 Schematic illustration of Monte Carlo method used for uncertainty estimation in TDTR experiments.

3.1.3 *Frequency-Domain Thermal Response*

The implementation of the frequency-domain thermal response to model the thermoreflectance signal made by Cahill [326] was a critical update to TDTR experiments. Beginning with the frequency-domain solution for a semi-infinite solid heated at the surface by a periodic point source [350] given by Equation 2,

$$g(r) = \frac{\exp(-qr)}{2\pi kr}, \tag{2}$$

where $q^2 = (i\omega/D)$, ω is the angular frequency, D is the thermal diffusivity, k is the thermal conductivity, r is the radial coordinate. Hankel transforms are used to simplify the convolutions in the analysis (discussed later) because of the cylindrical symmetry of the TDTR experiments. The Hankel transform of $g(r)$ is defined

$$G(s) = 2\pi \int_0^\infty g(r) J_0(2\pi sr) r dr \tag{3}$$

From a table of Hankel transforms [326], for a function $f(r) = \frac{\exp(-ar)}{r}$, the transform is given by the relationship in Equation 4,

$$F(s) = 2\pi \int_0^\infty f(r) J_0(2\pi sr) r dr = \frac{2\pi}{(4\pi^2 s^2 + a^2)^{\frac{1}{2}}} \tag{4}$$

For $g(r)$, $a = q$, and the Hankel transform can be found easily as,

$$G(s) = 2\pi \int_0^\infty \frac{\exp(-qr)}{2\pi kr} J_0(2\pi sr) r dr = \frac{1}{k(4\pi^2 s^2 + q^2)^{\frac{1}{2}}} \tag{5}$$

Schmidt et al. [329] showed the analysis is identical for anisotropic materials, however $q^2 = \left(k_r s^2 + \rho c_p i\omega\right)/k_z$ following the Hankel transform of the heat diffusion equation in cylindrical coordinates. k_r and k_z are the in-plane and cross-plane thermal conductivity, respectively, ρ is mass density, and c_p is specific heat.

In TDTR, the modulated pump laser beam heating the surface of a sample, has a Gaussian distribution of intensity [326] which is given by

$$p(r) = \frac{2A}{\pi w_0^2} \exp(-2r^2/w_0^2), \tag{6}$$

where A is the laser power, w_0 is the $1/e^2$ radius of the pump beam. The Hankel transform of $p(r)$ is defined as

$$P(s) = 2\pi \int_0^\infty p(r) J_0(2\pi sr) r dr \tag{7}$$

Again, from a table of Hankel transforms [351] one can find that in general for a function $f(r) = \exp(-a^2r^2)$, the Hankel transform is

$$F(s) = 2\pi \int_0^\infty f(r) J_0(2\pi sr) r dr = \frac{\pi}{a^2} \exp\left[-\frac{(2\pi s)^2}{4a^2}\right] \tag{8}$$

In the expression for $p(r)$, $a^2 = \frac{2}{w_0^2}$, and the Hankel transform is thus,

$$P(s) = 2\pi \int_0^\infty \frac{2A}{\pi w_0^2} \exp\left(-\frac{2r^2}{w_0^2}\right) J_0(2\pi sr) r dr = A \exp\left(-\frac{\pi^2 s^2 w_0^2}{2}\right) \tag{9}$$

The temperature rise at the surface, $\theta(r)$, due to the pump laser is a convolution of thermal response and pump beam intensity. The analysis is simplified in the frequency domain where the solution is given by the inverse transform of the product of $G(s)$ and $P(s)$,

$$\theta(r) = 2\pi \int_0^\infty P(s) G(s) J_0(2\pi sr) s ds \tag{10}$$

The probe laser measures the surface temperature of the metal transducer which is proportional to the change in reflectivity of the sample. The lock-in amplifier records the change in reflected intensity of the probe beam. The probe also has a Gaussian distribution of intensity and the measured signal is a weighted average of the temperature distribution $\theta(r)$ given by

$$\Delta T = \frac{4}{w_1^2}\int_0^\infty \theta(r)\exp\left(-\frac{2r^2}{w_1^2}\right) r dr \tag{11}$$

Substituting the expression for $\theta(r)$, ΔT becomes

$$\Delta T = \frac{4}{w_1^2}\int_0^\infty \left[2\pi \int_0^\infty P(s)G(s)J_0(2\pi sr)sds\right]\exp\left(-\frac{2r^2}{w_1^2}\right) r dr \tag{12}$$

Moving the Bessel function inside the integral over r and rearranging gives

$$\Delta T = \frac{4}{w_1^2}\int_0^\infty P(s)G(s)sds\left[2\pi \int_0^\infty \exp\left(-\frac{2r^2}{w_1^2}\right)J_0(2\pi sr) r dr\right] \tag{13}$$

The term $\left[2\pi \int_0^\infty \exp\left(-\frac{2r^2}{w_1^2}\right)J_0(2\pi sr) r dr\right]$ is a Hankel transform for a function of the form $f(r) = \exp(-a^2r^2)$, for which the Hankel transform was given previously in Equation 8. Now $a^2 = \frac{2}{w_1^2}$, and performing a Hankel transform and inserting this result into ΔT, the expression becomes,

$$\Delta T = \frac{4}{w_1^2}\int_0^\infty P(s)G(s)sds\left[\frac{\pi w_1^2}{2}\exp\left(-\frac{\pi^2 s^2 w_1^2}{2}\right)\right] \tag{14}$$

Rearranging and cancelling out terms,

$$\Delta T = 2\pi \int_0^\infty P(s)G(s)\exp\left(-\frac{\pi^2 s^2 w_1^2}{2}\right) sds \tag{15}$$

Plugging in the expression for $P(s)$ obtained earlier gives

$$\Delta T = 2\pi A\int_0^\infty G(s)\exp\left[-\frac{\pi^2 s^2 (w_0^2+w_1^2)}{2}\right] sds, \tag{16}$$

which is a single integral over s to be evaluated numerically. The upper limit of the integral can be set to $2/\sqrt{w_0^2 + w_1^2}$ because $\exp\left[-\frac{\pi^2 s^2 (w_0^2+w_1^2)}{2}\right]$ decreases rapidly with increasing s. Schmidt et al. [329] uses an upper limit of $10/\sqrt{w_0^2 + w_1^2}$.

The algorithm described by Feldman [352] can be used to generalize the expression for surface temperature, ΔT, for layered structures. The difference is the expression used for $G(s)$ which is given by,

$$G(s) = \left(\frac{B_1^+ + B_1^-}{B_1^- + B_1^+}\right)\frac{1}{\gamma_1} \tag{17}$$

The terms B_1^+ and B_1^- correspond to thermal waves propogating in the positive and negative z directions, respectively, normal to the sample surface [353]. The solution is found iteratively starting with the layer furthest from the surface using the expression

$$\binom{B^+}{B^-}_n = \frac{1}{2\gamma_1}\begin{bmatrix}\exp(-u_n L_n) & 0 \\ 0 & \exp(u_n L_n)\end{bmatrix}\begin{pmatrix}\gamma_n - \gamma_{n+1} + \gamma_n\gamma_{n+1}/TBC_{n,n+1} \\ \gamma_n + \gamma_{n+1} + \gamma_n\gamma_{n+1}/TBC_{n,n+1}\end{pmatrix}\binom{B^+}{B^-}_{n+1}, \tag{18}$$

where $u_n = (4\pi^2 s^2 + q_n^2)^{\frac{1}{2}}$, $q_n^2 = i\omega/D_n$ [or $q_n^2 = \left(k_{r,n}s^2 + \rho_n c_{p,n} i\omega\right)/k_{z,n}$], $\gamma_n = k_n u_n$, and $TBC_{n,n+1}$ is the thermal boundary conductance between layer n and layer $n + 1$. The top layer corresponds to n = 1 and is of the layer of interest in order to find the temperature oscillation at the surface. The layer furthest from the surface is considered to semi-infinite therefore $\binom{B^+}{B^-}_n = \binom{0}{1}$.

3.1.4 Modeling Experimental Data Using the Frequency-Domain Solution

The frequency domain thermal response is used to calculate the changes in reflectivity measured during a TDTR experiment. A graphical depiction of the measurement process presented by Schmidt et al. [329] is pictured in Figure 3-4 and described here briefly. The laser output can be approximated as a series of delta functions separated by the period of the laser, τ, since the pulse duration (~150 fs) is much shorter than the measurement time scale and pulse repetition period. The frequency spectrum of the laser output is also a series of delta functions separated in frequency by the repetition rate of the laser, $1/\tau$. The pump beam passes through an electro-optic modulator, which chops the beam with a square wave modulation at a 50% duty cycle at the modulation frequency, f. The use of lower values of f increase the penetration depth of thermal waves but higher modulation frequency gives better spatial resolution [354], minimizes influences of uncertainties in beam diameter [355], and reduces the effects of radial heat flow [336].

As discussed in more detail next, the lock-in amplifier measures the fundamental harmonic component of the reflected probe beam. As a result, the heating event created by the pump can be approximated as a sine wave (Figure 3-4(a)). The high repetition rate of the laser (~80 MHz) prevents the sample from returning to ambient temperature between successive pulses, a phenomenon termed pulse accumulation [329]. Figure 3-4(b) shows the temperature decay of the sample between pulses. The arrival time of probe beam is delayed relative to the pump to map the decay of the thermoreflectance signal. The probe measures the response to the pump beam at a single delay time between each pulse. This is shown graphically in Figure 3-4(c).

Lock-in detection extracts an extremely narrow band around the reference signal and only the fundamental harmonic component of the signal at f is considered. The lock-in amplifier used in our setup (Stanford Research Systems SR844) uses a square wave mixer instead of a pure sinusoid. The signal is amplified and filtered by placing an inductor in series with the output of the Si PIN photodiode and the 50 Ω input of the lock-in

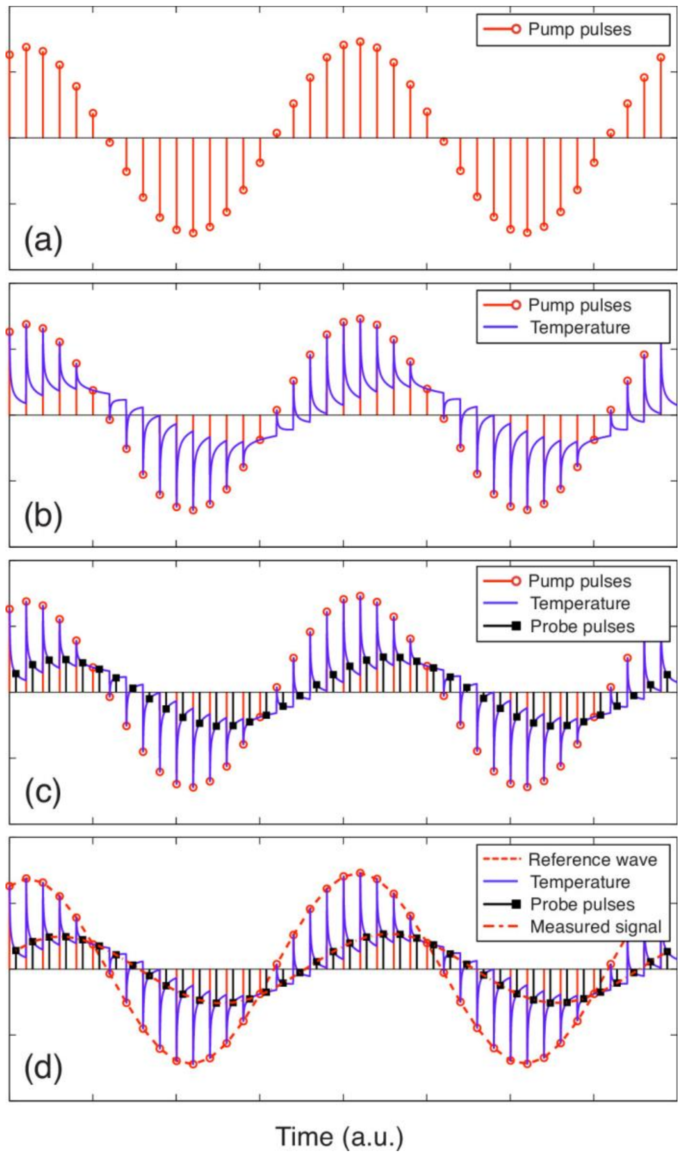

Figure 3-4 (a) The heating event can be considered a sine wave because the lock-in amplifier only measures the response to the fundamental harmonic component at the modulation frequency of the pump beam. (b) The repetition rate of the laser (~80 MHz) prevent the sample from reaching ambient temperature between successive pulse, a phenomenon called pulse accumulation. (c) The arrival time of the probe is delayed relative to the pump and measures the response to a pump pulse. (d) The TDTR signal, as measured by the lock-in amplifier, is the fundamental harmonic component of modulated heating event created by the pump. The result is, thus, a sine wave at the modulation frequency of the pump laser with different amplitude and phase. Copyright 2008 American Institute of Physics [329].

amplifier to remove the odd harmonics of the frequency f [356]. The lock-in amplifier measures the fundamental harmonic component of the probe laser at the modulation frequency of the pump laser which represents the temporal decay in thermoreflectance response of the sample. The measured signal is displayed in Figure 3-4(d). The output of the lock-in amplifier is the amplitude and phase of the probe beam in response to the thermal wave resulting from the heating event created by the pump [287]. The amplitude and phase of the signal are a function of the properties of the sample and the delay time between the pump and probe beam. The probe beam is delayed relative to the pump, and reflectivity data is taken as a function of this delay time.

As stated earlier, the change in surface temperature is proportional to the change in reflectivity measured by the probe beam. In the time domain, the signal of interest is given by the convolution of the thermal response and the probe beam intensity, but in the frequency domain this becomes multiplication. The real and imaginary parts of the change in reflectivity, $\Delta R(t)$, are given by

$$\mathrm{Re}[\Delta R(t)] = \frac{dR}{dT}\sum_{m=-\infty}^{\infty}[\Delta T(m/\tau + f) + \Delta T(m/\tau - f)]\exp(i2\pi mt/\tau), \qquad (19a)$$

$$\mathrm{Im}[\Delta R(t)] = -i\frac{dR}{dT}\sum_{m=-\infty}^{\infty}[\Delta T(m/\tau + f) - \Delta T(m/\tau - f)]\exp(i2\pi mt/\tau), \qquad (19b)$$

where $\frac{dR}{dT}$ is the thermoreflectance coefficient of the sample and t is the probe delay time. The lock-in amplifier used in our setup employs phase-sensitive detection with two square wave mixers. The reference inputs to the mixers are both at the modulation frequency f, but 90° out of phase with each other allowing both amplitude *and* phase of the thermoreflectance signal to be determined. Thus, the output of the lock-in amplifier has an in-phase and out-of-phase component [193, 326]

$$V(t) = V_{\mathrm{in}}(t) + iV_{\mathrm{out}}(t) \propto \frac{\Delta R(t)}{R}, \qquad (20)$$

where R is the reflectivity of the sample. The out-of-phase component corrects for experimental artifacts caused by error in focusing of the pump beam and pump-probe overlap [336], as well as gain of the electronics and properties of the photodetector [356]. V_{in} is essentially proportional to the surface temperature as a function of delay time, while V_{out} is proportional to the steady state temperature rise [355]. In addition, the reflectivity and thermoreflectance coefficient of the sample does not need to be measured separately if the ratio

$$-\frac{V_{\mathrm{in}}}{iV_{\mathrm{out}}} = \frac{\sum_{m=-\infty}^{\infty}[\Delta T(m/\tau+f)+\Delta T(m/\tau-f)]\exp(i2\pi mt/\tau)}{\sum_{m=-\infty}^{\infty}[\Delta T(m/\tau+f)-\Delta T(m/\tau-f)]\exp(i2\pi mt/\tau)}, \quad (21)$$

is used in data analysis.

3.2 Diffuse Mismatch Model

Increases in computational power has led inextricably to advances in simulation techniques for determining thermal properties [357]. Methodologies such as MD [358-361], lattice dynamics [362-364], and first principles simulations [214, 215, 241, 259] are continuously being implemented for calculation of thermal conductivity and TBC. However, each method contains inherent limitations and extreme care must be taken when interpreting results because of many assumptions associated with each technique. Crude models such as the acoustic mismatch model (AMM) [365-367], diffuse mismatch model (DMM) [191, 368-371], and similar variations like the maximum transmission limit (MTL) [198, 372] and radiation limit (RL) [194, 373, 374] are still popular for calculation of TBC. The main difference between these crude models is the calculation of the transmission at the interface. The concept of phonon transmission will be discussed in more detail in the next paragraph along with the DMM which is used here. The AMM assumes specular reflection at the interface which is valid only at small temperatures (T<30 K) when the long-wavelength phonons dominate heat transfer [191]. The aim of the MTL and RL are to set upper limits to the phonon transmission and, thus, the TBC. The MTL allows perfect transmission from one side of the interface [372] and is only limited by the need to satisfy the laws of thermodynamics. In a similar way, the RL assumes that phonons from one side of the interface have a transmission of 1 [373].

The original derivation of the DMM presented by Swartz and Pohl [191] assumed diffuse, elastic scattering of phonons at the interface of two materials. Phonons impinging on the interface scatter, losing all memory of their origin but maintain their frequency. Accordingly, phonons will transmit or reflect (Figure 3-5), and the probability for transmission is dependent only on the DOS of the material. A later study by Stoner and Maris [192] showed that the elastic assumption under predicts the TBC compared to experimental measurements. More recent work has taken into account phonon dispersion [368], interfacial mixing [369], surface roughness [370], and inelastic scattering [371] with varying amounts of success. Nevertheless, the DMM remains a useful tool for capturing trends in the phonon transmission across interfaces and because of its simple implementation.

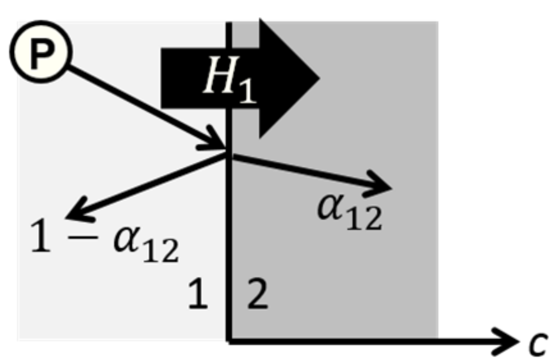

Figure 3-5 The diffuse scattering assumption means phonons lose all memory of their origin. Incident phonons transmit or reflect upon striking an interface, and the probability of transmission depends solely on the phonon DOS.

For small ΔT, the TBC approaches $TBC = \tau \frac{\partial(\alpha_{12} H_1)}{\partial T}$ where, under the diffuse assumption [191], $\alpha_{12} = H_2/(H_1 + H_2)$ is the transmission coefficient from material 1 to material 2 and the phonon irradiation (an analog to photon irradiation) [372] H_1 (W/m^2) from a 3D isotropic solid is given by the relationship,

$$H_1 = \frac{1}{4} \sum_j \int_0^{\omega_{\max,j}} \hbar\omega v_{j,1} f(\omega, T) D_1(\omega) d\omega, \tag{22}$$

where ω is angular frequency, $v_{j,1}$ is the phonon group velocity for polarization j, and $D_1(\omega)$ is the phonon DOS. The Bose-Einstein distribution is $f(\omega, T) = \frac{1}{\exp(\hbar\omega/k_B T) - 1}$, which includes reduced Planck's constant and Boltzmann constants, $\hbar$ and k_B, respectively. The summation is carried out over each phonon polarization. From the Debye assumption [375], $\omega = vk$, the DOS becomes $D_1(\omega) = \omega^2/2\pi^2 v_j^3$. Plugging both relationships into Equation 22 and following some derivation it can be shown that

$$H_1 = \frac{k_{\mathrm{B}}^4}{8\pi^2 \hbar^3} \sum_j \frac{1}{v_j^2} \int_0^{x_{\max,j}} \frac{T^4 {x_j}^3}{e^{x_j} - 1} dx_j \tag{23}$$

In Equation 23, $x = \hbar\omega/k_{\mathrm{B}} T$ and the integration limits, $x_{\max,j}$, correspond to the maximum frequency considered in each material. The prefactor $\tau = \left[1 - \frac{1}{2}(\alpha_{12} + \alpha_{21})\right]^{-1}$ is necessary when working in terms of local equivalent equilibrium temperature [376].

An isotropic Debye dispersion (i.e., $\omega = vk$) is generally assumed and may be valid for most bulk materials, but this assumption is not acceptable in the highly anisotropic, 2D graphene and h-BN. Duda et al. [377] accounted for this anisotropy by using an effective 2D Debye density of states ($D_{\mathrm{2D,eff}}(\omega) = \frac{\omega}{2\pi v^2} \frac{1}{d}$, where d is the interlayer spacing of a 2D material like graphite). More recently, Chen et al. [198] showed this 2D DMM model greatly overpredicts the TBC and presented a new DMM model using an anisotropic Debye dispersion ($\omega^2 = v_{ab}^2 k_{ab}^2 + v_c^2 k_c^2$, where $k_{ab}^2 = k_a^2 + k_b^2$) referred to here as anisotropic-DMM (A-DMM). The resulting FBZ is ellipsoidal, as opposed to spherical in the case of an isotropic dispersion (see Figure 3-6), where the major and minor axes correspond to the graphite ab- (i.e. basal) and c-axis. The authors presented a detailed derivation and analysis where the real quasi-TA and quasi-LA branches of the phonon dispersion [378] are recomposed into two ellipsoids: TL1 and TL2 branches. Along with an additional TA branch, the phonon velocities ($v_{ab,j}$ and $v_{c,j}$) for each branch can be determined from the real phonon dispersion. The resulting cross-plane (c-axis) phonon irradiation is given by [198],

$$H_{\mathrm{A-DMM}} = \frac{k_{\mathrm{B}}^4}{8\pi^2\hbar^3}\sum_j \frac{1}{v_{ab,j}^2}\left\{\int_0^{x_{\max,c,j}} \frac{T^4 {x_j}^3}{e^{x_j}-1}dx_j + \int_{x_{\max,c,j}}^{x_{\max,ab,j}}\left[\frac{\theta_{\mathrm{D},ab,j}^2\theta_{\mathrm{D},c,j}^2}{\theta_{\mathrm{D},ab,j}^2-\theta_{\mathrm{D},c,j}^2}\frac{T^2 x_j}{e^{x_j}-1} - \frac{\theta_{\mathrm{D},c,j}^2}{\theta_{\mathrm{D},ab,j}^2-\theta_{\mathrm{D},c,j}^2}\frac{T^4 {x_j}^3}{e^{x_j}-1}\right]dx_j\right\}, \tag{24}$$

where $\theta_{\mathrm{D},j}$ is the Debye temperature ($\hbar\omega_{\mathrm{D},j}/k_{\mathrm{B}}$). Here, the ω values in Chapter 5 are used in place of the Debye cutoff frequency, $\omega_{\mathrm{D},j}$. The first term in Equation (24) is identical to Equation (23) from the original DMM. The metal-graphite TBC results by Chen et al. [198]

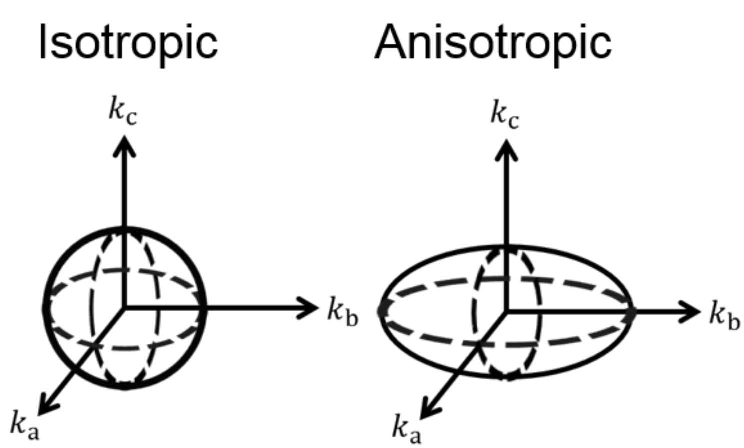

Figure 3-6 Graphical depiction of FBZ for (a) isotropic and (b) anisotropic Debye models.

showed the model still overpredicts the TBC at metal-graphite interfaces when compared to experiments [219].

An update to the A-DMM reported by Li et al. [379] attempts to resolve any discrepancy caused by input parameters. While Chen et al. [198] used the "secant" method (i.e., the slope of secant line connecting the Γ point to the end of the FBZ) to estimate phonon velocity of each branch, this method greatly overpredicts the phonon velocity of the flexural (ZA) branch found in graphite and other layered materials like h-BN. Li et al. [372] instead utilizes the elastic constants to predict the phonon velocities and, cleverly employs a piecewise (PW) linear approximation for the ZA branch specifically. The PW linear approximation is a more accurate representation of the ZA branch because at small wavevector, the ZA branch varies as k^2 which differs from TA and LA branches which vary as k [197]. We refer to this model as PW anisotropic DMM (PWA-DMM). In addition, the cutoff frequencies are determined from the real phonon dispersion as opposed to the Debye approximation ($\omega_{\mathrm{D},j} = v_j k_\mathrm{D}$). The c-axis phonon irradiation ($H_{\mathrm{PWA-DMM}}$) for PWA-DMM is identical to A-DMM (Equation 24) model for the TA and TL1 branches. Following some derivation, the expression for TL2 branch can be given by,

$$\begin{aligned} H_{\mathrm{PWA-DMM,TL2}} &= \frac{k_B^4}{8\pi^2\hbar^3}\left\{\frac{1}{v_{ab,1}^2}\int_0^{x_{\max,ab,1}} \frac{T^4 x^3}{e^x - 1}dx \right. \\ &+ \frac{1}{v_{ab,2}^2}\left[\int_{x_{\max,ab,1}}^{x_{\max,c}} \frac{T^4 x(x-\Delta x)^2}{e^x - 1}dx \right. \\ &\left.\left. + \int_{x_{\max,c}}^{x_{\max,ab,2}} \frac{\hbar^2 v_{ab,2}^2 k_{ab,2}^2/k_B^2 T^2 - (x-\Delta x)^2}{\hbar^2 v_{ab,2}^2 k_{ab,2}^2 x^2/k_B^2 T^2 x_{\max,c}^2 - (x-\Delta x)^2}\frac{T^4 x(x-\Delta x)^2}{e^x - 1}dx\right]\right\} \end{aligned} \tag{25}$$

In Equation 25, $v_{ab,1}$ and $v_{ab,2}$ are the phonon velocities corresponding to the first and second segment of ZA branch using the piecewise linear approximation, respectively, and $\Delta x = \hbar\Delta\omega/k_{\mathrm{B}}T$ where $\Delta\omega = k_{ab,1}(v_{ab,1} - v_{ab,2})$. $k_{ab,1}$ and $k_{ab,2}$ are wavevectors corresponding to intersection of the two piecewise segments and the cutoff wavevector in the ab-plane. The cutoff wave vectors are determined using the relationship $k_{ab}^2 k_c = 6\pi^2 N/V$ and the anisotropy ratio of the real lattice to ensure the correct number of acoustic modes [198].

CHAPTER 4. OXIDATION LIMITED METAL-GRAPHENE INTERFACES

In the following chapter, TDTR is used to investigate the effect of chemisorption (strong bonding) and physisorption (weak bonding) on the TBC at metal-graphene-graphene (M-G-M) interfaces. The interfaces are formed by transferring CVD-grown graphene to the surface of thin metal films followed deposition of metal transducer for TDTR. A sensitivity analysis reveals the impact of the supporting substrate's thermal properties on the TBC measurement which affect the measurability of TBC. The effect of native oxide layers in Ti and Ni films is explored by probing both metal-graphene-metal and metal-metal interfaces. XPS is used to quantify the oxide thickness. The impact of single-layer graphene (SLG) on Au-Au interface is also compelling.

4.1 Sample Fabrication and Characterization

The graphene transfer process was described previously [37, 380] and has been implemented in many studies to study the properties of CVD grown graphene. SLG grown on Cu foil via a CVD process [381] was spin coated (3000 RPM for 60 s) with PMMA (4% wt./vol in Toluene) and cured at 180 °C for 1 min. Because graphene grows on both sides of the foil, the bottom of the foil was etched using 30 s O_2 plasma (250 W, 50 sccm, 60 mTorr) to remove the graphene layer. The Cu foil was then etched using ammonium persulfate (5% wt./vol. in DI water) for 3-6 hours, or until Cu was completely removed. The resulting PMMA-graphene film was transferred to the surface of the target substrate and allowed to dry in the ambient. The substrates were then coated with an additional layer of PMMA in order to relax the wrinkles in the graphene [37]. Following the second PMMA coating, acetone was used to dissolve the PMMA film leaving only graphene on the surface of the samples. The samples were then annealed at 250°C in vacuum (5-10 mTorr) for three hours in an attempt to remove residual PMMA [382, 383] and improve conformity of graphene to the substrate [209]. This procedure was repeated for each sample used in this study.

The samples used in this study are referred to as SiO_2, Ti, Ni, and Au samples based upon the target layer on which the graphene is transferred to. Figure 4-1 shows a schematic of the geometry for each of the samples used in this study. The following is a brief description of each sample. The SiO_2 sample was created by transferring SLG to 300 nm thermally grown SiO_2 (measured using a Nanometrics Nanospec 3000 reflectometer) on Si (<100>, ρ=4-7 Ω-cm). Following graphene transfer, the SiO_2 sample was coated with 100

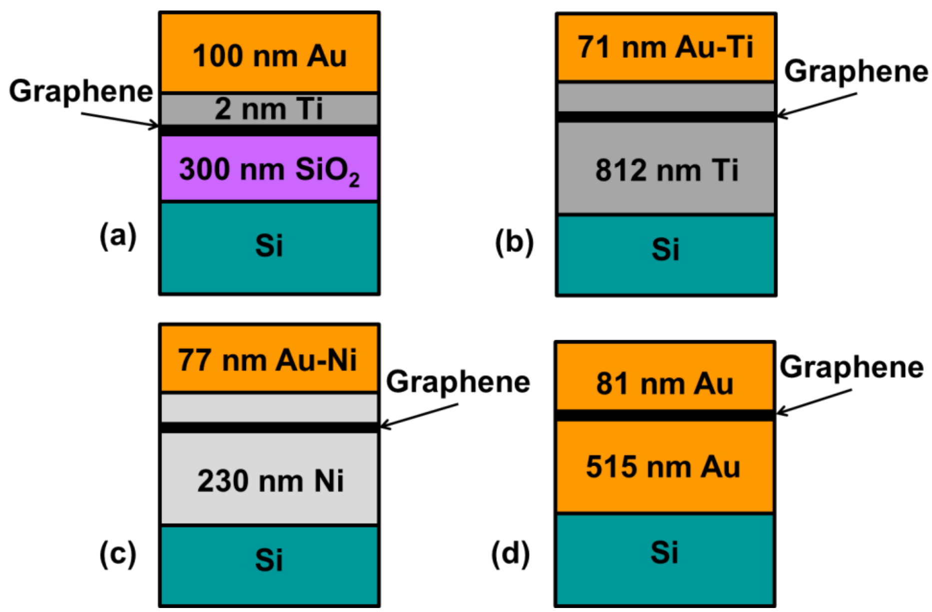

Figure 4-1 Schematic of sample geometries used in TDTR measurements. (a) Graphene was transferred to 300 nm thermally grown SiO_2 100 nm and Au transducer (with 2 nm Ti adhesion layer) deposited by e-beam evaporation. Sandwiched graphene structures with (b) 812 nm Ti, (c) 230 nm Ni, and (d) 515 nm Au deposited by e-beam evaporation. Top metal layers for (b), (c), and (d) were 71 nm Au-Ti, 77 nm Au-Ni, and 81 nm Au, respectively.

nm Au (including a 2 nm Ti adhesion layer between Au and SiO_2) for TDTR measurements. The Ti, Ni, and Au samples were created by transferring graphene to 812 nm thick Ti, 230 nm thick Ni, and 515 nm Au films on Si using electron-beam evaporation (Denton Explorer). Higher deposition rates of 5 and 3 A/s for Ti and Ni, respectively, were used in an effort to reduce oxidation during deposition [384, 385]. The Ti and Ni samples were coated with 60 nm Au-20 nm Ti and 60 nm Au-20 nm Ni, respectively, without breaking vacuum, while the Au sample was coated with 80 nm Au, to form the M-G-M interfaces. The 60 nm Au-20 nm Ti and 60 nm Au-20 nm Ni layers were treated as composite layers [222] since the TBC at M-M interfaces are typically an order of magnitude higher than at M-semiconductor or M-dielectric interfaces [195, 196]. The TBC values reported here are equivalent to the total thermal conductance of the M-G-SiO_2 or M-G-M interfaces.

The optical microscope image in Figure 4-2(a) shows a 1x1 mm^2 area of SiO_2 coated with graphene. The atomic force microscope image in Figure 4-2(b) shows a typical 1x1 μm^2 area on the surface of the SiO_2 sample. There are inherent wrinkles on the graphene surface resulting from the transfer process [380]. Raman spectroscopy (Renishaw InVia) and XPS (Thermo Scientific K-Alpha$^+$) were used to verify the presence of SLG on the surface of the sample. Figure 4-2(c) shows the resulting Raman spectrum with G peak at ~1591 cm^{-1} and 2D peak ~2678 cm^{-1} and intensity ratio $I(2D)/I(G) \approx 3.1$ which is typical of SLG [386]. The D peak at ~1344 cm^{-1} ($I(D)/I(G) \approx 0.15$) is indicative of disorder/defects in the graphene layer (pristine graphene would have no D peak) which often arise near the sample edge or grain boundaries in graphite or graphene with small crystallite size [387]. The D peak could also arise due to the presence of sp^3 amorphous carbon [388]. To quantify

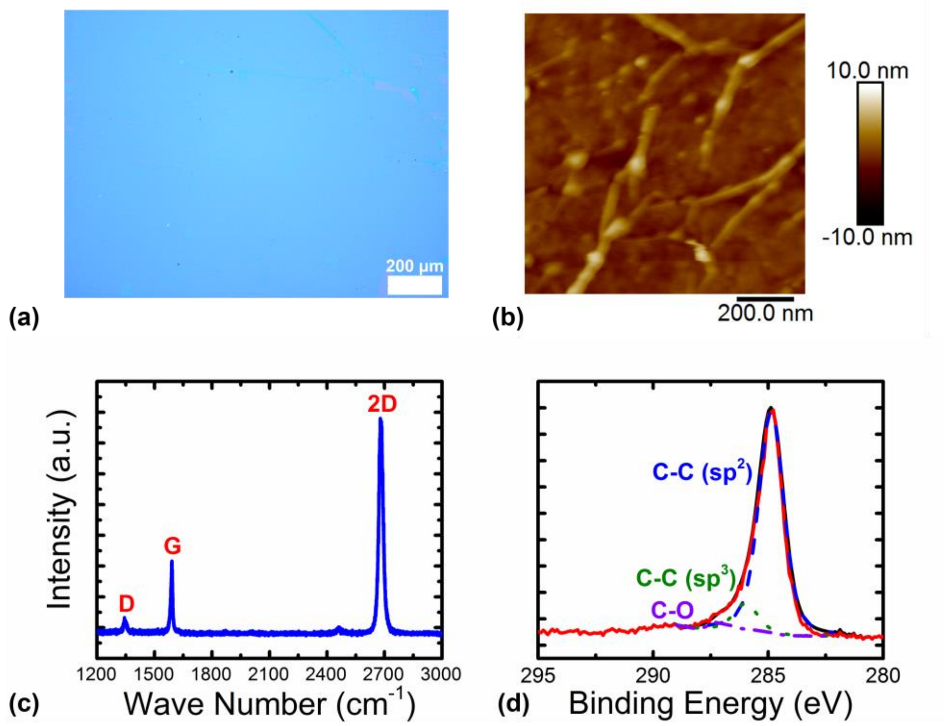

Figure 4-2 (a) Optical microscope image of graphene on the surface of 300 nm SiO_2. Image shows graphene covering an area of 1x1 mm^2. (b) Atomic force microscope images showing 1x1 μm^2 surface of graphene on SiO_2. (c) Raman spectrum for graphene on 300 nm SiO_2 with G peak at ~1591 cm^{-1} and 2D peak at ~2678 cm^{-1}. The relative intensity of the 2D to G peak (I(2D)/I(G) ≈ 3.1) indicates the graphene is single-layer, while the D peak at ~1344 cm^{-1} (I(D)/I(G) ≈ 0.15) is related to disorder/defects in the graphene layer. (d) The deconvolution of the C1s XPS spectrum shows the different types of bonding in the graphene layer.

the disorder in the graphene, the relation of Cancado et al. [389] is used to estimate the distance between defects and defect density of our samples to be ≈31 nm and ≈3.4 X 10^{10} cm^{-2} for an excitation laser wavelength of 532 nm. The large D peak in the graphene samples is higher than some earlier studies but comparable to TDTR studies on transferred CVD-grown graphene [221]. However, the goal of this study is to compare the TBC for different M-G interfaces which we are still able to do since the graphene quality is constant across all samples. Figure 4-2(d) shows the deconvolution of the C1s XPS spectrum with labeled peaks indicating the different types of bonding present in our graphene sample.

The $1/e^2$ diameters of the pump and probe beams were measured using a beam profiler (DataRay Inc. Beam'R2) and were approximately 20 and 8 µm, respectively. The pump and probe laser powers were 40-50 mW and 7-10 mW, respectively. Data fitting was performed over probe delay times of 0.2 to 7 ns. The transducer used for all samples was Au, which precluded the use of picosecond acoustics [341] to determine the transducer thickness since the piezoreflectivity (i.e., the change in reflectance with strain) of Au is small near a wavelength of 800 nm [228]. Reference glass slides were co-deposited during each metal deposition in order to determine film thickness and thermal conductivities of the metal layers. Profilometry (KLA-Tencor P-15) and AFM (Veeco Dimension 3100) measurements performed on reference glass slides were used to determine the height of the thick metal films underneath the graphene interface and the transducer thicknesses (i.e., the metal layer deposited on top of the graphene). The bottom Ti, Ni, and Au films were measured to be 812, 230, and 515 nm thick, respectively, and the Au-Ti, Au-Ni, and Au transducers were 71, 77, and 81 nm thick, respectively.

The thermal conductivity of the metal layers was determined by measuring the RT electrical conductivity in conjunction with the Wiedemann-Franz law: $L_0 = k/\sigma T$, where k is thermal conductivity, σ is electrical conductivity, T is absolute temperature, and L_0 is the Lorenz number which is equal to 2.44×10^{-8} $\mathrm{W\Omega K^{-2}}$ [390]. Electrical conductivity measurements were performed on reference glass slides using a four-point probe technique. The resulting thermal conductivities of the 812 nm Ti, 230 nm Ni, and 515 nm Au were 6.6, 50, and 200 W/m-K, respectively. The thermal conductivity of the 71 nm Au-Ti and 79 nm Au-Ni composite transducers were measured to be 132 and 131 W/m-K, respectively. The thermal conductivity of the 102 nm Au and 81 nm Au transducers were measured to be 185 and 200 W/m-K, respectively. The metal film thermal conductivities were treated as constants during data fitting, unless otherwise stated.

4.2 Sensitivity Analysis

Figure 4-3(a) shows the sensitivity to various parameters in the measurements performed on the SiO_2 sample, including thickness of the Au transducer layer, d_{Au}, SiO_2

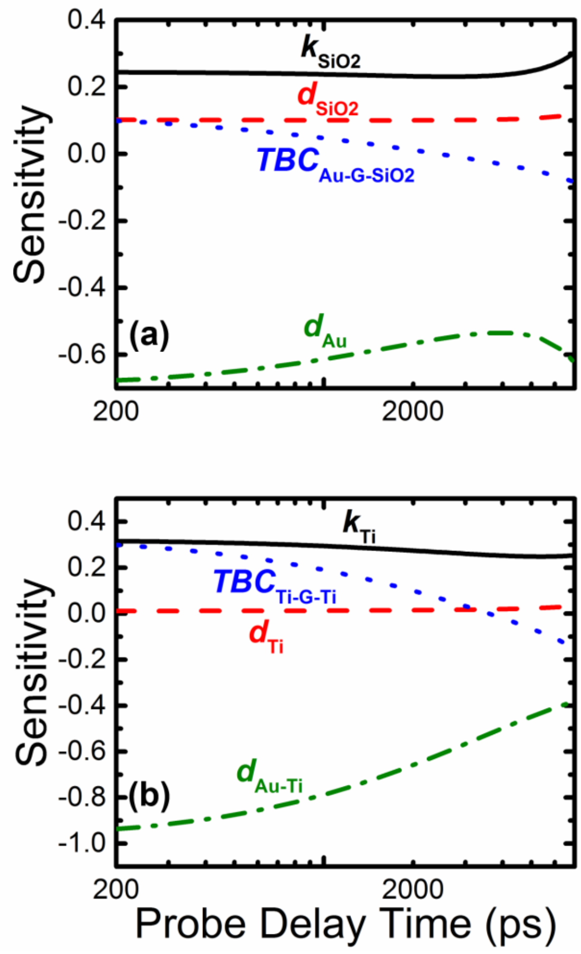

Figure 4-3 (a) Sensitivity to thickness of the Au transducer layer (green-dash-dot), d_{Au}, SiO_2 thermal conductivity (black-solid) and thickness (red-dash), k_{SiO2} and d_{SiO2}, respectively, and TBC at Au-G-SiO_2 interface (blue-dot), $TBC_{\mathrm{Au-G-SiO2}}$, (b) Sensitivity to various parameters in Ti sample including bottom Ti thermal conductivity (black-solid), k_{Ti}, TBC at Ti-G-Ti interface (blue-dot), $TBC_{\mathrm{Ti-G-Ti}}$, bottom Ti thickness (red-dash), d_{Ti}, and Au-Ti transducer thickness (green-dash-dot), $d_{\mathrm{Au-Ti}}$.

thermal conductivity, k_{SiO2}, and TBC at Au-G-SiO_2 interface, $TBC_{\mathrm{Au-G-SiO2}}$. The measurements showed negligible sensitivity to Au transducer thermal conductivity; however, there was significant sensitivity to the thickness of the transducer and SiO_2 thermal conductivity. The sensitivity to TBC was low due to the low thermal conductivity of the SiO_2 layer. This will be discussed in more detail in the next paragraph. In addition to TBC at Ti-G-Ti interface, $TBC_{\mathrm{Ti-G-Ti}}$, TDTR measurements on the Ti sample were sensitive to bottom Ti thermal conductivity, k_{Ti}, bottom Ti thickness, d_{Ti}, and Au-Ti transducer thickness, $d_{\mathrm{Au-Ti}}$. The sensitivity of the model to these parameters is shown in Figure 4-3(b). There was negligible sensitivity to the thermal conductivity of Au-Ti transducer, $k_{\mathrm{Au-Ti}}$. Like the SiO_2 sample, the sensitivity to TBC at the Ti-G-Ti interface was low compared to Ni and Au samples due to low thermal conductivity of the bottom Ti layer. The measurements on the Ni and Au samples showed sensitivity to TBC at Ni-Si and Au-Si interfaces, $TBC_{\mathrm{Ni-Si}}$ and $TBC_{\mathrm{Au-Si}}$, respectively, as well as bottom Ni and Au film thickness, d_{Ni} and d_{Au}, respectively. Sensitivity to the thermal conductivity of Au-Ni and Au transducers, $k_{\mathrm{Au-Ni}}$ and k_{Au}, were negligible.

Table 4-1 Summary of TBC values at M-G-SiO_2 and M-G-M interfaces. Statistical uncertainty analysis (MC simulations) was performed to determine upper/lower uncertainty bounds.

Sample	*TBC* (MW/m^2-K)	Unc. (MW/m^2-K)
Au-G-SiO_2	27.7	+2.9/-2.4
Ti-G-Ti	30.9	+2.9/-2.7
Ni-G-Ni	28.2	+6.2/-9.6
Au-G-Au	28.9	+5.6/-4.5

Comparing the Kapitza length [391] ($L_{\mathrm{K}} = \frac{k}{TBC}$) of an interface, where k is the thermal conductivity of the underlying layer, to thickness (d) of the underlying layer, the larger value will limit heat diffusion in the sample. The result is higher sensitivity to the interface or layer in question. For the 812 nm Ti layer, with thermal conductivity of 6.6 W/m-K and using TBC value from Table 4-1, L_{K} is 213 nm, much lower than the Ti layer thickness. The thermal conductivity of the bottom Ni layer was ~7.5 times higher than the bottom Ti layer, while the thermal conductivity of the bottom Au layer was ~30 times higher. L_{K} of the underlying Ni and Au layers were 1.77 and 6.92 μm, respectively. As a

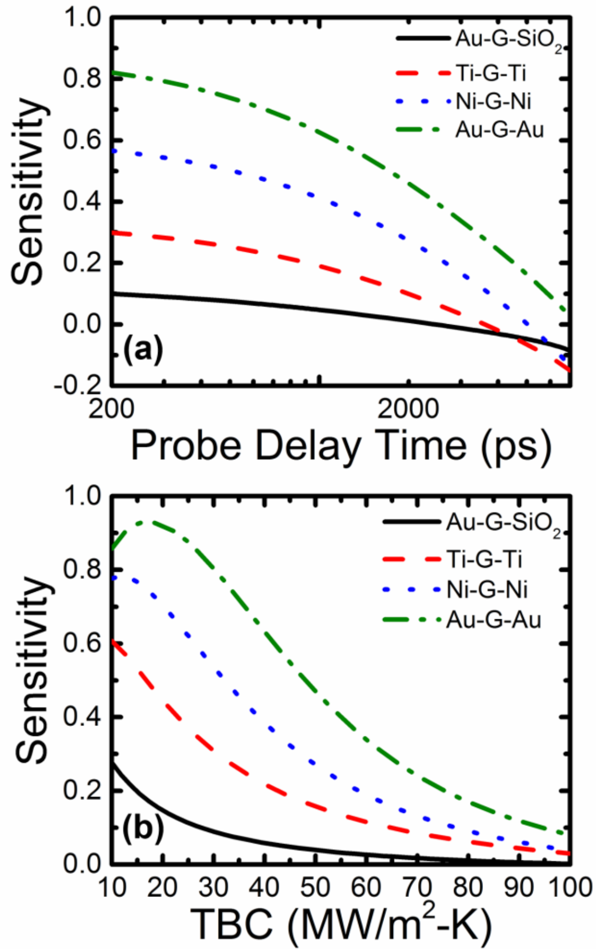

Figure 4-4 Comparison of sensitivity of TBC at Au-G-SiO_2 (black-solid), Ti-G-Ti (red-dash), Ni-G-Ni (blue-dot), and Au-G-Au (green-dash-dot) interfaces (a) as a function of delay time and (b) for different TBC values at a delay time of 200 ps.

result of the high L_{K} values, the sensitivity to TBC at Ni-G-Ni and Au-G-Au interfaces was much higher. This is illustrated in Figure 4-4 using average TBC values found in Table 4-1. Figure 4-4(a) compares sensitivity to TBC at M-G-SiO_2 and M-G-M interfaces as a function of delay time. The sensitivity to Au-G-Au interface across this range was higher than M-G-SiO_2 and other M-G-M interfaces as a result of higher L_{K}. Figure 4-4(b) shows a comparison of sensitivity to TBC at these interfaces for TBC values ranging from 10 to 100 MW/m^2-K at a delay time of 200 ps. Thermal conductivity of the underlying layer in SiO_2 and Ti samples was used as a fitting variable due to low sensitivity to TBC while these parameters could be held constant in Ni and Au samples.

4.3 TBC at Metal-Graphene-Oxide and Metal-Graphene-Metal Interfaces

The TBC was measured in areas with and without graphene on the SiO_2 sample for comparison. As stated in the preceding paragraph, both TBC and SiO_2 thermal conductivity were used as fitting variables. The resulting SiO_2 thermal conductivity (1.14 W/m-K) was near the bulk value [183]. The average TBC values were 84.9 and 27.7 MW/m^2-K for the Au-SiO_2 and Au-G-SiO_2 interfaces, respectively, which are comparable to previously reported values [208, 223]. The MC method [347, 349] described in Chapter 3 was used to obtain a better estimate of the lower uncertainty bound compared with analytical expressions [288]. A histogram showing the distribution of TBC values at the Au-G-SiO_2 interface and a convergence plot with the 5$^{\mathrm{th}}$, 50$^{\mathrm{th}}$, and 95$^{\mathrm{th}}$ percentiles from a typical MC simulation are shown in Figure 4-5(a) and (b), respectively. The reported TBC values at the Au-SiO_2 and Au-G-SiO_2 interfaces, 84.7 and 27.7 MW/m^2-K, respectively, are the average of the 50$^{\mathrm{th}}$ percentiles from each MC simulation. The upper and lower uncertainty

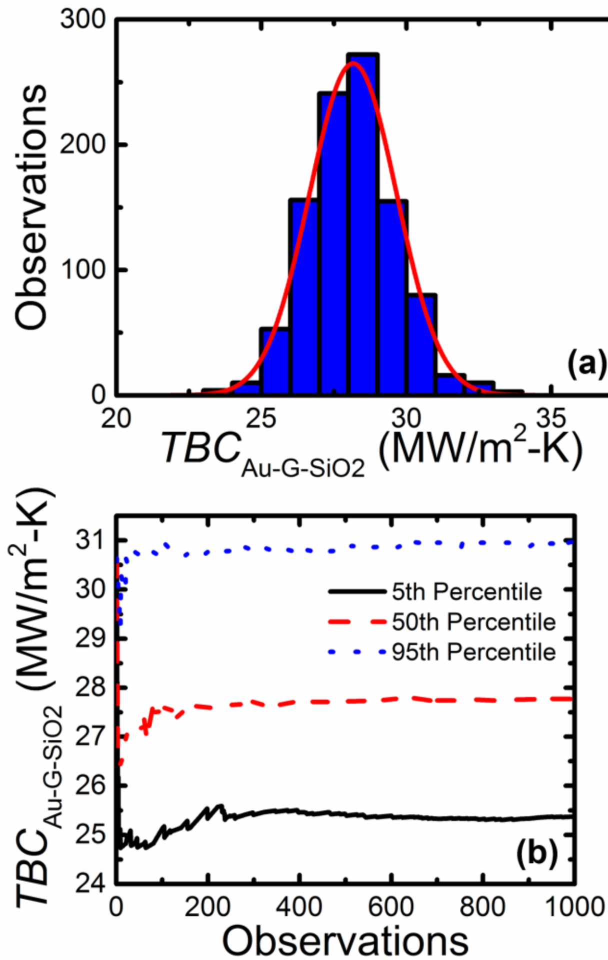

Figure 4-5 Results of a typical Monte Carlo simulations for measurements performed on the SiO_2 sample. (a) A histogram showing the distribution of TBC values at Au-G-SiO_2 interface. (b) Convergence plot showing the 5th, 50th, and 95th percentile. The 50th percentile is taken as the TBC value, while the 95th and 5th percentiles represent the upper and lower uncertainty bound, respectively.

bounds, the average of the 95th and 5th percentiles, respectively, were +2.9/-2.4 MW/m^2-K for the Au-G-SiO_2 interface.

The TBC at M-G-M interfaces were in a similar range as the SiO_2 sample. The thermal conductivity of the underlying Ti layer was used as a fitting parameter along with TBC at Ti-Ti and Ti-G-Ti interfaces. The resulting data fits are shown in Figure 4-6(a). The Ti thermal conductivity from TDTR was approximately 9.6 W/m-K, slightly higher than our value of 6.6 W/m-K using the Wiedemann-Franz law which measures the electronic contribution to thermal conductivity. An increased lattice contribution caused by metal oxidation may be the source of the difference in thermal conductivity observed using TDTR [390]. In addition, the Lorenz number, L_0, may differ from the theoretical value (2.44×10^{-8} WΩK^{-2}) for various metals [392] where higher Lorenz numbers can arise from increased lattice contribution. Using the k (9.6 W/m-K) value from TDTR and

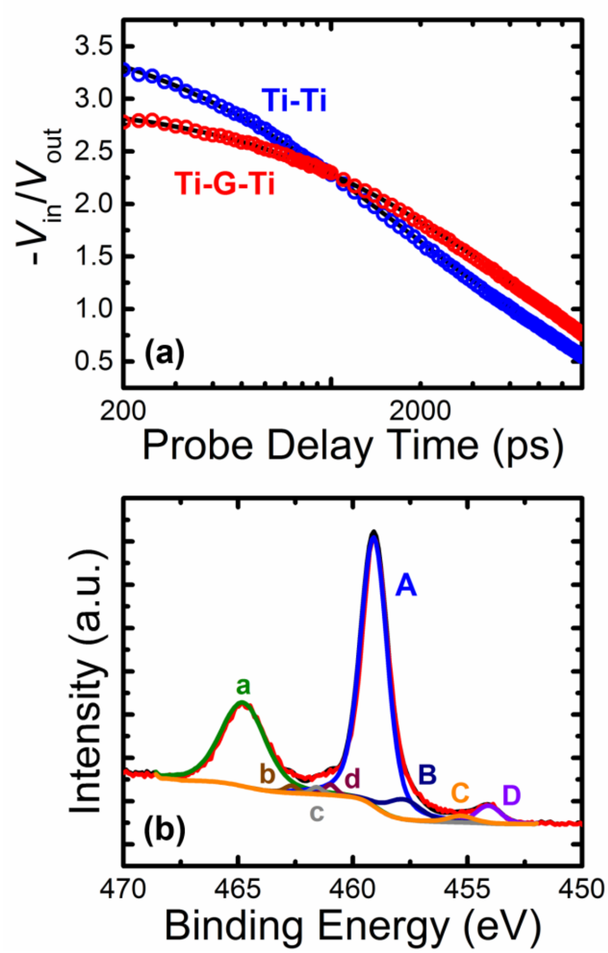

Figure 4-6 (a) Comparison of typical data fits for Ti sample. (b) Ti2p XPS spectrum with peaks labeled corresponding to TiO_2 (A and a) and the suboxides Ti_2O_3 (B and b), TiO (C and c), and Ti (D and d).

measurement of σ ($9.18 \times 10^{5}\,\frac{\mathrm{S}}{\mathrm{m}}$) from the four-point probe technique to calculate Lorenz number results in a L_0 value of 3.54×10^{-8} WΩK^{-2}.

Average TBC at Ti-Ti and Ti-G-Ti interfaces were 96.1 and 30.9 MW/m^2-K, respectively. The TBC at Ti-Ti interface was an order of magnitude lower than expected for a M-M interface [195, 196], which is attributed to oxidation in the Ti layer and confirmed using XPS. The effect is analogous to decreased TBC observed at Al-Si interface in the presence of a native oxide layer [370]. The Ti2p XPS spectrum shown in Figure 4-6(b) was used to determine the thickness of the oxide layer following the method of McCafferty and Wightman [393]. The oxide film was modeled as a mixture of TiO_2 and the suboxides Ti_2O_3 and TiO. The ineleastic electron mean free paths were calculated from the NIST Electron Inelastic Mean Free Path Database [394] using the predictive formula of Gries [395] with densities of 4.5, 4.23, 4.49, and 4.95 g/cm^3 for Ti, TiO_2, Ti_2O_3, and TiO, respectively. The total oxide thickness was found to be ≈2.8 nm with the contribution of each suboxide being 1.3, 1.1, and 0.44 nm for TiO_2, Ti_2O_3, and TiO, respectively. Since graphene forms a chemisorbed interface with Ti, it is quite possible that the TBC would be higher if Ti oxidation can be prevented in the samples.

The TBC of the Ni-Ni interface was an order of magnitude larger than Ni-G-Ni interface (315 versus 28.2 MW/m^2-K), a larger difference than observed for Ti samples. The resulting data fits for measurements on Ni sample are shown in Figure 4-7(a). The TBC at Ni-Ni interface was more than three times the TBC at the Ti-Ti interface. Like the Ti sample, oxidation of Ni layer likely led to lower TBC value at Ni-Ni interface. The Ni2p XPS spectrum is presented in Figure 4-7(b) with main peaks corresponding to Ni, NiO, and $Ni(OH)_2$ [396]. However, unlike Ti, the native oxide layer formed on the Ni surface

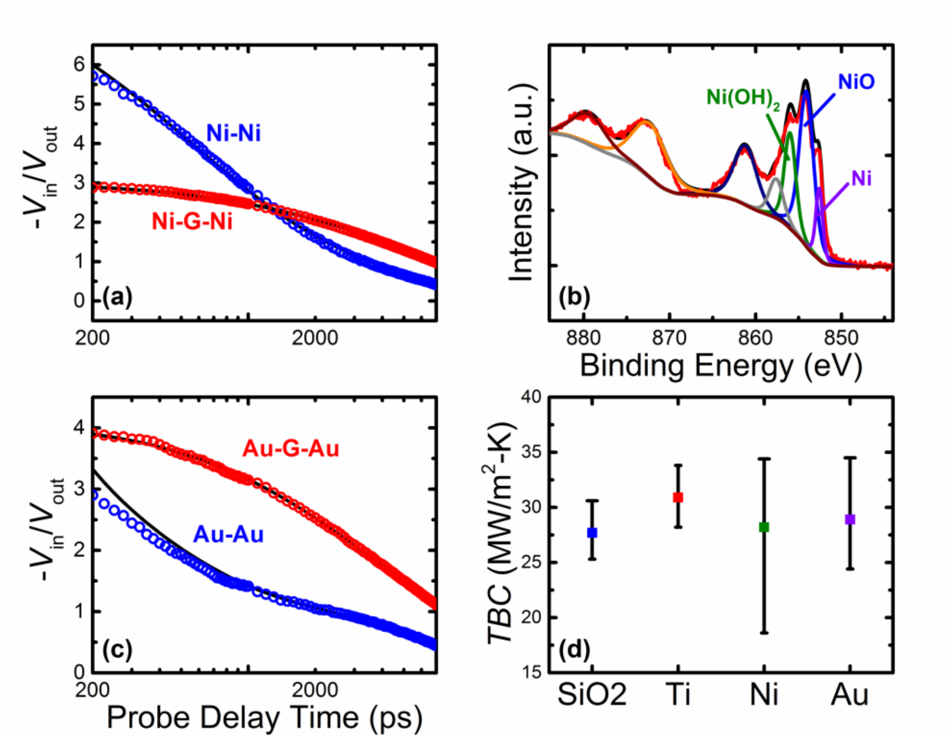

Figure 4-7 Typical data fit for (a) Ni and (c) Au samples used in this study. (b) Ni2p XPS spectrum with main peaks associated with Ni, NiO, and Ni(OH)$_2$. (d) Comparison of TBC values at graphene interfaces (e.g. Au-G-SiO$_2$, Ti-G-Ti) for all samples used in this study (also listed in Table 4-1).

was not treated as a multilayer stack with contributions from each oxidation state. Instead, the thickness of the mixed oxide/hydroxide film on the Ni sample was 2.5 nm estimated using the method of Strohmeier [397-399] with contributions from NiO and Ni(OH)$_2$.

The sensitivity to TBC at Au-Au interface was extremely low due to the high TBC at this interface. Gundrum et al. [195] reported TBC at Al-Cu interface to be 4 GW/m^2-K at RT; we expect TBC at Au-Au interface is much higher than this value since Au does not form an oxide [400] like Al and Cu. Wilson et al. [196] reported TBC of 14 GW/m^2-K at Pd/Ir interface. The TBC at this interface may be too high to resolve in the current sample configuration but is estimated to be > 10 GW/m^2-K based on MC results. The average TBC value at Au-G-Au interface was 28.9 MW/m^2-K. A typical data fit for the Au sample used in this study is shown in Figure 4-7(c). A comparison of average TBC values for samples in this study are shown in Figure 4-7(d) and the results are listed in Table 4-1. The error bars shown in Figure 4-7(d) were obtained using the MC method as were the uncertainty values listed in Table 4-1. The two values listed in the uncertainty column correspond to the lower and upper uncertainty bounds, or the 5th percentile and 95th percentile, respectively, from the MC simulations.

The TBC results at M-G-M interfaces presented here were in similar range as previously reported M-G-SiO_2 [208, 221-225], and M-G-M interfaces [209, 210, 226, 227, 401]. The total native oxide layer thickness estimated from the XPS spectra of Ti and Ni samples was 2.8 and 2.5 nm, respectively. Assuming the thermal conductivity of the oxide layers tis 1 W/m-K, this corresponds to a thermal conductance of 357 and 400 MW/m^2-K for Ti and Ni samples. This is much higher than measured TBC value at Ti-G-Ti and Ni-G-Ni interfaces, both of which contribute to the total interfacial thermal conductance [402]. Freedy et al. [225] showed increased TBC with decreased oxide concentration for a 5 nm Ti layer for graphene on SiO_2 at the M-G-SiO_2 interface showing that Ti oxidation, as opposed to graphene surface reactivity [223], is the limiting factor. A similar observation was made at Au-Al_2O_3 and Au-MgO interfaces [229] showing the effect of Ti oxidation on TBC. These studies focused on Ti because of its use as an adhesion layer for metal contacts. The results and observations here agree with these studies and further broaden the notion of reduction in TBC due to oxidation to other metals as we compare the effect on TBC for Ni in addition to Ti.

Further, the difference in metal and metal oxide Debye temperatures (Ti =420 K [179], TiO_2=750 K [403], Ni=495 K [404], NiO=630 K [405]) suggests the chemical interaction plays a major role in the thermal transport at the M-G interface. The chemisorbed interface between graphene and metal may not be formed due to the thin native oxide layer in the bottom Ti and Ni layer which could explain why high TBC was not observed as predicted by previous computational studies [215, 218] even though conductance of oxide layer itself is much greater than the TBC. In addition, the C1s XPS spectra for graphene on Ti and Ni showed no carbide formation at bottom interface which can also affect interfacial properties [406-408]. Gengler et al. [220] reported a decrease in TBC with increased titanium carbide concentration, but the absence of carbide formation here leaves oxidation as the likely hindrance of M-G interaction at the bottom interface.

However, this explanation is insufficient in explaining why the Au sample had similar TBC indicating that the bonding interactions are not the only important consideration for dictating TBC in our samples since the physisorbed sample (Au) was slightly higher than one chemisorbed sample (Ni) but lower than the other (Ti). For example, interface topology has a major effect on M-G TBC [209]. Different deposition methods (e.g., evaporation, sputtering) and deposition conditions (e.g., rate, pressure) can affect the surface roughness of metal films and thus the topology of the M-G interface. The chemisorbed M-G interface is expected to change electronic configuration [203-205] as well as phonon dispersion [211-215] of graphene. Huang et al. [210] showed that thermal transport at Pd-G-Pd interfaces was due to phonons with no significant electronic contribution, which could also explain why no TBC enhancement was observed. Interestingly, the insertion of a monolayer of graphene significantly reduced the TBC at Au-Au interface by more than two orders of magnitude. From this it can be concluded that the electronic contribution to TBC at M-M interfaces is negated by the presence of the graphene.

4.4 Conclusions

This chapter presented TBC measurements at M-M interfaces using TDTR. The metals used here represent chemisorbed (Ti, Ni) and physisorbed (Au) interfaces based on how they interact with graphene. The TBC was similar to previously reported TBC at M-G-SiO_2 and M-G-M interfaces. Oxidation of the bottom Ti (2.8 nm) and Ni layers (2.5 nm) was confirmed using XPS and likely led to decreased TBC at Ti-G-Ti and Ni-G-Ni interfaces by preventing the formation of chemisorbed interface between graphene and metal. Significantly reduced Ti-Ti and Ni-Ni TBC, compared to typical M-M interfaces, confirmed the effect of oxidation. Reducing the oxidation of the bottom Ti and Ni layers should lead to enhanced TBC, a necessary consideration for fabrication of future graphene devices. Also, the insertion of one monolayer of graphene can significantly reduce thermal transport at M-M interface with no oxidation (e.g., Au-Au).

CHAPTER 5. HEXAGONAL BORON NITRIDE-GRAPHENE HETEROSTRUCTURES

In this chapter, the experimentally measured TBC for Ti-graphene (Ti-G), Ti-h-BN, and h-BN-graphene (h-BN-G) interfaces are correlated with theoretical modeling using the diffuse mismatch model (DMM). TDTR is used to estimate the TBC at the interface of h-BN and graphene which is relevant for 2D heterostructures, a promising route to future applications for this class of materials. The DMM typically assume isotropic properties, this is far from valid for the highly anisotropic thermal transport in h-BN and graphene. Instead, the phonon transmission and TBC are predicted using two different forms of DMM developed for anisotropic materials and the contribution of the different phonon modes is demonstrated.

5.1 Sample Fabrication and Characterization

Single-layer graphene (SLG), with some bilayer islands, and few-layer h-BN were grown on Cu foil using separate CVD processes [230] and transferred to the surface of 300 nm thermally-grown SiO_2 (measured using a Nanometrics Nanospec 3000 reflectometer) using a PMMA polymer support (these samples were provided by collaborators at Rice University). Prior to transfer to SiO_2, the underlying Cu foil was etched in $FeCl_3$, and, following transfer, the PMMA was dissolved in acetone and isopropyl alcohol. The samples were annealed at 300°C in vacuum (5-10 mTorr) to remove residual PMMA [383] and improve conformity to the substrate [209]. Raman spectroscopy data was acquired using a Renishaw InVia Raman microscope with 180° backscattering geometry and 488 nm Ar^+ laser focused using a 50X objective lens (NA=0.5). XPS was performed using a Thermo Scientific K-Alpha+ spectrometer with an Al Kα monochromatic X-ray source (1486.6 eV).

In preparation for thermal measurements, the samples were simultaneously coated with Au (3 nm Ti adhesion layer) using electron-beam evaporation to serve as a thermal transducer. Schmidt et al. [219] showed that inclusion of 5 nm Ti adhesion layer nearly doubled the TBC at Al-graphite interface. Therefore, the interfaces considered here are Ti-G-SiO_2 or Ti-h-BN-SiO_2 despite Au layer as the thermal transducer. The sample geometries used in this study are shown in Figure 5-1(a)-(c). The actual film thickness of 77 nm was measured on co-deposited glass slide using AFM (Veeco Dimension 3100).

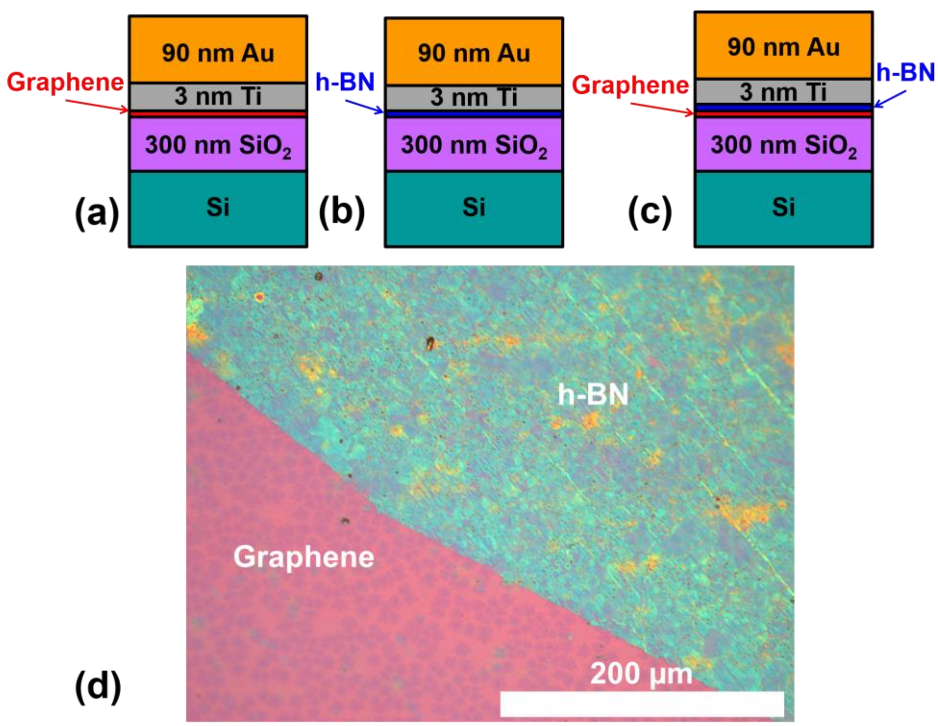

Figure 5-1 The samples used in this study are CVD grown (a) graphene, (b) h-BN, and (c) h-BN-G. Samples were coated with a Au thermal transducer (3 nm Ti adhesion layer) for TDTR measurements. The interfaces are considered Ti-G-SiO_2 or Ti-h-BN-SiO_2 in accordance with previous studies where a 5 nm Ti adhesion layer nearly doubled the TBC at Al-graphite interface. (d) An optical microscope image (20x) showing a ~0.5x0.5 mm^2 area on the surface of h-BN-G sample.

The pump and probe $1/e^2$ radii were ~5 and ~3 µm, respectively, measured with a DataRay Inc. Beam'R2 beam profiler. Pump and probe powers of 10 and 4 mW, respectively, were used. The arrival time of the probe was delayed up to 5 ns relative to the pump. MC simulations were used to determine uncertainties associated with TBC estimation [347, 349]. The optical microscope image in Figure 5-1(d) shows a 1x1 mm^2 area of SiO_2 coated with mostly SLG and h-BN.

Figure 5-2(a) and (b) shows the Raman spectra from the samples used in this study. The graphene sample (Figure 5-2(a)) displayed G peak at 1592 cm^{-1} (E_{2g} mode near the Γ point) [387] and 2D peak 2703 cm^{-1} (A_{1g} mode near the K point) [409] and intensity ratio I(2D)/I(G) ≈ 2.2 [386] showing the sample is single-layer. However, the shift in peak positions and reduced I(2D)/I(G) ratio suggests some p-type doping [410, 411] previously

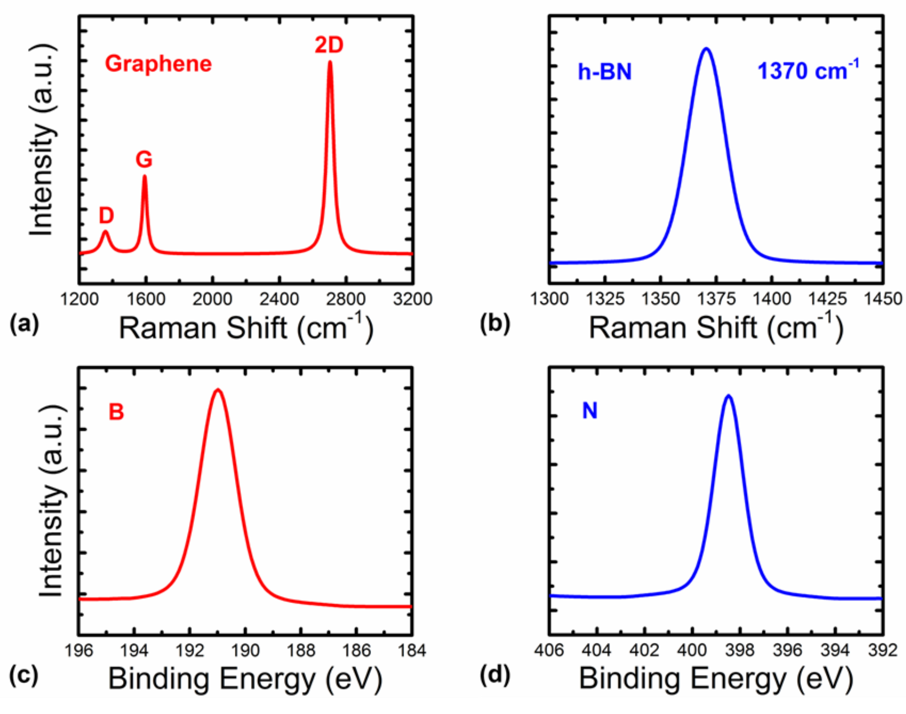

Figure 5-2 (a) Graphene and (b) h-BN Raman spectra. The intensity ratio I(2D)/I(G) ≈ 2.2 in (a) indicates graphene sample is single-layer. High resolution XPS spectra for h-BN samples showing (c) B and (d) N peaks at 191 and 398 eV, respectively. From the XPS data, we determined the stoichiometry of our h-BN sample was 1.17:1 (B:N).

attributed to residual PMMA [382]. The D peak at 1356 cm^{-1} arises from disorder in the graphene layer. Figure 5-2(b) shows the h-BN Raman spectrum with peak blue-shifted to ~1370 cm^{-1}, corresponding to the in-plane E_{2g} mode, compared to the characteristic peak at ~1366 cm^{-1} for bulk h-BN [412]. This shift could be caused by stress in the film resulting from the growth process, substrate-interlayer interaction, or crystallite size [413-415]. A comparison of the graphene and h-BN-graphene Raman spectra (not shown) did not display new peaks in the range of 1200-3200 cm^{-1} which would suggest coupling between the 2D layers [416-419]. There was simply peak broadening around 1360 cm^{-1} as a result of the h-BN layer. A more extensive Raman study may reveal shear or layer-breathing modes at lower frequencies. The high resolution XPS spectra in Figure 5-2(c) and (d), respectively, show B and N peaks at binding energies of 191 and 398 eV, respectively. From the XPS data, the stoichiometry of our h-BN sample was 1.17:1 (B:N) [420].

5.2 TBC Measurement and Analysis Using TDTR

The TBC at Ti-G-SiO_2 and Ti-h-BN-SiO_2 interfaces were 30.6 (+6.2/-4.2) and 33.7 (+9.8/-5.3) MW/m^2-K, respectively. The TBC at Ti-h-BN-G-SiO_2 interface was 18.3 (+4.0/-2.7) MW/m^2-K. The TDTR signals are compared in Figure 5-3(a). The total interfacial thermal conductance per unit area can be ascribed to the metal-h-BN-G-SiO_2 interfaces acting in series, as in the case of a thin film sample between two solids [402]. Therefore, a one-dimensional thermal resistance network is used to estimate the TBC at h-BN-G interface. This method was used previously [208, 221-223, 401] where the heat transport across M-G-SiO_2 and M-G-M interfaces was treated as the resistances of the decoupled M-G and G-SiO_2 (or G-M) interfaces acting in series. Zheng et al. reevaluated this analysis recently suggesting long wavelength phonons may traverse both interfaces

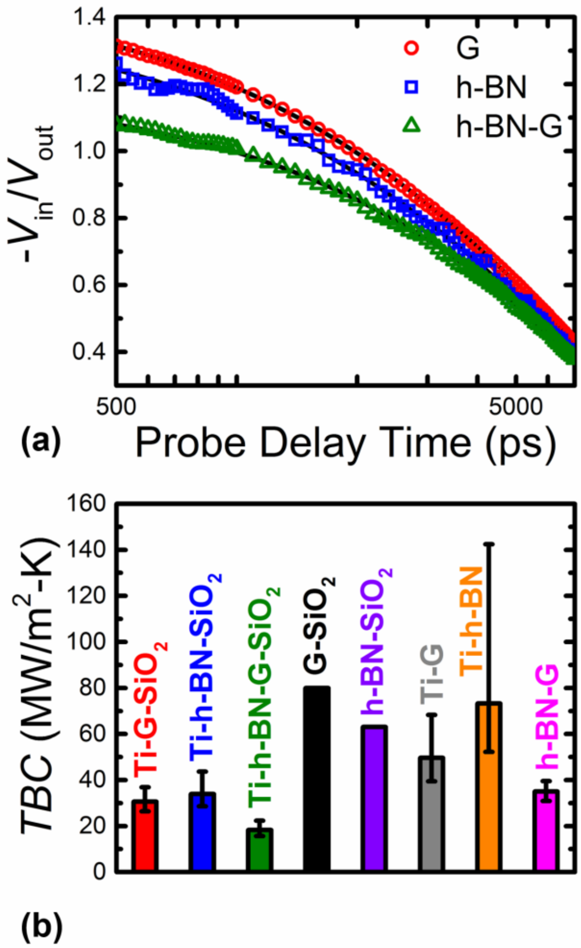

Figure 5-3 (a) TDTR signal comparisons for three samples used in this study. (b) Summary of TBC results from TDTR measurements and thermal resistor network. Ti-G-SiO$_2$, Ti-h-BN-SiO$_2$, and Ti-h-BN-SiO$_2$ values measured using TDTR. Error bars were calculated using the MC method. G-SiO$_2$ [312] and h-BN-SiO$_2$ [421] data taken from literature. Ti-G, Ti-h-BN, and h-BN-G TBC values were estimated using series resistance approximation.

through a process similar to the heat transport in superlattices [332]. Nevertheless, we apply the method here in the following manner. Using the relationship, $1/TBC_{\mathrm{Ti-G-SiO2}} = 1/TBC_{\mathrm{Ti-G}} + 1/TBC_{\mathrm{G-SiO2}}$, we can determine $TBC_{\mathrm{Ti-G}}$. Similarly, the $TBC_{\mathrm{G-SiO2}}$ term can be replaced by $TBC_{\mathrm{h-BN-SiO2}}$ to determine $TBC_{\mathrm{Ti-h-BN}}$. The thermal conductance of the h-BN and G layers were much greater than the interfacial TBC and were therefore neglected.

The $TBC_{\mathrm{G-SiO2}}$ and $TBC_{\mathrm{h-BN-SiO2}}$ values were previously reported for SLG (~80 MW/m^2-K) [312] and monolayer h-BN (~63 MW/m^2-K) [421] using the 3ω technique. Using these values, the resulting $TBC_{\mathrm{Ti-G}}$ and $TBC_{\mathrm{Ti-h-BN}}$ are 49.6 (+18.7/-10.2) and 73.3 (+69.1/-21.1) MW/m^2-K. The uncertainty bounds were determined using the upper/lower limits from the MC simulations for Ti-G-SiO_2 and Ti-h-BN-SiO_2 interfaces. We use these values and formulate a new relationship, $1/TBC_{\mathrm{Ti-h-BN-G-SiO2}} = 1/TBC_{\mathrm{Ti-h-BN}} + 1/TBC_{\mathrm{h-BN-G}} + 1/TBC_{\mathrm{G-SiO2}}$, and estimate $TBC_{\mathrm{h-BN-G}}$ to be 35.1 (+4.5/-4.2) MW/m^2-K. The TBC values are summarized in Figure 5-3(b). When compared with previous values in literature, our TBC value is greater than 7.4 MW/m^2-K reported by Chen et al. [243] and 5-10 MW/m^2-K reported by Kim et al. [246]. However, our value is less than 52.2 MW/m^2-K reported by Liu et al. [245], which we attribute to surface roughness resulting from the CVD growth process and PMMA residue following the transfer process. This value is also in a similar range as TBC (30 – 50 MW/m^2-K) for different lattice stacking configuration predicted using first principles AGF simulations [241].

5.3 DMM-Based TBC Analysis

Next, the anisotropic DMM models discussed in Section 3.2 are implemented to predict the phonon transmission and TBC at Ti-G, T-h-BN, and h-BN-G interfaces. Phonon velocities were calculated using the elastic constants for Ti [378], graphite [422], and h-BN [423]. The cutoff frequencies for each branch were determined from the published dispersion relations [197, 424, 425], and the Debye temperature for each branch corresponds to these frequencies. Following Chen et al. [198], the cutoff wavevectors are determined using the relationship $k_{ab}^2 k_c = 6\pi^2 N/V$ and the anisotropy ratio of the real lattice to ensure the correct number of acoustic modes. Also, the dispersion relation is unfolded along c-axis because of the relatively high velocity of optical modes in that direction. Table 5-1 lists the input parameters for both models, where $v_{ab,2}$, $\omega_{ab,1}$, and $k_{ab,1}$ are not used in the A-DMM model. Unlike Li et al. [379], the same input parameters are used in both models for direct comparison.

Table 5-1 Input parameters for A-DMM and PWA-DMM models. The phonon velocities were calculated using the elastic constants for Ti [378], graphite [422], and h-BN [423] and cutoff frequencies for each branch were determined from the published dispersion relations [197, 424, 425]. The wavevectors, $\boldsymbol{k_{ab,1}}$ and $\boldsymbol{k_{ab,2}}$, frequencies $\boldsymbol{\omega_{ab,1}}$ and $\boldsymbol{\omega_{ab,2}}$, and phonon velocities $\boldsymbol{v_{ab,1}}$ and $\boldsymbol{v_{ab,2}}$, for TL2 branch were determined using the analysis of Li et al. [426]. $\boldsymbol{v_{ab,2}}$, $\boldsymbol{\omega_{ab,1}}$, and $\boldsymbol{k_{ab,1}}$ are not used in the A-DMM model.

Branch	Parameters	Graphene	h-BN
TA	v_c (m/s)	1329	1915
	v_{ab} (m/s)	13935	12364
	ω_c (10^{12} rad/s)	8.24	9.98
	ω_{ab} (10^{12} rad/s)	190	166
TL1	v_c (m/s)	1329	1915
	v_{ab} (m/s)	21628	19652
	ω_c (10^{12} rad/s)	8.24	9.98
	ω_{ab} (10^{12} rad/s)	231	202
TL2	v_c (m/s)	4013	3586
	$v_{ab,1}$ (m/s)	1329	1915
	$v_{ab,2}$ (m/s)	7485	4396
	ω_c (10^{12} rad/s)	22.8	22.8
	$\omega_{ab,1}$ (10^{12} rad/s)	5.34	4.08
	$\omega_{ab,2}$ (10^{12} rad/s)	100	61.7
	$k_{ab,1}$ (10^{10} m^{-1})	0.402	0.213
	$k_{ab,2}$ (10^{10} m^{-1})	1.83	1.80

The DMM does not consider the quality of the interface (e.g., bonding, roughness), which varies from sample to sample; therefore, α_{12} is held constant and its value is determined for each interface by fitting both DMM models to our RT TDTR measurements

(Table 5-2). As a result, only the phonon irradiation from material 1 (e.g., Ti in the case of Ti-G and Ti-h-BN interface) needs to be considered [191]. Thus, when utilizing the fitted values, $\alpha_{12,\mathrm{fit}}$, the A-DMM and PWA-DMM models differ from each other and from the original DMM (Equation 23) only when considering the h-BN-G interface. The $\alpha_{12,\mathrm{fit}}$ values listed in Table 5-2 are very insightful. As expected, $\alpha_{12,\mathrm{fit}}$ for the Ti-G and Ti-h-BN are identical for the A-DMM and PWA-DMM models. They are also similar order of magnitude (~10^{-2}) for $\alpha_{12,\mathrm{fit}}$ at metal-graphite interfaces [208, 219] reported in previous studies. We must point out that Schmidt et al. [219] assumed a sine-type (or Born-von Karman) [372] dispersion for metals and effective 2D Debye density of states [377] in graphite. Also, the velocities of each phonon polarization were lumped into a single, average velocity. Koh et al. [208] used a linear (Debye) dispersion for Au. $\alpha_{12,\mathrm{fit}}$ for h-BN-G interface predicted by the PWA-DMM was nearly an order of magnitude larger than the value predicted by the A-DMM (see Table 5-2). The reason for this discrepancy is discussed below.

Table 5-2 Fitted phonon transmission coefficients, $\alpha_{12,\mathrm{fit}}$, used in DMM analysis determined by fitting to RT TDTR data.

Interface	A-DMM [377]	PWA-DMM [198]
Ti-G	0.05424	0.05424
Ti-h-BN	0.08016	0.08016
h-BN-G	0.02494	0.2287

The ratio of α_{12}, calculated using phonon irradiation (Equations 24 and 25) and the relationship $\alpha_{12} = H_2/(H_1 + H_2)$, to $\alpha_{12,\mathrm{fit}}$ values from Table 5-2 is compared in Figure 5-4(a). While Li et al. [379] makes an elastic assumption and calculates $\alpha_{12}(\omega)$, we assume inelastic scattering [427] in accordance with the A-DMM model and calculate $\alpha_{12}(T)$ allowing phonons of all frequencies in h-BN and graphene to participate. For the h-BN-G interface, α_{12} is expected to be near 0.5 for both models due to the similar vibrational properties of graphene and h-BN [197, 425]. The graph of $\alpha_{12}/\alpha_{12,\mathrm{fit}}$ in Figure 5-4(a) shows a weak temperature dependence above 200 K for both the A-DMM model (solid lines) and PWA-DMM (dashed lines).

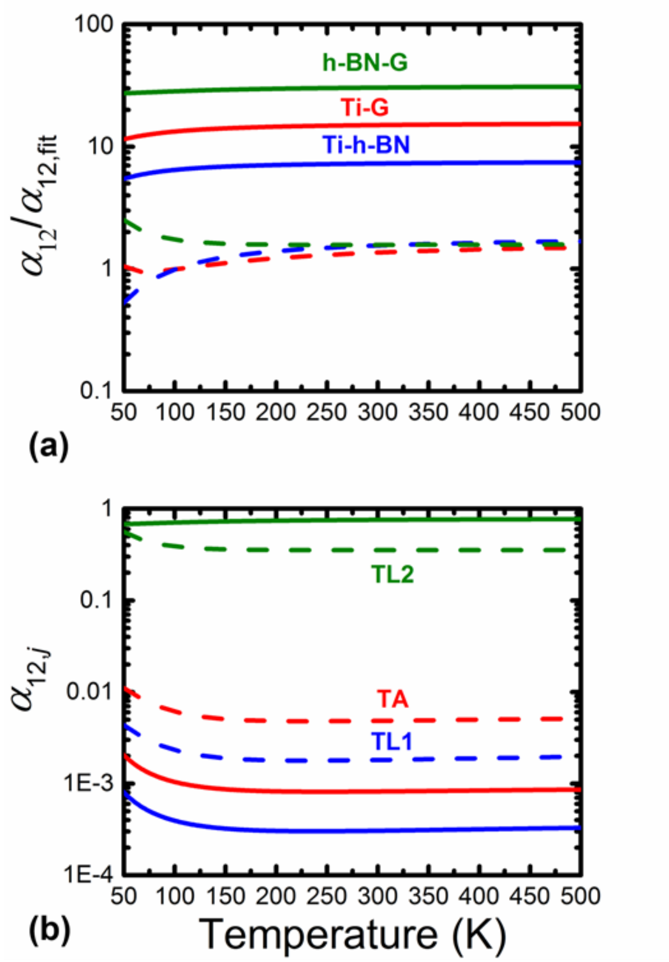

Figure 5-4 (a) Ratio of transmission coefficients, $\alpha_{12}/\alpha_{12,\mathrm{fit}}$, for A-DMM (solid lines) and PWA-DMM (dashed lines), where α_{12} is calculated from phonon irradiation (Equations 24 and 25) and the relationship $\alpha_{12} = H_2/(H_1 + H_2)$ and $\alpha_{12,\mathrm{fit}}$ is determined from RT TDTR data. The ratio $\alpha_{12}/\alpha_{12,\mathrm{fit}}$ depend weakly on temperature above 200 K. (b) The transmission coefficient of each phonon branch, $\alpha_{12,j}$, highlights the importance of the TL2 branch to total transmission, α_{12}.

The discrepancy between α_{12} and $\alpha_{12,\mathrm{fit}}$ was much larger for A-DMM compared to PWA-DMM model. At RT $\alpha_{12}/\alpha_{12,\mathrm{fit}}$ for Ti-G and Ti-h-BN interfaces are 14.9 and 7.27, respectively, using the A-DMM model, while there is much better agreement for the PWA-DMM (1.36 and 1.55 for Ti-G and Ti-h-BN, respectively). The high $\alpha_{12}/\alpha_{12,\mathrm{fit}}$ ratio for the A-DMM for Ti-G and Ti-h-BN interface arises from the much higher phonon irradiation in graphene and h-BN compared to PWA-DMM. The phonon irradiation is proportional to v_{ab}^{-2}, thus the assumption of a constant v_{ab} for TL2 branch, which contributes most to the irradiation [198, 379], results in much higher calculated α_{12} value for A-DMM model. This is the phonon focusing effect [428] whereby cross-plane TBC can be increased with a reduction in in-plane phonon velocity. The same is true for h-BN-G interface where $\alpha_{12}/\alpha_{12,\mathrm{fit}}$ was 30.3 and 1.57 for the A-DMM and PWA-DMM models, respectively. The transmission coefficient for each phonon branch, $\alpha_{12,j}$, is shown in Figure 5-4(b) and further reinforces the importance of the TL2 branch.

Finally, the TBC predicted using $\alpha_{12,\mathrm{fit}}$ are shown in Figure 5-5 along with TBC for Ti-G, Ti-h-BN, and h-BN-G from our TDTR results. Various literature results for h-BN/G [243, 245, 246], M/G [210, 221, 401] and M/graphite [219] interfaces are also shown for comparison. The discrepancy between h-BN-G results for the A-DMM and PWA-DMM models at low temperatures arises from the assumption of constant α_{12}. The phonon wavelength varies as T^{-1} resulting in higher α_{12} at low temperatures where phonon wavelength is much larger than surface roughness leading to decreased scattering [191]. This behavior is captured by the PWA-DMM model but not the A-DMM. Interestingly, the TBC at h-BN/G interface is constant above 200 K for both models. TBC is expected to increase below the Debye temperature [180, 191], which is greater than 1000 K [429] for

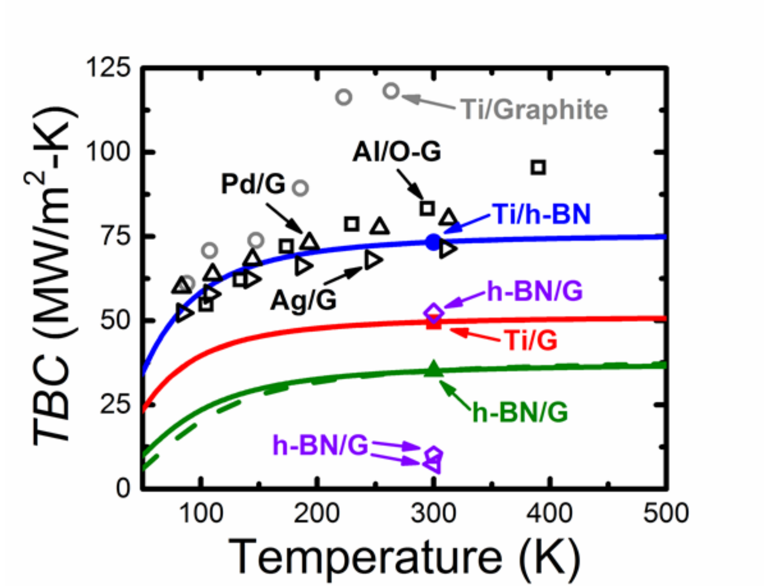

Figure 5-5 Comparison of TBC for Ti-G (red filled square), Ti-h-BN(filled blue square), and h-BN-G (filled green triangle) from this work. DMM results from this work are plotted as solid (A-DMM) and dashed lines (PWA-DMM). TBC values at Ti-G, Ti-hBN, and h-BN-G are estimated assuming series resistances. The DMM results were calculated using $\alpha_{12,\mathrm{fit}}$ values in Table 5-2. Also shown are previously reported of h-BN-G TBC from Chen et al. [243] (open left purple triangle), Liu et al. [245] (open purple diamond), and Kim et al. [246] (open purple trapezoid) using Raman spectroscopy. For further comparison, TBC for various metal-G [Al-O-G (open black square) [221], Pd-G (open up black triangle) [210], and Ag-G (open right black triangle) [401]] and Ti-graphite (open gray circles) [219] interfaces are also shown.

both h-BN and graphene. The observed trend with temperature may be a result of the ZA branch in ab-axis and TA branch in c-axis (i.e., TL2 branch) properties being the dominant contributor to TBC for both A-DMM and PWA-DMM models. The maximum frequency of vibrations (Table 5-1) for the two branches correspond to Debye temperatures of 764 and 174 K, respectively, but the contribution from both remain constant above 200 K.

5.4 Conclusions

To summarize, the TBC at h-BN-G interface was estimated using a series thermal resistor network coupled with TDTR measurements at Ti-G-SiO_2, Ti-h-BN-SiO_2, and Ti-h-BN-G-SiO_2 interfaces. The TBC at h-BN-G interface was 35.1 MW/m^2-K; however, since h-BN and graphene have similar physical structure and acoustic properties the TBC at their interface may be increased by improving sample quality. The phonon transmission predicted using two forms of the DMM for anisotropic materials was compared. The A-DMM model predicts a higher phonon irradiation thus higher transmission coefficient due the assumption of constant velocity of ZA mode across entire the FBZ. The PWA-DMM model uses two different phonon velocities near the center and at edge of the FBZ resulting in better prediction of phonon transmission. The phonon transmission and temperature dependence of TBC confirms the TL2 branch of h-BN and graphene are the dominant contributor when implementing both the A-DMM and PWA-DMM model. This methodology can be extended to other 2D heterostructures to analyze the TBC at the interfaces of 2D layers.

CHAPTER 6. SPATIAL MAPPING OF THERMAL BOUNDARY CONDUCTANCE AT METAL-MOLYBDENUM DISELENIDE INTERFACES

The following chapter presents the 2D spatial variation of the TBC at metal-$MoSe_2$ (M-$MoSe_2$) interfaces. Photolithography allows individual islands of CVD grown $MoSe_2$ to be isolated and probed using TDTR. A modified TDTR technique reduces the measurement time significantly. TDTR traditionally requires mapping the decay of the thermoreflectance signal as a function of time. Here, the TBC is determined by comparing the measured thermoreflectance signal at a single delay time to a correlation curve which predicts the variation of the thermoreflectance signal with TBC. Image clustering provides improved resolution of the optical images and TBC maps allowing distinction between regions with different layer number and TBC value. TDTR performed over the full range of delay times reveal a key finding of the current chapter.

6.1 Sample Fabrication and Characterization

Single-layer $MoSe_2$ flakes were grown on a 310 nm thermally grown SiO_2 through a low-pressure CVD (LPCVD) process, described previously [430, 431], by reacting 0.2 g MoO_3 with 1.2 g Se powder under 40 sccm Ar + 6 sccm H_2 carrier gas resulting in triangular $MoSe_2$ islands (CVD growth was performed at Oak Ridge National Lab). The largest single-layer islands found on the sample were equilateral triangles with 80 µm side length. Individual $MoSe_2$ islands were patterned using Futurrex, Inc.'s NR9-1500PY negative photoresist exposed using a Microtech LaserWriter LW405 system. The

LaserWriter allows for low-throughput, direct-write, photolithographic patterning with a focused laser beam (λ=375 nm) with 0.7 μm minimum resolution. After identifying candidate islands, those with approximately 80 μm side length, 100 μm square windows were drawn above them along with 500 μm square windows at each corner (Figure 6-1(a)). The larger windows were used to locate the 100 μm windows for site-specific TDTR measurements. The optical microscope image (10x objective) in Figure 6-1(b) shows the exposure pattern of $MoSe_2$ islands prior to metal deposition for TDTR measurements.

Following patterning, the samples were coated with Al, with and without a Ti adhesion layer, using electron-beam evaporation to form Al-$MoSe_2$-SiO_2 and Ti-$MoSe_2$-SiO_2 interfaces. The Al-Ti interface can be ignored since the TBC at M-M interfaces is an order of magnitude higher than M-semiconductor or M-dielectric interfaces [195, 196,

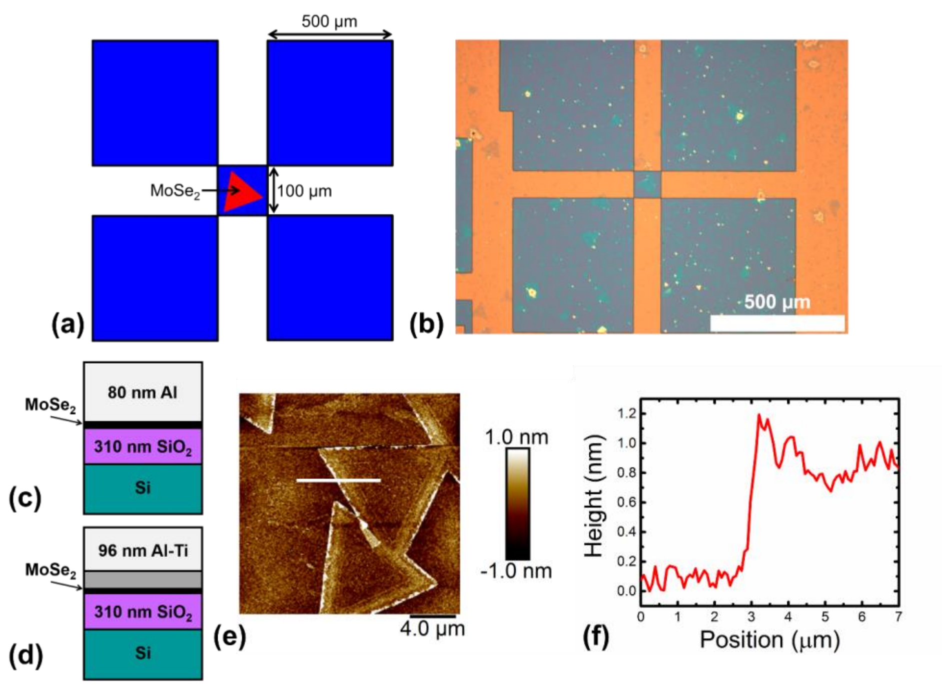

Figure 6-1 (a) Schematic of exposure pattern for $MoSe_2$ islands for metal deposition and thermal measurements. (b) Optical microscope image showing exposed region of sample. (c), (d) Sample geometry used in TDTR measurements. (e) Atomic force microscope image, and (f) Profile of single-layer $MoSe_2$ (~0.7 nm) along the line shown in (e) corresponding to single-layer $MoSe_2$.

349]. Like Schmidt et al. [219] for graphite, Cheaito et al. [432] showed that inclusion of 2 nm Ti adhesion layer was enough to effectively change the TBC at Au-Si interfaces, with little change up to 40 nm Ti. Therefore, with Ti adhesion layer we can consider the interface to be Ti-$MoSe_2$-SiO_2. The TBC values reported here are equivalent to the total thermal conductance of the M-$MoSe_2$-SiO_2 interface. In both geometries, the Al layer acts as an ideal transducer to absorb incident laser energy during thermal measurements because of its relatively large thermoreflectance coefficient at the wavelength of our probe laser (λ=800 nm) [433]. The transducer thicknesses (Figure 6-1(c) and (d)) were measured on co-deposited glass slides using AFM and confirmed using picosecond acoustics [341]. Raman spectroscopy and XPS data were acquired using the previously described Renishaw InVia Raman microscope and Thermo Scientific K-Alpha$^+$ spectrometer, respectively.

The optical contrast of the $MoSe_2$ regions in Figure 6-1(b) can be used to identify single-layer regions [434]. As stated previously, the largest islands on the sample were equilateral triangles with ~80 µm side length. The AFM image in Figure 6-1(e) shows the sample surface and the height of an isolated island was measured to be ~0.7 nm along the line in Figure 6-1(f), confirming the $MoSe_2$ is single-layer [88]. The Raman spectrum (Figure 6-2(a)) shows two distinct peaks at ~244 and ~291 cm^{-1} corresponding to A_{1g} (out-of-plane) and E^1_{2g} (in-plane) modes in $MoSe_2$, respectively [89]. Less pronounced peaks corresponding to B^1_{2g} and E_{1g} modes can also be identified. The Mo 3d (Figure 6-2(b)) and Se 3d (Figure 6-2(c)) high resolution spectra shows the characteristic Mo $3d_{5/2}$ and Mo $3d_{3/2}$ doublet with peak binding energies of 230 and 233 eV, respectively, with slight MoO_x peak, along with Se $3d_{5/2}$ and Se $3d_{3/2}$ doublet peaks at 54.8 and 55.7 eV, respectively, in agreement with the previous studies [435].

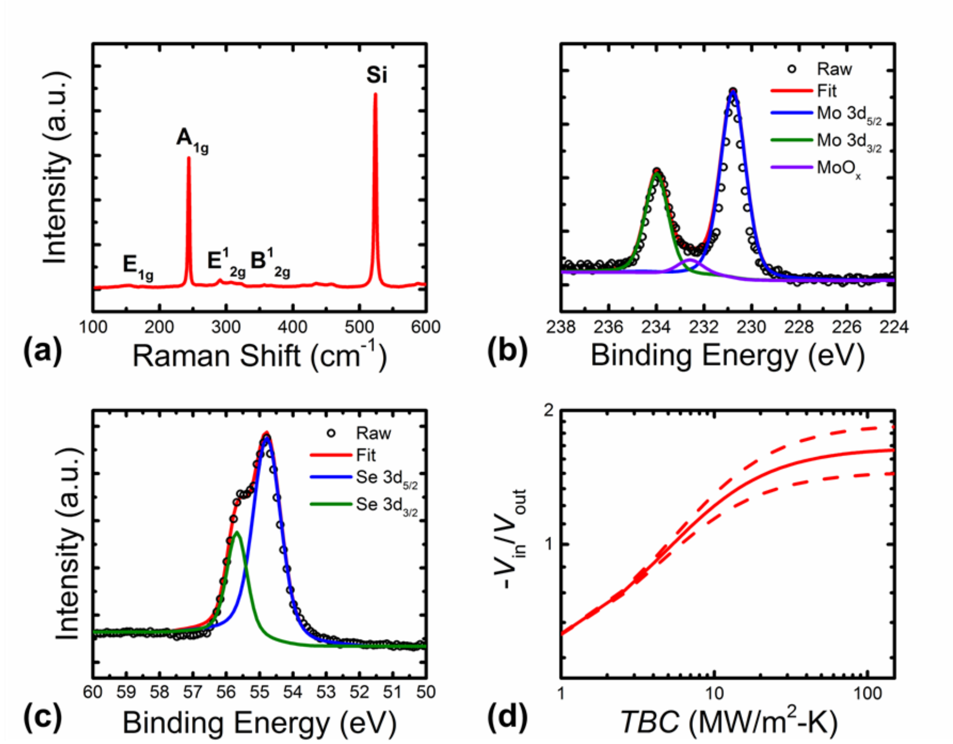

Figure 6-2 (a) Single-layer $MoSe_2$ Raman spectrum with two peaks corresponding to A_{1g} (out-of plane) and E^1_{2g} (in-plane) modes at ~244 and ~291 cm^{-1}, respectively. (b) High resolution Mo 3d XPS spectrum with Mo $3d_{5/2}$ and Mo $3d_{3/2}$ doublet with peak binding energies of 230 and 233 eV, respectively, with slight MoO_x peak. (c) High resolution Se 3d XPS spectrum with Se $3d_{5/2}$ and Se $3d_{3/2}$ doublet with peak binding energies of 54.8 and 55.7 eV, respectively. (d) Correlation curve used to calculate TBC from the $-V_{\mathrm{in}}/V_{\mathrm{out}}$ created by varying the M-$MoSe_2$-SiO_2 TBC from 1 to 150 MW/m^2-K at a delay time of 100 ps. The solid line is used to create TBC maps and corresponds to SiO_2 thermal conductivity, *k*, of 1.38 W/m-K from TDTR measurements. The dashed lines are calculated using the upper and lower bounds from MC simulations.

6.2 TDTR Results

6.2.1 2D Mapping of TBC

In traditional TDTR experiments, the arrival time of the probe is delayed relative to the pump beam (in contrast, the pump beam can be advanced relative to the probe [326]) to map the decay of the thermoreflectance signal. This typically requires several minutes per measurement, but the time to scan a 2D area can be decreased substantially by measuring the thermoreflectance signal, $-V_{\mathrm{in}}/V_{\mathrm{out}}$, at a single delay time where V_{in} and V_{out} are the in-phase and out-of-phase signal, respectively, of the lock-in amplifier. This approach was initially used to map the thermal conductivity of Nb-Ti-Cr-Si diffusion couples [355] and extended recently to show thermal conductivity suppression near grain boundaries in polycrystalline diamond [436]. The method is analogous to a technique used by Yang et al. [222] to map TBC at M-G interfaces. The 2D map of TBC is created by raster scanning the sample over a 120x120 μm^2 area. Precise control of the sample position is achieved using a motorized translation stage and DC servo motor controller (Thorlabs MTS25-Z8 and KDC101, respectively). The pump and probe $1/e^2$ radii were ~5 and ~3 µm (measured using a DataRay Inc. Beam'R2 beam profiler), respectively, with pump and probe powers of 7 and 3 mW, respectively. The resolution of the resulting 2D image is determined by the step size of sample translation (3 µm in this study). The TBC is calculated by comparing the measured $-V_{\mathrm{in}}/V_{\mathrm{out}}$ value to a correlation curve which predicts $-V_{\mathrm{in}}/V_{\mathrm{out}}$ as a function of TBC at metal-$MoSe_2$-SiO_2.

Prior to 2D TDTR mapping, correlation curves were created from theoretically calculated values of $-V_{\mathrm{in}}/V_{\mathrm{out}}$ as a function of TBC at M-$MoSe_2$-SiO_2 interface. To accomplish this, we must first know the geometry and thermal properties of each layer of our sample (Figure 6-1(c) and (d)). As stated earlier, metal transducer thickness (d) was measured using atomic force microscopy and confirmed using picosecond acoustics [341]. Thermal conductivity (k) of metal films were measured using the Wiedemann-Franz law, $L_0 = k/\sigma T$, where k is thermal conductivity, σ is electrical conductivity, T is absolute temperature, and L_0 is the Lorenz number (taken from literature as 2.44×10^{-8} $\mathrm{W\Omega K^{-2}}$

[390]). Electrical conductivity measurements were performed at RT on reference glass slides using a four-point probe technique.

SiO_2 thickness was measured using reflectometry (Nanometrics Nanospec 3000 reflectometer). The TBC at SiO_2-Si interface was taken from literature [437] along with Si thermal conductivity [184]; however, the sensitivity to these two parameters were very small and did not significantly affect the measured TBC at metal-$MoSe_2$-SiO_2 interface. Bulk values for volumetric heat capacity were used for each layer. The SiO_2 thermal conductivity is the most important parameter which remains to be determined. The importance of the properties of the underlying layer immediately adjacent to the interface of interest [349] was showed previously for M-G-SiO_2 interfaces, which also applies here for M-$MoSe_2$-SiO_2 interfaces. The sensitivity of the model to SiO_2 thermal conductivity makes its measurement critical to accurately determining TBC. Performing full TDTR scans (from 100 – 6000 ps) on the larger (500 µm) windows, the SiO_2 thermal conductivity was determined to be 1.38 (+0.68/-0.46) W/m-K in agreement with bulk [438]. The upper and lower bounds were calculated using MC simulations [347, 349].

With all properties of the sample now known, a correlation curve (Figure 6-2(d)) was created by calculating $-V_{\mathrm{in}}/V_{\mathrm{out}}$ while varying the M-$MoSe_2$-SiO_2 TBC from 1 to 150 MW/m^2-K at a delay time of 100 ps. We chose 100 ps because the sensitivity to TBC is higher at short delay times. The solid line in Figure 6-2(d) is used to create TBC maps and corresponds to SiO_2 thermal conductivity, k, of 1.38 W/m-K from TDTR measurements. The dashed lines represent the upper and lower limits from MC simulations. For each curve, $-V_{\mathrm{in}}/V_{\mathrm{out}}$ increases with TBC then plateaus which can be explained by the decreased sensitivity compared to SiO_2 thermal conductivity as TBC increases [349].

Spatial mapping of TBC was performed by raster scanning of the sample over a 120x120 μm^2 area using 3 µm increments (i.e., the $1/e^2$ radius of the probe beam), much larger than the 100 µm square area of metal coated $MoSe_2$ islands.

By analyzing the thermoreflectance signal (i.e., $-V_{\mathrm{in}}/V_{\mathrm{out}}$) we can easily distinguish between areas with and without metal present. Figure 6-3(a) (Al) and (b) (Ti) show optical images (100x) of individual $MoSe_2$ islands which were probed during this study. From the figure, we see the growth process produced mostly single-layer islands and some bilayer regions where smaller islands have grown above larger regions. A map of $-V_{\mathrm{in}}/V_{\mathrm{out}}$ signal across the 120x120 μm^2 area in Figure 6-3(c) and (d) show the alignment is quite good in comparison with the optical images. The recorded $-V_{\mathrm{in}}/V_{\mathrm{out}}$ signal in areas where no metal transducer coated the sample resulted in negative numbers which, when used as input to the correlation curve, produced negative TBC. These values were ultimately set to zero. Also excluded were TBC values less than ~5 MW/m^2-K as they are only observed near the edge of the metal covered regions of the sample.

Analyzing the TBC maps of Figure 6-3(e) and (f), some single-layer $MoSe_2$ regions can be distinguished from bilayer regions. Higher TBC values were located on areas not covered by $MoSe_2$ (Al-SiO_2 or Ti-SiO_2 interfaces). In addition, the color contours across the $MoSe_2$ islands show TBC is higher for the Ti sample compared with Al. Edge effects were observed, as evidenced by differences in the color contours in the center and near the edge of $MoSe_2$ islands in Figure 6-3(c)-(f), which could be due to different M-$MoSe_2$ interaction at the a-axis of $MoSe_2$ or near the edge of metal coated area of the sample. The variation in TBC across the probed area could result from change in the interface structure

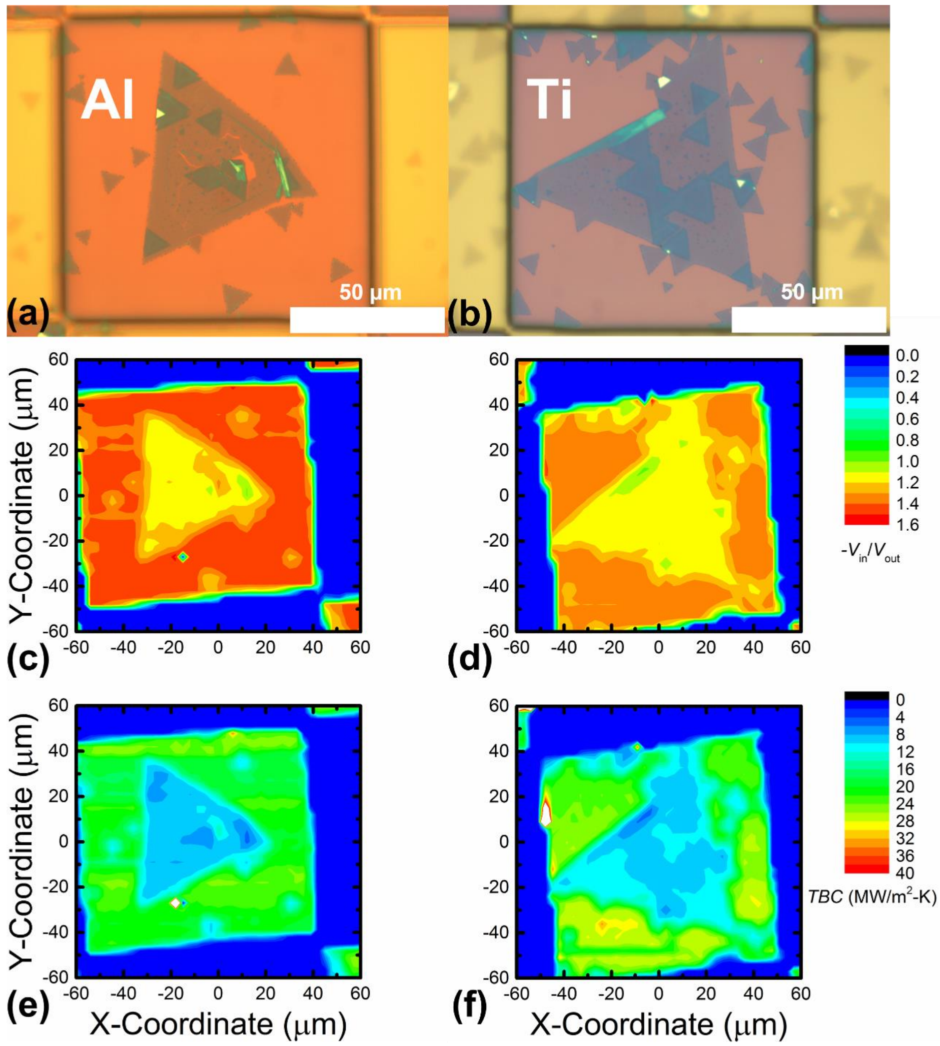

Figure 6-3 Optical microscope images (100x) showing probed area of 2D TDTR mapping experiments at (a) Al-$MoSe_2$-SiO_2 and (b) Ti-$MoSe_2$-SiO_2 interfaces. (c), (d) Spatial variation of $-V_{in}/V_{out}$ signal showing good alignment with to optical images. 2D TBC map across probed 120x120 μm^2 area of (e) Al and (f) Ti covered regions of sample. Some single-layer $MoSe_2$ regions can be distinguished from bilayer regions in both images. The color contours suggest higher TBC across Ti-$MoSe_2$-SiO_2 interfaces compared to Al-$MoSe_2$-SiO_2. Also, higher TBC values were located on areas not covered by $MoSe_2$ (Al-SiO_2 or Ti-SiO_2 interfaces). Edge effects are apparent from differences in color contours at the center and near the edges of $MoSe_2$ islands in (c)-(f).

near bilayer $MoSe_2$ regions. TBC depends on chemical (i.e., bonding) [439] and mechanical (i.e., roughness) [370] properties of the interface. A systematic study correlating interfacial bonding [226] and/or surface roughness [209] to TBC using XPS or

AFM, respectively, could provide more insight to the nature of thermal interaction at electrical contacts in TMD devices.

As previously mentioned, the growth process for the $MoSe_2$ samples result in single-layer and bilayer regions. While performing the TBC mapping, single-layer and bilayer regions are probed together without distinguishing between the two during the measurement. The results suggest there is a sharp distinction between regions with different layer number, but finding a sharp boundary is arduous due to low resolution of TBC maps and difficulty in alignment with corresponding optical image. The distribution of TBC in single-layer and bilayer regions is compared using the contrast of the optical images in Figure 6-3(a) and (b). Single-layer regions appear lighter than bilayer regions, allowing the pixels of the optical images to be clustered by applying k-means algorithm [440] (help from Wenqing Shen is much appreciated). The k-means algorithm partitions all pixels into k clusters with each cluster having a mean value, and pixels in one cluster are closest to the corresponding mean value among all cluster means. Regions with no $MoSe_2$ (i.e., 0-layer) can also be identified.

The TBC maps (Figure 6-3(e) and (f)) are clustered based on the TBC value, enabling a sharp boundary to be established between different regions. Key points, mostly corners, of the optical images and TBC maps are selected, and the locations of these key points are used to calculate the perspective transformation matrix between the optical images and TBC maps which were used to align optical images and TBC maps. The original TBC maps have much lower resolution than the optical images thus they are resized/scaled for alignment and better clustering results. The clustered optical images are shown in Figure 6-4(a) and (b) and the different colors correspond to single-layer (blue),

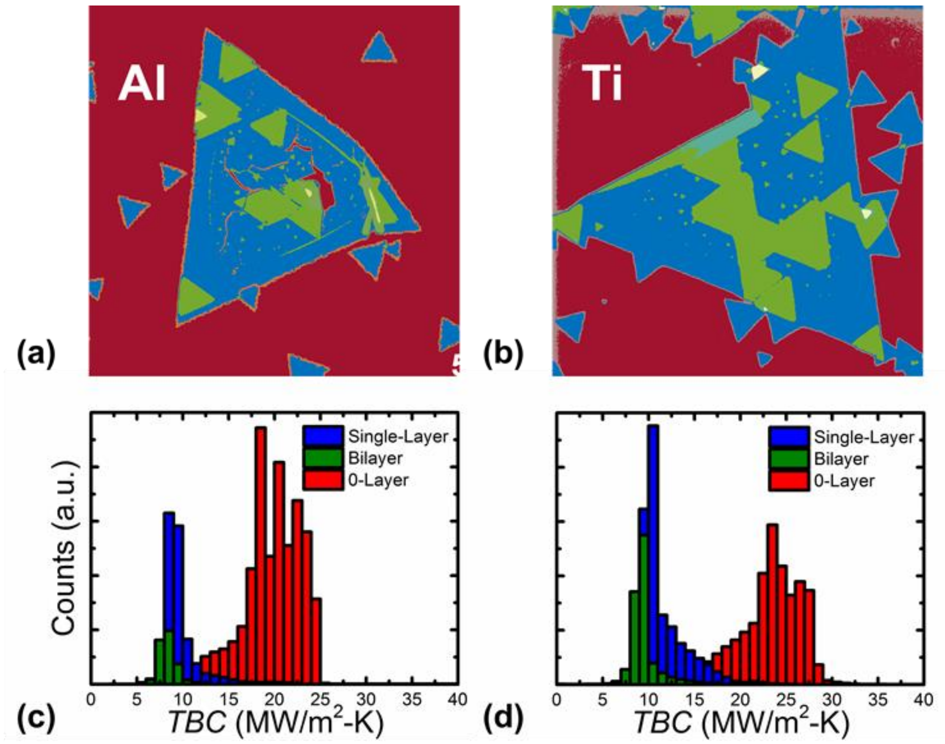

Figure 6-4 Clustered optical images for (a) Al and (b) Ti samples with single-layer (blue), bilayer (green), and 0-layer (red) regions highlighted. Histograms showing the distribution of TBC values across (c) Al and (d) Ti samples confirm TBC in single-layer regions is higher than bilayer regions.

bilayer (green) and 0-layer (red) regions of the sample. Following alignment, the corresponding TBC values for each cluster in the optical images were extracted from the aligned TBC maps. The histogram plots for each cluster are shown in Figure 6-4(c) and (d) for Al and Ti samples, respectively. The results reveal the TBC in single-layer regions are in fact higher than bilayer regions.

6.2.2 Full Delay Time TDTR

Because the sensitivity of model parameters varies over a range of delay times, we perform full TDTR scans (100 – 6000 ps) at different positions across the areas shown in Figure 6-3(a) and (b) to obtain a more accurate estimation of TBC. The results of full TDTR scans shown in Figure 6-5 were, for the most part, in agreement with the TBC maps where two, clearly-defined regions were observed corresponding to M-$MoSe_2$-SiO_2 and M-SiO_2 interfaces. In Figure 6-5 we see that TBC at Ti-$MoSe_2$-SiO_2 interface was consistently higher than Al-$MoSe_2$-SiO_2 interface in agreement with the contour plots in Figure 6-3(e) and (f). On average, TBC increases of 4 and 24 MW/m^2-K were observed at Ti-$MoSe_2$-SiO_2 and Ti-SiO_2 interfaces compared to Al-$MoSe_2$-SiO_2 and Al-SiO_2 interfaces, respectively, showing the choice of metal can significantly impact the TBC and thus heat dissipation from electrical contacts in TMD devices. The error bars in Figure 6-5 were calculated using MC simulations [347, 349]. It must be pointed out that the TBC from full TDTR scans differs from the 2D TBC maps. However, the general trend of increased TBC

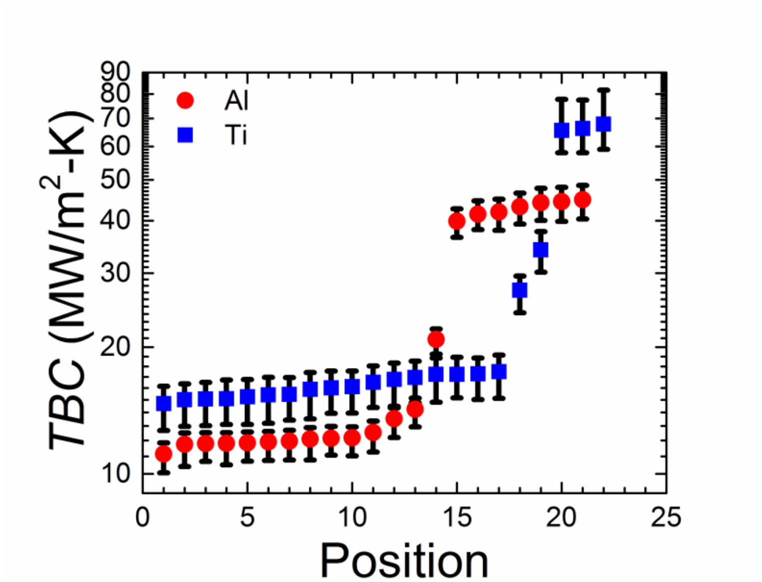

Figure 6-5 Summary of TBC values from full TDTR scans at several positions across $MoSe_2$ islands from 2D mapping experiments. Error bars were calculated using MC simulations. We observed two, clearly-defined regions corresponding to M-$MoSe_2$-SiO_2 and M-SiO_2 interfaces. Also, TBC at Ti-$MoSe_2$-SiO_2 interface was consistently higher than Al-$MoSe_2$-SiO_2 interface. TBC increases of 4 and 24 MW/m^2-K, on average, at Ti-$MoSe_2$-SiO_2 and Ti-SiO_2 interfaces, respectively, compared to Al-$MoSe_2$-SiO_2 and Al-SiO_2 interfaces show the impact of metal contact on TBC.

at Ti-$MoSe_2$ and Ti-SiO_2 interfaces can still be observed, thus the TBC mapping results are useful for comparative purposes.

In addition, the TBC at Al-SiO_2 and Ti-SiO_2 interfaces is less than previously reported values (85 – 120 MW/m^2-K) for M-SiO_2 interfaces [208, 288, 349] which is attributed to residual photoresist or other residue from the CVD growth process**.** This difference in TBC for Al and Ti interfaces with $MoSe_2$ could be caused by strong interaction between Ti *3d* and Se *4p* orbitals [255]. On the other hand, the difference in Debye temperatures of Al and Ti metals (Ti =420 K, Al=428 K [179]) and oxides (TiO_2=750 K [403], Al_2O_3=1100 K [441]) formed during high vacuum deposition could give rise to the observed differences in TBC. From this perspective, we would expect the Ti-$MoSe_2$-SiO_2 TBC to be higher since the Debye temperature of $MoSe_2$ (200 K [442]) is much closer to TiO_2. TBC may also be increased for both Al and Ti deposited in ultra-high vacuum environment, as shown previously for Ti-G-SiO_2 [225] and Ti-Al_2O_3 and Ti-MgO interfaces [229] either due to lower Debye temperature or increased reactivity of metal films with less oxidation.

Finally, the TBC results presented here are compared to values reported in literature for MoS_2 and $MoSe_2$ interfaces. Both are TMDs with similar semiconducting properties and structure; however, MoS_2 has been more widely studied until recently thus we use MoS_2 results for comparative purposes. The TBC at MoS_2 and $MoSe_2$ interfaces are not expected to be same as they are two different materials and the surface structure depends on the sample fabrication method, but the comparison aims to highlight the similarities and differences from other studies. The values presented here are slightly less than the previously reported values (20 – 26 MW/m^2-K) at M-MoS_2 [258] interface. Previous studies used exfoliated MoS_2 and $MoSe_2$ flakes which can have different interfacial properties compared to CVD grown. More recent studies of MoS_2-SiO_2 interfaces [261, 263], reported small differences between exfoliated and CVD-grown MoS_2 with and without an AlO_x capping layer which forms interface structure (AlO_x-MoS_2-SiO_2) similar to the M-$MoSe_2$-SiO_2 interfaces used here. It is important to note that in the present study the M-$MoSe_2$-SiO_2 interfaces were treated as a single, diffuse interface. The results of Yasaei et al. [262] for Au-Ti-MoS_2-SiO_2 interfaces are more relevant to the current study. Reported TBC values were 20 and 33 MW/m^2-K for exfoliated and CVD grown MoS_2, respectively, in similar range of the values presented here.

6.3 Conclusions

In summary, the spatial variation of the TBC at interfaces of CVD grown $MoSe_2$ with metal was investigated using a modified TDTR technique. The thermoreflectance signal at a single probe delay time was compared with a correlation curve which describes the change in the signal with respect to the TBC at M-$MoSe_2$-SiO_2 interface. Using this technique, a 2D map of TBC was created in reduced time than would be required to do full TDTR scans over delay times of several ns. The results showed higher TBC at Ti-$MoSe_2$-SiO_2 interface compared to Al-$MoSe_2$-SiO_2. The analysis of clustered optical images revealed the TBC in single-layer regions was higher than bilayer regions of $MoSe_2$. Full TDTR scans also confirmed an increase in TBC at M-$MoSe_2$-SiO_2 and M-SiO_2 for Ti compared to Al highlighting the importance of choice of metal contact. This study will provide much needed insights into the energy efficient design and thermal management of future TMD devices.

CHAPTER 7. THERMAL CONDUCTIVITY AND HEAT CAPACITY OF THIN FILM HAFNIA

In this chapter, the thermal properties of thin film HfO_2 are examined. Thermal conductivity and heat capacity are determined for films of varying thickness. The modulation frequency of TDTR experiments determines the sensitivity to different thermal properties of a sample. From this, the thermal conductivity and heat capacity can be determined simultaneously. The total thermal conductance and effective thermal conductivity are estimated based on the layer thickness. Both include the contribution from the interfaces above and below the thin film layer. The thickness-independent, intrinsic thermal conductivity is determined for HfO_2 layers ranging from 12 – 215 nm using least-squares fitting and a relationship between the intrinsic thermal conductivity, the effective thermal conductivity, and the total thermal conductance of the interfaces adjacent to the thin film layer.

7.1 Sample Fabrication and Characterization

The HfO_2 layers in this study were grown on Si substrates at 200 °C in a Cambridge Nanotech Fiji ALD system using Tetrakis(dimethylamido) hafnium and water precursors [443]. Thin Ti layers were first deposited on Si to improve adhesion of HfO_2 (these samples are obtained from industrial collaborators). In preparation for TDTR measurements, the HfO_2 films were coated with 100 nm Au (2 nm Ti adhesion layer) using electron-beam evaporation. The thicknesses of the Au transducer above HfO_2 film was determined using profilometry measurements on a co-deposited glass slide. The thermal conductivity was estimated from electrical conductivity measurements and the Wiedemann-Franz law: $L = k/\sigma T$, where σ is the electrical conducitivity, T is the absolute temperature, and L is the Lorentz number, 2.44×10^{-8} $W\Omega K^{-2}$ [390]. The resulting thermal conductivity for the Au film (190 W/m-K) was used as an input to the thermal model. The bulk value of the thermal conductivity was assumed for the Si substrate [184]. Bulk values for heat capacity were used for the Au film and Si substrate.

Figure 7-1(a) and (b) show scanning electron microscope images of the 12 nm and 106 nm sample, respectively. The structure of HfO_2 layers varied for samples with different thicknesses. Disordered, amorphous phases were located near the HfO_2-Si interface, while regions of crystalline, monoclinic phase appear as the sample thickness increased. The cross-sectional TEM image in Figure 7-1(c) show the disordered structure of the 12 nm HfO_2 layer suggesting the 12 nm sample is entirely amorphous. A similar image of the 106 nm sample in Figure 7-1(d) show an amorphous region near the HfO_2-Si interface, but crystalline regions can be observed while approaching the Au-HfO_2 interface. Figure 7-1(e) and (f) show high magnification TEM images of the highlighted regions of Figure 7-1(d) and confirms our observation of two distinct regions in 106 nm samples. The stoichiometry of the 12 nm and 106 nm HfO_2 layers were determined using electron energy loss spectroscopy (Figure 7-2(a) and (b)). The results show the 12 nm sample contained small oxygen deficiency, while the stoichiometry of the 106 nm sample was that of HfO_2. The local structure of HfO_2 was further analyzed by implementing fast Fourier transform (FFT) of the TEM image. Figure 7-2(c) and (d) show 12 nm layer and ordered crystalline structure in 106 nm layer, respectively. The FFT results confirm the highlighted crystalline region consists of monoclinic HfO_2.

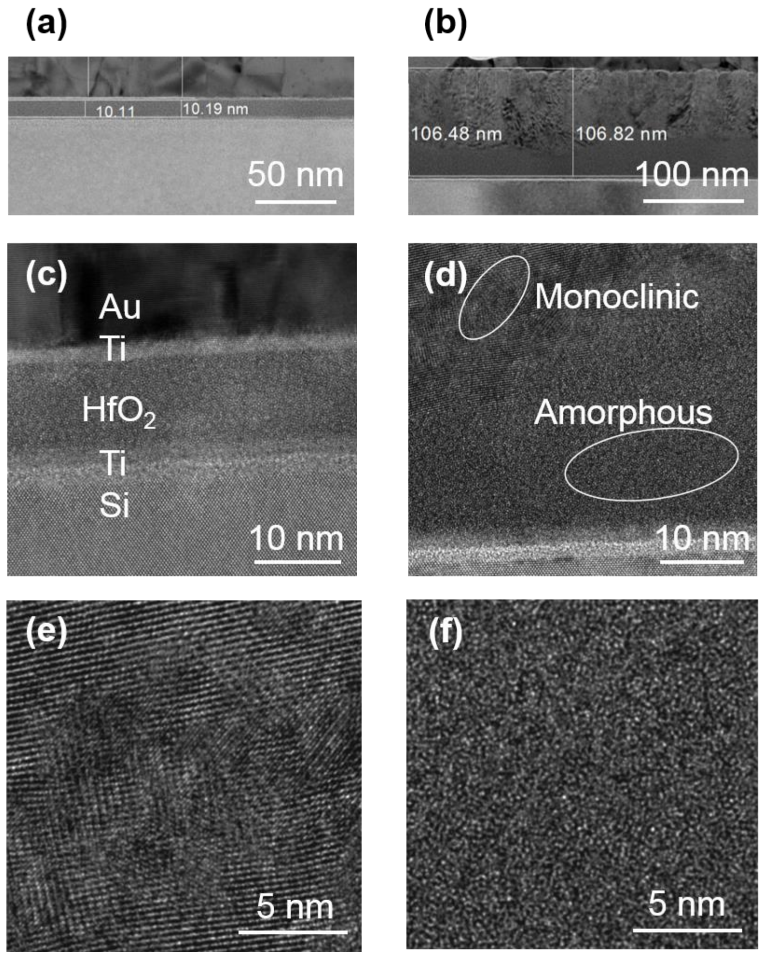

Figure 7-1 Scanning electron microscope images showing thickness of (a) 12 nm and (b) 106 nm HfO_2 layers. (c) Cross-sectional TEM images showing overall structure of the HfO_2 layer in 12 nm (d) and 106 nm samples. Si substrate is also shown. (e) Monoclinic and (f) amorphous regions of 106 nm HfO_2 layer highlighted in (d).

7.2 TDTR Methodology for Thin Film Analysis

Liu et al. [288] analyzed the thermal model used in TDTR and FDTR method and established criteria in which cross-plane and/or in-plane heat transfer effects must be considered. In the process, they found that cross-plane transport dominates in most of the thin film measurements. In addition, low and high frequency regimes where the thin film layer can be treated as an interface or as semi-infinite, resulting from a comparison of the

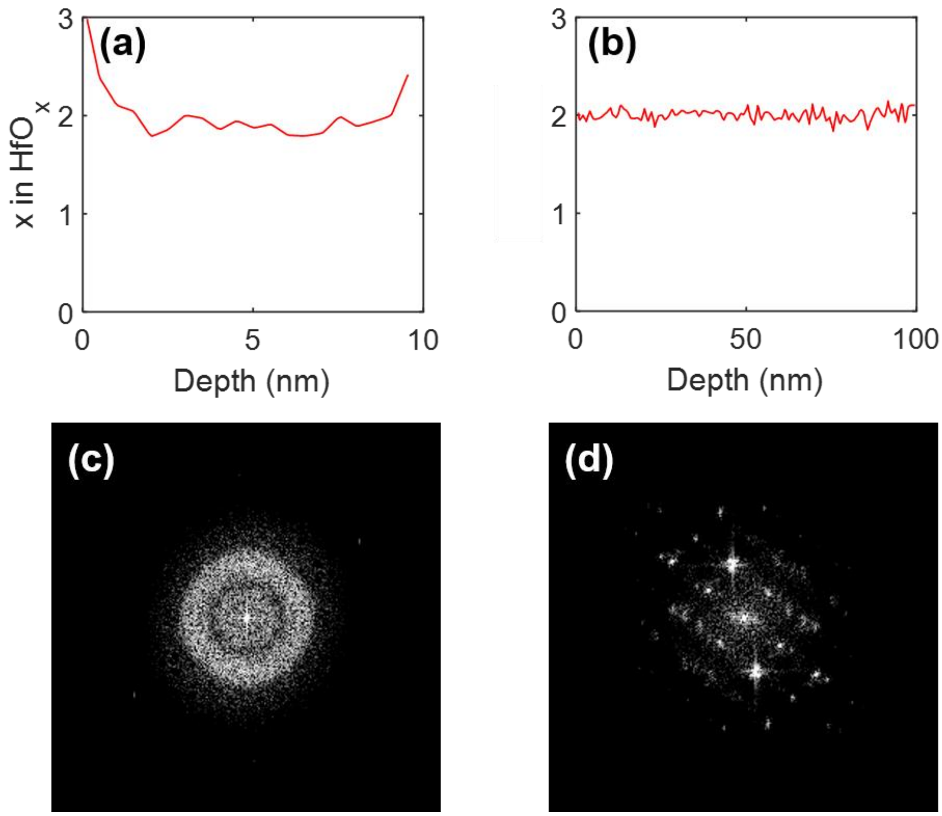

Figure 7-2 Electron energy loss spectroscopy results of (a) 12 nm and (b) 106 nm HfO_2 sample. FFT of TEM image for (c) amorphous 12 nm sample and (d) crystalline region in 106 nm layer.

penetration depth to the layer thickness [437], were given by the relationships $f_{\text{low}} < 0.055k/\pi d^2 C$ and $f_{\text{high}} > 4.5k/\pi d^2 C$ [288] where d is the thickness of the thin film layer.

In the low frequency regime, the thermal response is determined by the thermal conductance, $G = \frac{k}{d}$, and the heat capacity, C, and a thin film layer can be treated as an interface. The contributions from the interfaces on each side of the layer cannot be resolved individually; only the total thermal conductance, G_{T}, can be determined. In the high frequency regime, the thermal response is determined by the thermal effusivity ($\sqrt{kC}$), which measures a materials ability to exchange thermal energy with its surroundings, and the thin film layer can be treated as semi-infinite. In the intermediate regime the thermal effusivity as well as the thermal diffusivity ($D = \frac{k}{C}$) are both important. In these two regimes the thermal conductivity and the heat capacity can be determined by creating a k-C diagram from different combinations of the two properties at different modulation frequencies [288, 290]. The different curves intersect at the thermal conductivity and heat capacity of the sample.

Table 7-1 lists the high and low frequency cutoffs for each sample in this study using k of bulk HfO_2 for (1.1 W/m-K) [183] and C values determined here. The modulation frequencies used in this study were 1.2, 3.6, 6.3, and 8.8 MHz, corresponding to l values from 110 to 340 nm. To increase sensitivity to the properties of the HfO_2 layers, the k-C diagrams were created using modulation frequencies of 6.3, and 8.8 MHz for the 215, 106, and 53 nm samples ($l \approx$ 110-140 nm). The 12 nm sample was treated as an interface for all frequencies and total thermal conductance (G_{T}) was measured. The pump and probe $1/e^2$ radii were ~19 and ~8 µm, respectively, with pump and probe powers of 25-40 and 7-8 mW, respectively. The arrival time of the probe was delayed up to 7 ns relative to the pump.

Table 7-1 Low and high frequency regimes for interface and semi-infinite approximation, respectively, satisfying the relationships $f_{\mathrm{low}} < 0.055k/\pi d^2 C$ and $f_{\mathrm{high}} > 4.5k/\pi d^2 C$ [274]. The heat capacity values for each sample are taken from $k - C$ diagrams. The 12 nm HfO_2 layer was treated as interface because the modulation frequencies in this study were below the low frequency cutoff [288, 437].

d_{HfO2} (nm)	C (J/cm³-K)	f_{low} (MHz)	f_{high} (MHz)
12	2.8	43.4	3550
53	2.8	2.23	182
106	2.7	0.577	47.2
215	2.2	0.172	14.1

7.3 TDTR Results for Thin Film Samples

7.3.1 $k-C$ Diagrams

The transducer-thin film (e.g., Au-HfO_2) TBC was used as a fitting variable in addition to thin film thermal conductivity. The sensitivity to the TBC at the Au-HfO_2 and HfO_2-Si interfaces, i.e., $TBC_{\mathrm{Au-HfO2}}$ and $TBC_{\mathrm{HfO2-Si}}$, respectively, was extremely low due to the low thermal conductivity of the HfO_2 layers. Both interfaces include a 2 nm Ti adhesion layer, and the TBC at Ti-Si interface has been reported to be 150 – 200 MW/m^2-K [432, 444]. As a result, $TBC_{\mathrm{HfO2-Si}}$ was held constant at 150 MW/m^2-K while fitting for $TBC_{\mathrm{Au-HfO2}}$ and k_{HfO2} for the 53, 106, and 215 nm samples. The results of the k-C diagrams for the 53, 106, and 215 nm HfO_2 samples are analyzed next.

A $k-C$ curve was created for modulation frequencies of 6.3 and 8.8 MHz which intersects at the thermal conductivity and heat capacity of the HfO_2 layer. Figure 7-3(a) shows the k-C diagram for the 215 nm layer. The intersecting points of the graph are near the bulk thermal conductivity of 1.1 W/m-K, but the heat capacity of 2.2 J/cm^3-K is nearly 20% less than the heat capacity of thinner samples. The k-C diagram for the 106 nm HfO_2 sample in Figure 7-3(b) intersects at k and C values of 1.09 W/m-K and 2.7 J/cm^3-K, respectively. In Figure 7-3(c), the k-C diagram for the 53 nm thick HfO_2 layer has an intersecting point at 1.03 W/m-K and 2.77 J/cm^3-K.

The variation in the heat capacity measurement of the 215 nm sample could be caused by thermal waves probing both amorphous and crystalline regions of the HfO_2 layer. The crystalline (stable monoclinic or metastable orthorhombic) HfO_2 is expected to be more dense than amorphous HfO_2. Kuo et al. [445] observed crystallization, increased refractive index, and decreased etch rate (10% hydrofluoric acid) of sputtered HfO_2 films following high temperature anneal. The authors attributed this to film densification.

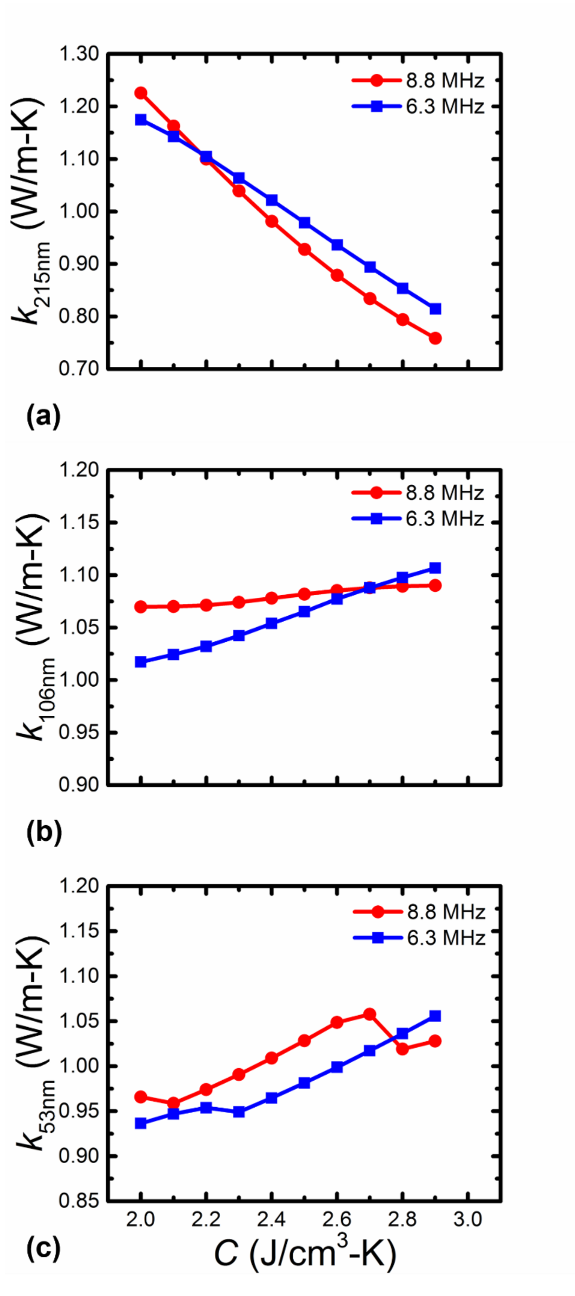

Figure 7-3 k-C diagrams for (a) 215, (b) 106, (c) 53 nm thick HfO_2 layers where the curves for each frequency intersect at the thermal conductivity and heat capacity of the sample. In (a), the intersection points vary from k = 1.1 W/m-K and C = 2.2 J/cm^3-K, a 20% decrease in heat capacity compared to thinner films. In (b), the intersection points occur at k = 1.09 W/m-K and C = 2.7 J/cm^3-K. The curves in (c) intersect at k = 1.03 W/m-K and C = 2.77 J/cm^3-K.

However, this is insufficient to explain the variation in heat capacity since the 215 nm HfO_2 should be more crystalline but lower heat capacity was observed. On the other hand, Lee et al. [272] observed 10% reduction in density compared to bulk in polycrystalline HfO_2 films which, if also true for the samples in this study, could explain the reduction in heat capacity. It is also possible that increased carbon impurities in thicker HfO_2 films could lead to decreased density as shown previously for HfO_2 films deposited by metal-organic chemical vapor deposition [446]. An additional explanation, related with the sample structure, is that amorphous HfO_2 has higher heat capacity than monoclinic HfO_2 [447]; therefore, the effective heat capacity would decrease when the sample includes a larger portion of monoclinic HfO_2.

7.3.2 Intrinsic Thermal Conductivity

After estimating heat capacity for each sample, the HfO_2 thermal conductivity and TBC at Au-HfO_2 interface can be determined. The heat capacity from the $k - C$ diagrams in Figure 7-3 were treated as constants, and $TBC_{\mathrm{HfO2-Si}}$ was held constant and set to 150 MW/m^2-K [432]. TDTR scans were performed at varying points across the samples and typical experimental signals are compared in Figure 7-4. The results are plotted in Figure 7-5(a) where the error bars were calculated using MC simulations [347, 349]. The thermal conductivity agrees with the bulk value, while TBC varies from 60 – 100 MW/m^2-K. The error bounds for TBC at Au-HfO_2 interface in Figure 7-5(a) become larger as sample thickness increases. This is because the sensitivity to $TBC_{\mathrm{Au-HfO2}}$ decreases as the thermal resistance of the underlying HfO_2 increases.

The heat capacity of the 12 nm layer could not be determined because of its thin nature; however, the interface approximation [288, 437] was valid since all modulation frequencies used in this study were below the low frequency cutoff in Table 7-1. Treating the 12 nm HfO_2 layer as an interface between the metal transducer and Si substrate, the average thermal conductance, G_{T}, of the 12 nm HfO_2 layer across the four modulation frequencies was 39.3 (+3.9/-3.7) MW/m^2-K. This includes the contribution from $TBC_{\mathrm{Au-HfO2}}$ and $TBC_{\mathrm{HfO2-Si}}$ which cannot be resolved separately by TDTR at the modulation frequencies used here. The low thermal conductance is due to the low thermal conductivity and amorphous nature of the film [448]. For comparison, G_{T} of the 53, 106, and 215 nm HfO_2 samples were calculated using the results in Figure 7-5(a) assuming $TBC_{\mathrm{Au-HfO2}}$, $G_{\mathrm{T,HfO2}}$, and $TBC_{\mathrm{HfO2-Si}}$ are three resistances in series [402]. The results are shown in Figure 7-5(b) along with the result for the 12 nm sample. As expected, G_{T} decreases with increasing HfO_2 thickness.

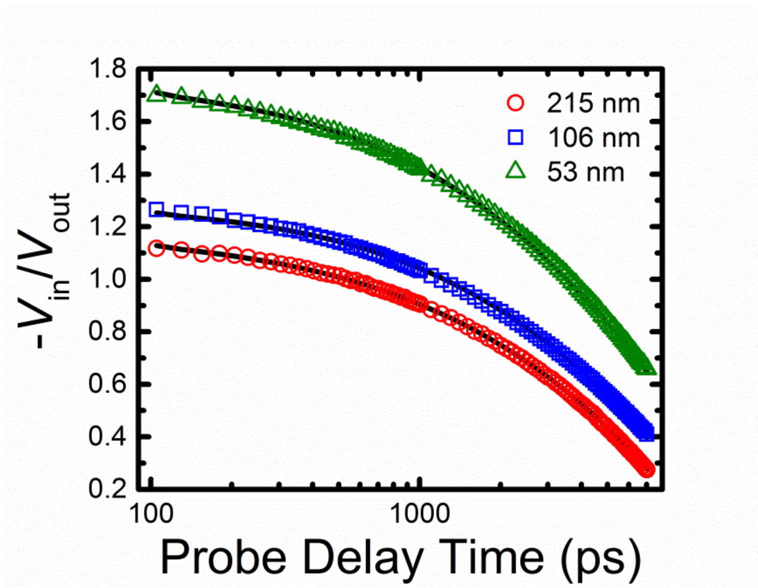

Figure 7-4 Comparison of TDTR signals (8.8 MHz) near the intersecting points of the k-C diagrams. The k (C) values for the 215, 106, and 53 nm samples were 1.1 (2.2), 1.09 (2.7), and 1.03 (2.8) W/m-K (J/cm^3-K), respectively.

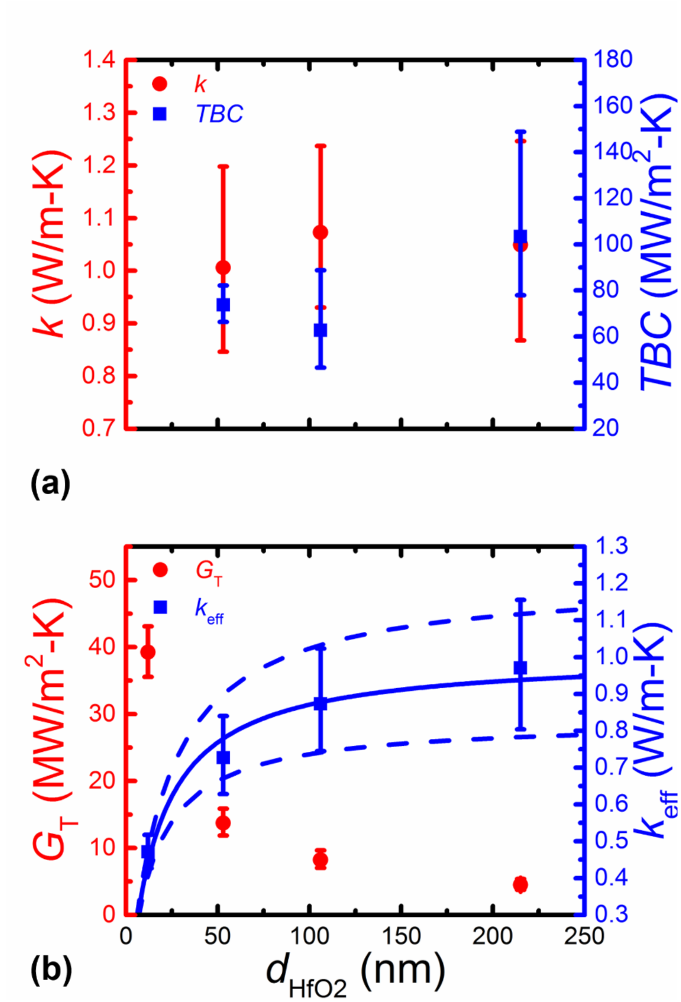

Figure 7-5 (a) Thermal conductivity and TBC at Au-HfO$_2$ interface of 53, 106, and 215 nm HfO$_2$ films. The heat capacity from the $k - C$ diagrams in Figure 7-3 were treated as constants, and $TBC_{\mathrm{HfO2-Si}}$ was held constant and set to 150 MW/m^2-K. The thermal conductivities were comparable to the bulk value. The error bars were determined from MC simulations. (b) Comparison of G_{T} and k_{eff} values of 12, 53, 106, and 215 nm thick HfO$_2$ samples. From Equation 1 (solid line), the thickness-independent k_{i} for HfO$_2$ was estimated to be 1.00 W/m-K, in agreement with a previous study [275]. The dashed lines represent the upper and lower bounds of k_{eff} from the results of MC simulations.

Finally, the intrinsic thermal conductivity of HfO$_2$ films of varying thickness is determined. The product of G_{T} and the layer thickness was first used to calculate and effective thermal conductivity, including the contribution from $TBC_{\mathrm{Au-HfO2}}$ and

$TBC_{\mathrm{HfO2-Si}}$, for each sample. The intrinsic thermal conductivity, k_{i}, of HfO_2 is related to the effective thermal conductivity through the relationship [274],

$$k_{\mathrm{eff}} = \frac{k_{\mathrm{i}}}{1+{k_{\mathrm{i}}}/{dG_{TBC}}}, \tag{26}$$

where G_{TBC} is the combined thermal conductance of the Au-HfO_2 and HfO_2-Si interfaces. Using nonlinear least-squares fitting, k_{i} and G_{TBC} values of 1.00 W/m-K and 65.4 MW/m^2-K, respectively, are calculated. The resulting curve is plotted as a solid line in Figure 7-5(b), while the upper and lower bounds are plotted as dashed lines. The intrinsic thermal conductivity agrees well with the $k - C$ diagrams as well as a similar study on thin film HfO_2 [275].

7.4 Conclusions

In conclusion, the thermal conductivity and heat capacity of thin film, HfO_2 samples were measured at RT using TDTR. The thermal conductivity of 53, 106, and 215 nm HfO_2 agreed with bulk values, but the volumetric heat capacity decreased for the 215 nm layer compared to the thinner films. The composition of the films was determined using TEM, and the change of heat capacity could be explained by decreased density of HfO_2 layer due to the combined amorphous and crystalline regions of HfO_2 layer. The effective thermal conductivity, including the contribution of adjacent interfaces above and below the HfO_2 layers, was used to calculate the thickness-independent, intrinsic thermal conductivity to be 1.00 W/m-K in agreement with bulk values

CHAPTER 8. SUMMARY AND OUTLOOK

8.1 Summary and Conclusions

In this dissertation, the thermal transport at the interfaces of 2D materials and within thin film HfO_2 were investigated using TDTR. The following is a summary of the results.

(1) TDTR was used to investigate the effect of chemisorption and physisorption on the TBC at M-G-M interfaces. Transition metals Ti and Ni form chemisorbed (strongly bonded) interfaces with graphene while Au forms physisorbed (weakly bonded) interface. No enhancement of TBC was observed for Ti and Ni, which was attributed to the presence of native oxide in the bottom layer of the metal-graphene-metal interface. XPS revealed native oxide layers of 2.8 and 2.5 nm thickness were present in Ti and Ni samples, respectively. The TBC was also significantly reduced at the Ti-Ti and Ni-Ni interfaces compared to the Au-Au interface in this study confirming the effect of oxidation on TBC. Au is a noble metal which does not oxidize in ambient conditions. The insertion of single-layer graphene into the Au-Au interface substantially reduced the electronic contribution to TBC which are the primary thermal carriers at M-M interfaces. These findings highlight a critical design consideration for the M-G-M interfaces in future device applications.

(2) The TBC at the interfaces of h-BN and graphene was measured at RT using TDTR. At the time this thesis is being written, a Raman spectroscopy technique requiring lithographically patterned metal lines to electrically heat the graphene layer has been the lone method for probing this interface. TDTR requires no special sample preparation only the deposition of a thin metal film. CVD grown h-BN and graphene were first transferred

to the surfaces of two oxidized Si samples, and TDTR was used to determine the TBC at M-h-BN-SiO_2 and M-G-SiO_2 interfaces. A h-BN-graphene interface was formed by mechanical stacking through successive transfers of graphene followed by h-BN. TDTR was then used to probe the M-h-BN-G-SiO_2 sample. The three measurements were combined with a series resistor network model to extract the TBC at the h-BN-G interface.

To complement the experimental results, the phonon transmission and TBC at h-BN-G interface were predicted using two forms of the DMM for anisotropic materials. The two models assume an anisotropic dispersion in h-BN and graphene, a more accurate depiction of the physical properties of the two materials. They differ only in the representation of the ZA phonon mode along the in-plane direction. One model applies a piecewise linear approximation with two different phonon velocities near the center and at the boundary of the first Brillouin zone, as opposed to a single velocity, which is the assumption of the first model. The phonon transmission predicted using the piecewise approximation was in better agreement with experimental fit, and therefore a more accurate representation of the physical properties of the materials. Both models displayed similar temperature dependent behavior, which is to suggest the in-plane ZA mode and out-of-plane LA mode along the out-of-plane direction are the dominant contributors to the phonon transmission and TBC at the h-BN-graphene interface.

(3) A direct-write photolithography technique was used to isolate CVD grown $MoSe_2$ islands for TDTR measurements. Following deposition of Al and Ti, a modified TDTR technique, requiring much less time than traditional TDTR scans, was used to create 2D maps showing the spatial variation of TBC across M-$MoSe_2$-SiO_2 interfaces. Traditionally, in TDTR the decay of the thermoreflectance signal is determined as a

function of time. To reduce the time to map a 2D area, a correlation curve was created showing the variation in thermoreflectance signal with TBC at a single time. The thermoreflectance signal was then measured experimentally and compared with the correlation curve to determine the TBC value. 2D TBC maps were created at Al-$MoSe_2$-SiO_2 and Ti-$MoSe_2$-SiO_2 interfaces. The analysis of the TBC maps revealed higher TBC in single-layer regions of $MoSe_2$ compared to bilayer. The TBC maps were also combined with traditional TDTR scans to confirm increased TBC at Ti-$MoSe_2$-SiO_2 interface compared to Al-$MoSe_2$-SiO_2. The results emphasize the impact selection of metal contacts can have on the thermal dissipation from electrical contacts in future $MoSe_2$ devices.

(4) The thermal conductivity and heat capacity of HfO_2 thin films of varying thickness were measured using TDTR. The thermal conductivity of 53, 106, and 215 nm films were near the bulk value. A 20% reduction in heat capacity was observed for the 215 nm film compared with thinner films. The composition of the HfO_2 films was investigated using transmission electron microscopy. A 12 nm film was fully amorphous, but a combination of amorphous and crystalline regions was observed in the thicker HfO_2 thickness. The decrease in heat capacity of the 215 nm films was, thus, attributed to decreased film density. The thickness of the 12 nm sample prevented performance of similar measurements of thermal conductivity and heat capacity. Instead, by treating the film as an interface, the total thermal conductance was measured with the contribution of the interfaces on the top and bottom of the thin film included in the measurement. In a similar way, the total thermal conductance of the remaining thin films was determined, and an effective thermal conductivity was determined for each sample by taking the product of the total thermal conductance and film thickness. The thickness-independent thermal

conductivity of HfO_2 films from 12 to 215 nm was estimated by fitting the effective thermal conductivity and combined TBC at both interfaces to an empirical model. The resulting thermal conductivity was in agreement with bulk.

8.2 Outlook for Future Work

Extensions to the topics covered in this dissertation are discussed next.

8.2.1 High Quality Metal-2D Material Interfaces

The oxidation of most metals upon exposure to ambient is unavoidable. To form high quality M-G or M-TMD interfaces for future studies, great care should be taken during and after metal deposition to ensure a high-quality interface is formed. In high vacuum (~10^{-6} Torr), oxygen species can react with metals during deposition. For example, in the case of Ti, high vacuum deposition results in TiO_x prior to exposure to ambient [449]. Metal capping layers which do not oxidize (e.g., Au) are often utilized to prevent surface oxidation of Ti. This will be for naught if TiO_x is deposited and not pure Ti metal because the oxidation will be prevalent throughout the thickness of the film. Wherever possible, the metal depositions should be performed in ultrahigh vacuum (~10^{-9} Torr) to prevent deposition of TiO_x species. Before exposure to ambient a capping layer such as Au will successfully prevent further oxidation in Ti layer forming high quality M-G and M-TMD interface [225, 450-452] for experimental study. The impact of high quality M-G contacts on future graphene devices is efficient thermal management including reduction in operating temperature leading to improved reliability and longevity.

A second option is to perform metal deposition inside a glovebox under N_2 or Ar_2 rich environment. This will also prevent oxidation of metal during deposition. For CVD grown graphene, a wet transfer process [37, 380] is generally used whereby graphene is retrieved from the surface of deionized water, or some other aqueous solvent, and placed on the substrate. In the case of sandwiched M-G-M structure, the metal surface is exposed to water which may result in further oxidation. A dry process [36, 38] should be used instead to prevent the oxidation from additional exposure during wet transfer. For example, graphene transferred from deionized water to a polymer surface, followed by dry transfer to substrate. This should mitigate additional oxidation which may result from the transfer process. An additional advantage of this technique it that it can be combined with glove box metal deposition to form high quality M-G interfaces. Dry processing may be automated in the future to improve scalability of device fabrication.

8.2.2 Isolated Metal-2D Material Interfaces

A direct measurement of TBC at a M-G or M-TMD interface has not been performed. Though the in-plane properties of 2D materials have been measured in suspended geometry with Raman spectroscopy [8, 10, 267, 453], a direct measurement of the cross-plane interfacial properties in this geometry have eluded researchers thus far. TDTR requires the deposition of a thin metal film which serves as a transducer for temperature measurement, and the ultrathin layer thickness of 2D materials require a substrate for mechanical support. Potential issues may arise if suspended 2D layer cannot support metal film. Thin metal films can be used, but for TDTR the metal must be optically thick so that all energy is absorbed in the metal transducer and only diffuses into underlying layer through heat conduction [317, 336]. Another issue may arise if high thermal conductivity metal such as Au is used. The thermal energy generated in the metal film following absorption of photons from the focused laser will diffuse along the in-plane direction in the metal. This will limit the sensitivity to the graphene or other 2D material layer. The assumption that the bottom layer in a multilayered TDTR sample is semi-infinite must also be satisfied. This can be done by assuming air underneath suspended materials is the semi-infinite bottom layer; however, the low thermal conductivity of air will limit sensitivity to TBC. This may not be feasible at this point, but I am optimistic that with the talent in the research community it will be accomplished at some point. Efforts have already been taken to probe the in-plane properties of layered bulk materials [264]. It is only a matter of time until this method reaches the single-layer limit.

8.2.3 Characterization of Variability in 2D Material Properties

The study of 2D materials will not be complete until high quality 2D layers can be produced across large areas. Exfoliation of high quality crystals from bulk [1] is promising at the fundamental research level, but device integration is unattainable using this method. Likewise, layers produced by CVD [36, 38, 381, 454-456] or epitaxial growth [6, 231, 457, 458] can be formed over large areas; however, the quality can be degraded compared to bulk with sample to sample variation as well as variation across a single sample. CVD growth is the most promising because of the possibility of large area coverage and flexibility in choice of supporting substrate. CVD-grown TMD layers with varying defect/doping concentration can result in different bandgap [459-461] and carrier type [430, 462, 463]. Tunable properties such as these are critical for the application of TMDs in optoelectronic devices designed for operation in a specific segment of the electromagenetic spectrum or CMOS devices with alternating n-type and p-type transistors. The thermal conductivity has been shown to vary as well [265, 266] which could greatly impact device performance but more work is needed. In addition, the effect of defect/doping concentration on the interfacial properties is not understood. One method of investigation could be in-situ XPS measurements [451] on TMD layers with different defect/doping concentration to show the interfacial reaction during metal deposition, followed by correlation with electrical and thermal experiments. The results from characterization of high quality, large area 2D layers with controlled defects/doping concentration will ultimately determine the fate of this class of materials.

REFERENCES

1. Novoselov, K.S., et al., *Two-dimensional atomic crystals.* Proceedings of the National Academy of Sciences of the United States of America, 2005. **102**(30): p. 10451-10453.

2. Novoselov, K.S., et al., *Electric field effect in atomically thin carbon films.* Science, 2004. **306**(5696): p. 666-669.

3. Wallace, P.R., *The Band Theory of Graphite.* Physical Review, 1947. **71**(9): p. 622-634.

4. Zhang, Y.B., et al., *Experimental observation of the quantum Hall effect and Berry's phase in graphene.* Nature, 2005. **438**(7065): p. 201-204.

5. Novoselov, K.S., et al., *Two-dimensional gas of massless Dirac fermions in graphene.* Nature, 2005. **438**(7065): p. 197-200.

6. Berger, C., et al., *Electronic confinement and coherence in patterned epitaxial graphene.* Science, 2006. **312**(5777): p. 1191-1196.

7. Bolotin, K.I., et al., *Ultrahigh electron mobility in suspended graphene.* Solid State Communications, 2008. **146**(9-10): p. 351-355.

8. Balandin, A.A., et al., *Superior thermal conductivity of single-layer graphene.* Nano Letters, 2008. **8**(3): p. 902-907.

9. Ghosh, S., et al., *Extremely high thermal conductivity of graphene: Prospects for thermal management applications in nanoelectronic circuits.* Applied Physics Letters, 2008. **92**(15).

10. Cai, W.W., et al., *Thermal Transport in Suspended and Supported Monolayer Graphene Grown by Chemical Vapor Deposition.* Nano Letters, 2010. **10**(5): p. 1645-1651.

11. Hone, J., et al., *Thermal conductivity of single-walled carbon nanotubes.* Physical Review B, 1999. **59**(4): p. R2514-R2516.

12. Kim, P., et al., *Thermal transport measurements of individual multiwalled nanotubes.* Physical Review Letters, 2001. **87**(21).

13. Pop, E., et al., *Thermal conductance of an individual single-wall carbon nanotube above room temperature.* Nano Letters, 2006. **6**(1): p. 96-100.

14. Berman, R., P.R.W. Hudson, and M. Martinez, *Nitrogen in Diamond - Evidence from Thermal-Conductivity.* Journal of Physics C-Solid State Physics, 1975. **8**(21): p. L430-L434.

15. Anthony, T.R., et al., *Thermal-Diffusivity of Isotopically Enriched C-12 Diamond.* Physical Review B, 1990. **42**(2): p. 1104-1111.

16. Olson, J.R., et al., *Thermal-Conductivity of Diamond between 170 and 1200-K and the Isotope Effect.* Physical Review B, 1993. **47**(22): p. 14850-14856.

17. Lemme, M.C., et al., *A graphene field-effect device.* Ieee Electron Device Letters, 2007. **28**(4): p. 282-284.

18. Lin, Y.M., et al., *Operation of Graphene Transistors at Gigahertz Frequencies.* Nano Letters, 2009. **9**(1): p. 422-426.

19. Lin, Y.M., et al., *100-GHz Transistors from Wafer-Scale Epitaxial Graphene.* Science, 2010. **327**(5966): p. 662-662.

20. Xia, F.N., et al., *Graphene Field-Effect Transistors with High On/Off Current Ratio and Large Transport Band Gap at Room Temperature.* Nano Letters, 2010. **10**(2): p. 715-718.

21. Lin, Y.M., et al., *Wafer-Scale Graphene Integrated Circuit.* Science, 2011. **332**(6035): p. 1294-1297.

22. Cheng, R., et al., *High-frequency self-aligned graphene transistors with transferred gate stacks.* Proceedings of the National Academy of Sciences of the United States of America, 2012. **109**(29): p. 11588-11592.

23. Han, S.J., et al., *Graphene radio frequency receiver integrated circuit.* Nature Communications, 2014. **5**.

24. Avouris, P., Z.H. Chen, and V. Perebeinos, *Carbon-based electronics.* Nature Nanotechnology, 2007. **2**(10): p. 605-615.

25. Geim, A.K., *Graphene: Status and Prospects.* Science, 2009. **324**(5934): p. 1530-1534.

26. Schwierz, F., *Graphene transistors.* Nature Nanotechnology, 2010. **5**(7): p. 487-496.

27. Han, M.Y., et al., *Energy band-gap engineering of graphene nanoribbons.* Physical Review Letters, 2007. **98**(20).

28. Li, X.L., et al., *Chemically derived, ultrasmooth graphene nanoribbon semiconductors.* Science, 2008. **319**(5867): p. 1229-1232.

29. Molitor, F., et al., *Transport gap in side-gated graphene constrictions.* Physical Review B, 2009. **79**(7).

30. Nair, R.R., et al., *Fine structure constant defines visual transparency of graphene.* Science, 2008. **320**(5881): p. 1308-1308.

31. Wang, F., et al., *Gate-variable optical transitions in graphene.* Science, 2008. **320**(5873): p. 206-209.

32. Sheehy, D.E. and J. Schmalian, *Optical transparency of graphene as determined by the fine-structure constant.* Physical Review B, 2009. **80**(19).

33. Lee, C., et al., *Measurement of the elastic properties and intrinsic strength of monolayer graphene.* Science, 2008. **321**(5887): p. 385-388.

34. Frank, I.W., et al., *Mechanical properties of suspended graphene sheets.* Journal of Vacuum Science & Technology B, 2007. **25**(6): p. 2558-2561.

35. Wang, X., L.J. Zhi, and K. Mullen, *Transparent, conductive graphene electrodes for dye-sensitized solar cells.* Nano Letters, 2008. **8**(1): p. 323-327.

36. Kim, K.S., et al., *Large-scale pattern growth of graphene films for stretchable transparent electrodes.* Nature, 2009. **457**(7230): p. 706-710.

37. Li, X.S., et al., *Transfer of Large-Area Graphene Films for High-Performance Transparent Conductive Electrodes.* Nano Letters, 2009. **9**(12): p. 4359-4363.

38. Bae, S., et al., *Roll-to-roll production of 30-inch graphene films for transparent electrodes.* Nature Nanotechnology, 2010. **5**(8): p. 574-578.

39. Xia, F.N., et al., *Ultrafast graphene photodetector.* Nature Nanotechnology, 2009. **4**(12): p. 839-843.

40. Mueller, T., F.N.A. Xia, and P. Avouris, *Graphene photodetectors for high-speed optical communications.* Nature Photonics, 2010. **4**(5): p. 297-301.

41. Bonaccorso, F., et al., *Graphene photonics and optoelectronics.* Nature Photonics, 2010. **4**(9): p. 611-622.

42. Gan, X.T., et al., *Chip-integrated ultrafast graphene photodetector with high responsivity.* Nature Photonics, 2013. **7**(11): p. 883-887.

43. Pan, D.Y., et al., *Li Storage Properties of Disordered Graphene Nanosheets.* Chemistry of Materials, 2009. **21**(14): p. 3136-3142.

44. Wu, Z.S., et al., *Doped Graphene Sheets As Anode Materials with Superhigh Rate and Large Capacity for Lithium Ion Batteries.* Acs Nano, 2011. **5**(7): p. 5463-5471.

45. Dean, C.R., et al., *Boron nitride substrates for high-quality graphene electronics.* Nature Nanotechnology, 2010. **5**(10): p. 722-726.

46. Mayorov, A.S., et al., *Micrometer-Scale Ballistic Transport in Encapsulated Graphene at Room Temperature.* Nano Letters, 2011. **11**(6): p. 2396-2399.

47. Britnell, L., et al., *Field-Effect Tunneling Transistor Based on Vertical Graphene Heterostructures.* Science, 2012. **335**(6071): p. 947-950.

48. Lee, K.H., et al., *Large-Scale Synthesis of High-Quality Hexagonal Boron Nitride Nanosheets for Large-Area Graphene Electronics.* Nano Letters, 2012. **12**(2): p. 714-718.

49. Britnell, L., et al., *Electron Tunneling through Ultrathin Boron Nitride Crystalline Barriers.* Nano Letters, 2012. **12**(3): p. 1707-1710.

50. Britnell, L., et al., *Strong Light-Matter Interactions in Heterostructures of Atomically Thin Films.* Science, 2013. **340**(6138): p. 1311-1314.

51. Georgiou, T., et al., *Vertical field-effect transistor based on graphene-WS2 heterostructures for flexible and transparent electronics.* Nature Nanotechnology, 2013. **8**(2): p. 100-103.

52. Yu, W.J., et al., *Vertically stacked multi-heterostructures of layered materials for logic transistors and complementary inverters.* Nature Materials, 2013. **12**(3): p. 246-252.

53. Roy, K., et al., *Graphene-MoS2 hybrid structures for multifunctional photoresponsive memory devices.* Nature Nanotechnology, 2013. **8**(11): p. 826-830.

54. Kretinin, A.V., et al., *Electronic Properties of Graphene Encapsulated with Different Two-Dimensional Atomic Crystals.* Nano Letters, 2014. **14**(6): p. 3270-3276.

55. Roy, T., et al., *Field-Effect Transistors Built from All Two-Dimensional Material Components.* Acs Nano, 2014. **8**(6): p. 6259-6264.

56. Das, S., et al., *All Two-Dimensional, Flexible, Transparent, and Thinnest Thin Film Transistor.* Nano Letters, 2014. **14**(5): p. 2861-2866.

57. Withers, F., et al., *Light-emitting diodes by band-structure engineering in van der Waals heterostructures.* Nature Materials, 2015. **14**(3): p. 301-306.

58. Geim, A.K. and I.V. Grigorieva, *Van der Waals heterostructures.* Nature, 2013. **499**(7459): p. 419-425.

59. Novoselov, K.S., et al., *2D materials and van der Waals heterostructures.* Science, 2016. **353**(6298).

60. Liu, Y., et al., *Van der Waals heterostructures and devices.* Nature Reviews Materials, 2016. **1**(9).

61. Bolotin, K.I., et al., *Temperature-dependent transport in suspended graphene.* Physical Review Letters, 2008. **101**(9).

62. Du, X., et al., *Approaching ballistic transport in suspended graphene.* Nature Nanotechnology, 2008. **3**(8): p. 491-495.

63. Ando, T., *Screening effect and impurity scattering in monolayer graphene.* Journal of the Physical Society of Japan, 2006. **75**(7).

64. Hwang, E.H., S. Adam, and S. Das Sarma, *Carrier transport in two-dimensional graphene layers.* Physical Review Letters, 2007. **98**(18).

65. Nomura, K. and A.H. MacDonald, *Quantum transport of massless dirac fermions.* Physical Review Letters, 2007. **98**(7).

66. Chen, J.H., et al., *Intrinsic and extrinsic performance limits of graphene devices on SiO2.* Nature Nanotechnology, 2008. **3**(4): p. 206-209.

67. Fratini, S. and F. Guinea, *Substrate-limited electron dynamics in graphene.* Physical Review B, 2008. **77**(19).

68. Ponomarenko, L.A., et al., *Effect of a High-kappa Environment on Charge Carrier Mobility in Graphene.* Physical Review Letters, 2009. **102**(20).

69. Giovannetti, G., et al., *Substrate-induced band gap in graphene on hexagonal boron nitride: Ab initio density functional calculations.* Physical Review B, 2007. **76**(7).

70. Liu, L., Y.P. Feng, and Z.X. Shen, *Structural and electronic properties of h-BN.* Physical Review B, 2003. **68**(10).

71. Watanabe, K., T. Taniguchi, and H. Kanda, *Direct-bandgap properties and evidence for ultraviolet lasing of hexagonal boron nitride single crystal.* Nature Materials, 2004. **3**(6): p. 404-409.

72. Young, A.F., et al., *Electronic compressibility of layer-polarized bilayer graphene.* Physical Review B, 2012. **85**(23).

73. Kuc, A., N. Zibouche, and T. Heine, *Influence of quantum confinement on the electronic structure of the transition metal sulfide TS2.* Physical Review B, 2011. **83**(24).

74. Chen, C.C., et al., *Thermoelectric transport across graphene/hexagonal boron nitride/graphene heterostructures.* Nano Research, 2015. **8**(2): p. 666-672.

75. D'Souza, R. and S. Mukherjee, *Thermoelectric transport in graphene/h-BN/graphene heterostructures: A computational study.* Physica E-Low-Dimensional Systems & Nanostructures, 2016. **81**: p. 96-101.

76. Frindt, R.F. and A.D. Yoffe, *Physical Properties of Layer Structures - Optical Properties and Photoconductivity of Thin Crystals of Molybdenum Disulphide.* Proceedings of the Royal Society of London Series a-Mathematical and Physical Sciences, 1963. **273**(1352): p. 69-+.

77. Wilson, J.A. and A.D. Yoffe, *The transition metal dichalcogenides discussion and interpretation of the observed optical, electrical and structural properties.* Advances in Physics, 1969. **18**(73): p. 193-335.

78. Chhowalla, M., et al., *The chemistry of two-dimensional layered transition metal dichalcogenide nanosheets.* Nature Chemistry, 2013. **5**(4): p. 263-275.

79. Podzorov, V., et al., *High-mobility field-effect transistors based on transition metal dichalcogenides.* Applied Physics Letters, 2004. **84**(17): p. 3301-3303.

80. Radisavljevic, B., et al., *Single-layer MoS2 transistors.* Nature Nanotechnology, 2011. **6**(3): p. 147-150.

81. Qiu, H., et al., *Electrical characterization of back-gated bi-layer MoS2 field-effect transistors and the effect of ambient on their performances.* Applied Physics Letters, 2012. **100**(12).

82. Das, S., et al., *High Performance Multilayer MoS2 Transistors with Scandium Contacts.* Nano Letters, 2013. **13**(1): p. 100-105.

83. Lee, H.S., et al., *MoS2 Nanosheet Phototransistors with Thickness-Modulated Optical Energy Gap.* Nano Letters, 2012. **12**(7): p. 3695-3700.

84. Lopez-Sanchez, O., et al., *Ultrasensitive photodetectors based on monolayer MoS2.* Nature Nanotechnology, 2013. **8**(7): p. 497-501.

85. Zhang, W.J., et al., *High-Gain Phototransistors Based on a CVD MoS2 Monolayer.* Advanced Materials, 2013. **25**(25): p. 3456-3461.

86. Kufer, D. and G. Konstantatos, *Highly Sensitive, Encapsulated MoS2 Photodetector with Gate Controllable Gain and Speed.* Nano Letters, 2015. **15**(11): p. 7307-7313.

87. Mak, K.F., et al., *Atomically Thin MoS2: A New Direct-Gap Semiconductor.* Physical Review Letters, 2010. **105**(13).

88. Tongay, S., et al., *Thermally Driven Crossover from Indirect toward Direct Bandgap in 2D Semiconductors: MoSe2 versus MoS2.* Nano Letters, 2012. **12**(11): p. 5576-5580.

89. Tonndorf, P., et al., *Photoluminescence emission and Raman response of monolayer MoS2, MoSe2, and WSe2.* Optics Express, 2013. **21**(4): p. 4908-4916.

90. Splendiani, A., et al., *Emerging photoluminescence in monolayer MoS2.* Nano Lett, 2010. **10**(4): p. 1271-5.

91. Zhang, Y., et al., *Direct observation of the transition from indirect to direct bandgap in atomically thin epitaxial MoSe2.* Nature Nanotechnology, 2014. **9**(2): p. 111-115.

92. Larentis, S., B. Fallahazad, and E. Tutuc, *Field-effect transistors and intrinsic mobility in ultra-thin MoSe2 layers.* Applied Physics Letters, 2012. **101**(22).

93. Chang, Y.H., et al., *Monolayer MoSe2 Grown by Chemical Vapor Deposition for Fast Photodetection.* Acs Nano, 2014. **8**(8): p. 8582-8590.

94. Pradhan, N.R., et al., *Ambipolar Molybdenum Diselenide Field-Effect Transistors: Field-Effect and Hall Mobilities.* Acs Nano, 2014. **8**(8): p. 7923-7929.

95. Chamlagain, B., et al., *Mobility Improvement and Temperature Dependence in MoSe2 Field-Effect Transistors on Parylene-C Substrate.* Acs Nano, 2014. **8**(5): p. 5079-5088.

96. Abderrahmane, A., et al., *High photosensitivity few-layered MoSe2 back-gated field-effect phototransistors.* Nanotechnology, 2014. **25**(36).

97. Bernardi, M., M. Palummo, and J.C. Grossman, *Extraordinary Sunlight Absorption and One Nanometer Thick Photovoltaics Using Two-Dimensional Monolayer Materials.* Nano Letters, 2013. **13**(8): p. 3664-3670.

98. Buscema, M., et al., *Large and Tunable Photothermoelectric Effect in Single-Layer MoS2.* Nano Letters, 2013. **13**(2): p. 358-363.

99. Jin, Z.L., et al., *A Revisit to High Thermoelectric Performance of Single-layer MoS2.* Scientific Reports, 2015. **5**.

100. Kumar, S. and U. Schwingenschlögl, *Thermoelectric Response of Bulk and Monolayer MoSe2 and WSe2.* Chemistry of Materials, 2015. **27**(4): p. 1278-1284.

101. Hippalgaonkar, K., et al., *High thermoelectric power factor in two-dimensional crystals of MoS2.* Physical Review B, 2017. **95**(11).

102. Brown, A. and S. Rundqvist, *Refinement of the crystal structure of black phosphorus.* Acta Crystallographica, 1965. **19**(4): p. 684-685.

103. Takeda, K. and K. Shiraishi, *Theoretical Possibility of Stage Corrugation in Si and Ge Analogs of Graphite.* Physical Review B, 1994. **50**(20): p. 14916-14922.

104. Cahangirov, S., et al., *Two- and One-Dimensional Honeycomb Structures of Silicon and Germanium.* Physical Review Letters, 2009. **102**(23).

105. Fleurence, A., et al., *Experimental Evidence for Epitaxial Silicene on Diboride Thin Films.* Physical Review Letters, 2012. **108**(24).

106. Lin, C.L., et al., *Structure of Silicene Grown on Ag(111).* Applied Physics Express, 2012. **5**(4).

107. Vogt, P., et al., *Silicene: Compelling Experimental Evidence for Graphenelike Two-Dimensional Silicon.* Physical Review Letters, 2012. **108**(15).

108. Davila, M.E., et al., *Germanene: a novel two-dimensional germanium allotrope akin to graphene and silicene.* New Journal of Physics, 2014. **16**.

109. Derivaz, M., et al., *Continuous Germanene Layer on Al(111).* Nano Letters, 2015. **15**(4): p. 2510-2516.

110. Molle, A., et al., *Hindering the Oxidation of Silicene with Non-Reactive Encapsulation.* Advanced Functional Materials, 2013. **23**(35): p. 4340-4344.

111. Cinquanta, E., et al., *Getting through the Nature of Silicene: An sp(2)-sp(3) Two-Dimensional Silicon Nanosheet.* Journal of Physical Chemistry C, 2013. **117**(32): p. 16719-16724.

112. Tao, L., et al., *Silicene field-effect transistors operating at room temperature.* Nature Nanotechnology, 2015. **10**(3): p. 227-231.

113. Castellanos-Gomez, A., et al., *Isolation and characterization of few-layer black phosphorus.* 2d Materials, 2014. **1**(2).

114. Koenig, S.P., et al., *Electric field effect in ultrathin black phosphorus.* Applied Physics Letters, 2014. **104**(10).

115. Xia, F.N., H. Wang, and Y.C. Jia, *Rediscovering black phosphorus as an anisotropic layered material for optoelectronics and electronics.* Nature Communications, 2014. **5**.

116. Liu, H., et al., *Phosphorene: An Unexplored 2D Semiconductor with a High Hole Mobility.* Acs Nano, 2014. **8**(4): p. 4033-4041.

117. Qiao, J.S., et al., *High-mobility transport anisotropy and linear dichroism in few-layer black phosphorus.* Nature Communications, 2014. **5**.

118. Li, L.K., et al., *Black phosphorus field-effect transistors.* Nature Nanotechnology, 2014. **9**(5): p. 372-377.

119. Buscema, M., et al., *Fast and Broadband Photoresponse of Few-Layer Black Phosphorus Field-Effect Transistors.* Nano Letters, 2014. **14**(6): p. 3347-3352.

120. Engel, M., M. Steiner, and P. Avouris, *Black Phosphorus Photodetector for Multispectral, High-Resolution Imaging.* Nano Letters, 2014. **14**(11): p. 6414-6417.

121. Hu, P.A., et al., *Synthesis of Few-Layer GaSe Nanosheets for High Performance Photodetectors.* Acs Nano, 2012. **6**(7): p. 5988-5994.

122. Late, D.J., et al., *GaS and GaSe Ultrathin Layer Transistors.* Advanced Materials, 2012. **24**(26): p. 3549-3554.

123. Gomes, L.C., A. Carvalho, and A.H.C. Neto, *Enhanced piezoelectricity and modified dielectric screening of two-dimensional group-IV monochalcogenides.* Physical Review B, 2015. **92**(21).

124. Gomes, L.C. and A. Carvalho, *Phosphorene analogues: Isoelectronic two-dimensional group-IV monochalcogenides with orthorhombic structure.* Physical Review B, 2015. **92**(8).

125. Subramanian, M.A., et al., *A New High-Temperature Superconductor - Bi2sr3-Xcaxcu2o8+Y.* Science, 1988. **239**(4843): p. 1015-1017.

126. Cava, R.J., et al., *Superconductivity near 70-K in a New Family of Layered Copper Oxides.* Nature, 1988. **336**(6196): p. 211-214.

127. Takada, K., et al., *Superconductivity in two-dimensional CoO2 layers.* Nature, 2003. **422**(6927): p. 53-55.

128. Osada, M. and T. Sasaki, *Exfoliated oxide nanosheets: new solution to nanoelectronics.* Journal of Materials Chemistry, 2009. **19**(17): p. 2503-2511.

129. Naguib, M., et al., *Two-Dimensional Nanocrystals Produced by Exfoliation of Ti3AlC2.* Advanced Materials, 2011. **23**(37): p. 4248-4253.

130. Naguib, M., et al., *Two-Dimensional Transition Metal Carbides.* Acs Nano, 2012. **6**(2): p. 1322-1331.

131. Khazaei, M., et al., *Novel Electronic and Magnetic Properties of Two-Dimensional Transition Metal Carbides and Nitrides.* Advanced Functional Materials, 2013. **23**(17): p. 2185-2192.

132. Anasori, B., et al., *Two-Dimensional, Ordered, Double Transition Metals Carbides (MXenes).* Acs Nano, 2015. **9**(10): p. 9507-9516.

133. Moore, G.E., *Cramming More Components onto Integrated Circuits.* Electronics, 1965. **38**(8): p. 114-117.

134. Lo, S., et al., *Quantum-mechanical modeling of electron tunneling current from the inversion layer of ultra-thin-oxide nMOSFET's.* IEEE Electron Device Letters, 1997. **18**(5): p. 209-211.

135. Muller, D.A., et al., *The electronic structure at the atomic scale of ultrathin gate oxides.* Nature, 1999. **399**(6738): p. 758-761.

136. Hirose, M., et al., *Fundamental limit of gate oxide thickness scaling in advanced MOSFETs.* Semiconductor Science and Technology, 2000. **15**(5): p. 485-490.

137. Wu, E.Y., J.H. Stathis, and L.K. Han, *Ultra-thin oxide reliability for ULSI applications.* Semiconductor Science and Technology, 2000. **15**(5): p. 425-435.

138. Kingon, A.I., J.P. Maria, and S.K. Streiffer, *Alternative dielectrics to silicon dioxide for memory and logic devices.* Nature, 2000. **406**(6799): p. 1032-1038.

139. Wilk, G.D., R.M. Wallace, and J.M. Anthony, *High-kappa gate dielectrics: Current status and materials properties considerations.* Journal of Applied Physics, 2001. **89**(10): p. 5243-5275.

140. Mistry, K., et al., *A 45nm logic technology with high-k plus metal gate transistors, strained silicon, 9 Cu interconnect layers, 193nm dry patterning, and 100% Pb-free packaging.* 2007 Ieee International Electron Devices Meeting, Vols 1 and 2, 2007: p. 247-+.

141. Bohr, M.T., et al., *The high-k solution.* Ieee Spectrum, 2007. **44**(10): p. 29-35.

142. Strukov, D.B., et al., *The missing memristor found.* Nature, 2008. **453**(7191): p. 80-83.

143. Chua, L., *Memristor-The missing circuit element.* IEEE Transactions on Circuit Theory, 1971. **18**(5): p. 507-519.

144. Dearnaley, G., A.M. Stoneham, and D.V. Morgan, *Electrical Phenomena in Amorphous Oxide Films.* Reports on Progress in Physics, 1970. **33**(11): p. 1129-+.

145. Hickmott, T.W., *Low-Frequency Negative Resistance in Thin Anodic Oxide Films.* Journal of Applied Physics, 1962. **33**(9): p. 2669-&.

146. Yang, J.J., et al., *Memristive switching mechanism for metal/oxide/metal nanodevices.* Nature Nanotechnology, 2008. **3**(7): p. 429-433.

147. Linn, E., et al., *Complementary resistive switches for passive nanocrossbar memories.* Nature Materials, 2010. **9**(5): p. 403-406.

148. Kim, K.H., et al., *Nanoscale resistive memory with intrinsic diode characteristics and long endurance.* Applied Physics Letters, 2010. **96**(5).

149. Lee, M.-J., et al., *A fast, high-endurance and scalable non-volatile memory device made from asymmetric Ta2O5−x/TaO2−x bilayer structures.* Nature Materials, 2011. **10**: p. 625.

150. Chang, S.H., et al., *Oxide Double-Layer Nanocrossbar for Ultrahigh-Density Bipolar Resistive Memory.* Advanced Materials, 2011. **23**(35): p. 4063-+.

151. Jo, S.H., et al., *Nanoscale Memristor Device as Synapse in Neuromorphic Systems.* Nano Letters, 2010. **10**(4): p. 1297-1301.

152. Yu, S.M., et al., *An Electronic Synapse Device Based on Metal Oxide Resistive Switching Memory for Neuromorphic Computation.* Ieee Transactions on Electron Devices, 2011. **58**(8): p. 2729-2737.

153. Prezioso, M., et al., *Training and operation of an integrated neuromorphic network based on metal-oxide memristors.* Nature, 2015. **521**(7550): p. 61-64.

154. Hu, S.G., et al., *Associative memory realized by a reconfigurable memristive Hopfield neural network.* Nature Communications, 2015. **6**.

155. Lee, H.Y., et al., *HfOx Bipolar Resistive Memory With Robust Endurance Using AlCu as Buffer Electrode.* Ieee Electron Device Letters, 2009. **30**(7): p. 703-705.

156. Lee, H.Y., et al., *Low-Power and Nanosecond Switching in Robust Hafnium Oxide Resistive Memory With a Thin Ti Cap.* Ieee Electron Device Letters, 2010. **31**(1): p. 44-46.

157. Govoreanu, B., et al. *10×10nm²Hf/HfO<inf>x</inf>crossbar resistive RAM with excellent performance, reliability and low-energy operation*. in *2011 International Electron Devices Meeting*. 2011.

158. Mei, C.Y., et al., *28-nm 2T High-K Metal Gate Embedded RRAM With Fully Compatible CMOS Logic Processes.* Ieee Electron Device Letters, 2013. **34**(10): p. 1253-1255.

159. Yoon, J.H., et al., *Pt/Ta2O5/HfO2−x/Ti Resistive Switching Memory Competing with Multilevel NAND Flash.* Advanced Materials, 2015. **27**(25): p. 3811-3816.

160. Wedig, A., et al., *Nanoscale cation motion in TaOx, HfOx and TiOx memristive systems.* Nature Nanotechnology, 2016. **11**(1): p. 67-+.

161. Jiang, H., et al., *Sub-10 nm Ta Channel Responsible for Superior Performance of a HfO2 Memristor.* Scientific Reports, 2016. **6**.

162. Li, C., et al., *Analogue signal and image processing with large memristor crossbars.* Nature Electronics, 2018. **1**(1): p. 52-59.

163. Chow, R., et al., *Reactive Evaporation of Low-Defect Density Hafnia.* Applied Optics, 1993. **32**(28): p. 5567-5574.

164. Ibegazene, H., S. Alperine, and C. Diot, *Yttria-Stabilized Hafnia-Zirconia Thermal Barrier Coatings - the Influence of Hafnia Addition on Tbc Structure and High-Temperature Behavior.* Journal of Materials Science, 1995. **30**(4): p. 938-951.

165. Aarik, J., et al., *Optical characterization of HfO2 thin films grown by atomic layer deposition.* Thin Solid Films, 2004. **466**(1-2): p. 41-47.

166. Shimada, S. and T. Aketo, *High-temperature oxidation at 1500 degrees and 1600 degrees C of SiC/graphite coated with sol-gel-derived HfO2.* Journal of the American Ceramic Society, 2005. **88**(4): p. 845-849.

167. Jerman, M., Z.H. Qiao, and D. Mergel, *Refractive index of thin films of SiO2, ZrO2, and HfO2 as a function of the films' mass density.* Applied Optics, 2005. **44**(15): p. 3006-3012.

168. Modreanu, M., et al., *Investigation of thermal annealing effects on microstructural and optical properties of HfO(2) thin films.* Applied Surface Science, 2006. **253**(1): p. 328-334.

169. Gallais, L., et al., *Laser damage resistance of hafnia thin films deposited by electron beam deposition, reactive low voltage ion plating, and dual ion beam sputtering.* Applied Optics, 2008. **47**(13): p. C107-C113.

170. Jo, I., et al., *Low-Frequency Acoustic Phonon Temperature Distribution in Electrically Biased Graphene.* Nano Letters, 2011. **11**(1): p. 85-90.

171. Pop, E., *Energy Dissipation and Transport in Nanoscale Devices.* Nano Research, 2010. **3**(3): p. 147-169.

172. Pop, E., V. Varshney, and A.K. Roy, *Thermal properties of graphene: Fundamentals and applications.* Mrs Bulletin, 2012. **37**(12): p. 1273-1281.

173. Pop, E., S. Sinha, and K.E. Goodson, *Heat generation and transport in nanometer-scale transistors.* Proceedings of the Ieee, 2006. **94**(8): p. 1587-1601.

174. Flik, M.I., B.I. Choi, and K.E. Goodson, *Heat-Transfer Regimes in Microstructures.* Journal of Heat Transfer-Transactions of the Asme, 1992. **114**(3): p. 666-674.

175. Ju, Y.S. and K.E. Goodson, *Phonon scattering in silicon films with thickness of order 100 nm.* Applied Physics Letters, 1999. **74**(20): p. 3005-3007.

176. Li, D.Y., et al., *Thermal conductivity of individual silicon nanowires.* Applied Physics Letters, 2003. **83**(14): p. 2934-2936.

177. Regner, K.T., et al., *Broadband phonon mean free path contributions to thermal conductivity measured using frequency domain thermoreflectance*. Nature Communications, 2013. **4**.

178. Kittel, C. and H. Kroemer, *Thermal physics*. 2d ed. 1980, San Francisco: W. H. Freeman. xvii, 473 p.

179. Kittel, C., *Introduction to solid state physics*. 8th ed. 2005, Hoboken, NJ: Wiley. xix, 680 p.

180. Chen, G., *Nanoscale energy transport and conversion : a parallel treatment of electrons, molecules, phonons, and photons*. MIT-Pappalardo series in mechanical engineering. 2005, New York: Oxford University Press. xxiii, 531 p.

181. Fourier, J.-B.-J. and A. Freeman, *The analytical theory of heat*. 1878, Cambridge Eng.: The University Press; etc. xxiii, 466 p.

182. Rohsenow, W.M. and H.Y. Choi, *Heat, mass, and momentum transfer*. Prentice-Hall series in engineering of the physical sciences. 1961, Englewood Cliffs, N.J.,: Prentice-Hall. 537 p.

183. Purdue University. Thermophysical Properties Research Center. and Y.S. Touloukian, *Thermophysical properties of matter; [the TPRC data series; a comprehensive compilation of data*. 1970, New York,: IFI/Plenum.

184. Glassbrenner, C.J. and G.A. Slack, *Thermal Conductivity of Silicon + Germanium from 3 Degrees K to Melting Point.* Physical Review, 1964. **134**(4a): p. 1058-+.

185. Bergman, T.L. and F.P. Incropera, *Fundamentals of heat and mass transfer*. 7th ed. 2011, Hoboken, NJ: Wiley. xxiii, 1048 p.

186. Kelly, B.T., *Physics of graphite*. 1981, London ; Englewood, N.J.: Applied Science. x, 477 p.

187. Cooper, M.G., B.B. Mikic, and Yovanovi.Mm, *Thermal Contact Conductance.* International Journal of Heat and Mass Transfer, 1969. **12**(3): p. 279-&.

188. Mikic, B.B., *Thermal Contact Conductance - Theoretical Considerations.* International Journal of Heat and Mass Transfer, 1974. **17**(2): p. 205-214.

189. Kapitza, P.L., *Heat transfer and superfluidity of helium II.* Journal of Physics-Ussr, 1941. **5**(1-6): p. 59-69.

190. Pollack, G.L., *Kapitza Resistance.* Reviews of Modern Physics, 1969. **41**(1): p. 48-&.

191. Swartz, E.T. and R.O. Pohl, *Thermal-Boundary Resistance.* Reviews of Modern Physics, 1989. **61**(3): p. 605-668.

192. Stoner, R.J. and H.J. Maris, *Kapitza Conductance and Heat-Flow between Solids at Temperatures from 50 to 300 K.* Physical Review B, 1993. **48**(22): p. 16373-16387.

193. Costescu, R.M., M.A. Wall, and D.G. Cahill, *Thermal conductance of epitaxial interfaces.* Physical Review B, 2003. **67**(5).

194. Lyeo, H.K. and D.G. Cahill, *Thermal conductance of interfaces between highly dissimilar materials.* Physical Review B, 2006. **73**(14).

195. Gundrum, B.C., D.G. Cahill, and R.S. Averback, *Thermal conductance of metal-metal interfaces.* Physical Review B, 2005. **72**(24).

196. Wilson, R.B. and D.G. Cahill, *Experimental Validation of the Interfacial Form of the Wiedemann-Franz Law.* Physical Review Letters, 2012. **108**(25).

197. Wirtz, L. and A. Rubio, *The phonon dispersion of graphite revisited.* Solid State Communications, 2004. **131**(3-4): p. 141-152.

198. Chen, Z., et al., *Anisotropic Debye model for the thermal boundary conductance.* Physical Review B, 2013. **87**(12).

199. Desorbo, W. and W.W. Tyler, *The Specific Heat of Graphite from 13-Degrees-K to 300-Degrees-K.* Journal of Chemical Physics, 1953. **21**(10): p. 1660-1663.

200. Pop, E., et al., *Electrical and thermal transport in metallic single-wall carbon nanotubes on insulating substrates.* Journal of Applied Physics, 2007. **101**(9).

201. Liao, A.D., et al., *Thermally Limited Current Carrying Ability of Graphene Nanoribbons.* Physical Review Letters, 2011. **106**(25).

202. Zheng, J.X., et al., *Interfacial Properties of Bilayer and Trilayer Graphene on Metal Substrates.* Scientific Reports, 2013. **3**.

203. Giovannetti, G., et al., *Doping graphene with metal contacts.* Physical Review Letters, 2008. **101**(2).

204. Khomyakov, P.A., et al., *First-principles study of the interaction and charge transfer between graphene and metals.* Physical Review B, 2009. **79**(19).

205. Schultz, B.J., et al., *On chemical bonding and electronic structure of graphene-metal contacts.* Chemical Science, 2013. **4**(1): p. 494-502.

206. Cheianov, V.V. and V.I. Fal'ko, *Selective transmission of Dirac electrons and ballistic magnetoresistance of n-p junctions in graphene.* Physical Review B, 2006. **74**(4).

207. Park, C.H., et al., *Anisotropic behaviours of massless Dirac fermions in graphene under periodic potentials.* Nature Physics, 2008. **4**(3): p. 213-217.

208. Koh, Y.K., et al., *Heat Conduction across Monolayer and Few-Layer Graphenes.* Nano Letters, 2010. **10**(11): p. 4363-4368.

209. Huang, B. and Y.K. Koh, *Improved topological conformity enhances heat conduction across metal contacts on transferred graphene.* Carbon, 2016. **105**: p. 268-274.

210. Huang, B. and Y.K. Koh, *Negligible Electronic Contribution to Heat Transfer across Intrinsic Metal/Graphene Interfaces.* Advanced Materials Interfaces, 2017. **4**(20).

211. Aizawa, T., et al., *Phonon-Dispersion in Monolayer Graphite Formed on Ni(111) and Ni(001).* Surface Science, 1990. **237**(1-3): p. 194-202.

212. Aizawa, T., et al., *Phonon-Dispersion of Monolayer Graphite on Pt(111) and Nbc Surfaces - Bond Softening and Interface Structures.* Surface Science, 1992. **260**(1-3): p. 311-318.

213. Allard, A. and L. Wirtz, *Graphene on Metallic Substrates: Suppression of the Kohn Anomalies in the Phonon Dispersion.* Nano Letters, 2010. **10**(11): p. 4335-4340.

214. Chen, L., Z. Huang, and S. Kumar, *Phonon transmission and thermal conductance across graphene/Cu interface.* Applied Physics Letters, 2013. **103**(12).

215. Chen, L., Z. Huang, and S. Kumar, *Impact of bonding at multi-layer graphene/metal Interfaces on thermal boundary conductance.* Rsc Advances, 2014. **4**(68): p. 35852-35861.

216. Gong, C., et al., *Metal-Graphene-Metal Sandwich Contacts for Enhanced Interface Bonding and Work Function Control.* Acs Nano, 2012. **6**(6): p. 5381-5387.

217. Franklin, A.D., et al., *Double Contacts for Improved Performance of Graphene Transistors.* Ieee Electron Device Letters, 2012. **33**(1): p. 17-19.

218. Mao, R., et al., *First-principles calculation of thermal transport in metal/graphene systems.* Physical Review B, 2013. **87**(16).

219. Schmidt, A.J., et al., *Thermal conductance and phonon transmissivity of metal-graphite interfaces.* Journal of Applied Physics, 2010. **107**(10).

220. Gengler, J.J., et al., *Limited thermal conductance of metal-carbon interfaces.* Journal of Applied Physics, 2012. **112**(9).

221. Hopkins, P.E., et al., *Manipulating Thermal Conductance at Metal-Graphene Contacts via Chemical Functionalization.* Nano Letters, 2012. **12**(2): p. 590-595.

222. Yang, J., et al., *Thermal conductance imaging of graphene contacts.* Journal of Applied Physics, 2014. **116**(2).

223. Foley, B.M., et al., *Modifying Surface Energy of Graphene via Plasma-Based Chemical Functionalization to Tune Thermal and Electrical Transport at Metal Interfaces.* Nano Letters, 2015. **15**(8): p. 4876-4882.

224. Walton, S.G., et al., *Plasma-based chemical functionalization of graphene to control the thermal transport at graphene-metal interfaces.* Surface & Coatings Technology, 2017. **314**: p. 148-154.

225. Keren, F., et al., *Titanium Contacts to Graphene: Process-Induced Variability in Electronic and Thermal Transport.* Nanotechnology, 2018.

226. Jiang, T., et al., *Covalent bonding modulated graphene-metal interfacial thermal transport.* Nanoscale, 2016. **8**(21): p. 10993-11001.

227. Zhang, C.W., et al., *Electron contributions to the heat conduction across Au/graphene/Au interfaces.* Carbon, 2017. **115**: p. 665-671.

228. Losego, M.D., et al., *Effects of chemical bonding on heat transport across interfaces.* Nature Materials, 2012. **11**(6): p. 502-506.

229. Olson, D.H., et al., *The influence of titanium adhesion layer oxygen stoichiometry on thermal boundary conductance at gold contacts.* Applied Physics Letters, 2018. **112**(17).

230. Liu, Z., et al., *Direct Growth of Graphene/Hexagonal Boron Nitride Stacked Layers.* Nano Letters, 2011. **11**(5): p. 2032-2037.

231. Shi, Y.M., et al., *van der Waals Epitaxy of MoS2 Layers Using Graphene As Growth Templates.* Nano Letters, 2012. **12**(6): p. 2784-2791.

232. Wang, M., et al., *A Platform for Large-Scale Graphene Electronics - CVD Growth of Single-Layer Graphene on CVD-Grown Hexagonal Boron Nitride.* Advanced Materials, 2013. **25**(19): p. 2746-2752.

233. Zhang, C.H., et al., *Direct growth of large-area graphene and boron nitride heterostructures by a co-segregation method.* Nature Communications, 2015. **6**.

234. Yang, W., et al., *Epitaxial growth of single-domain graphene on hexagonal boron nitride.* Nature Materials, 2013. **12**(9): p. 792-797.

235. Lin, Y.C., et al., *Atomically Thin Heterostructures Based on Single-Layer Tungsten Diselenide and Graphene.* Nano Letters, 2014. **14**(12): p. 6936-6941.

236. Yan, A.M., et al., *Direct Growth of Single- and Few-Layer MoS2 on h-BN with Preferred Relative Rotation Angles.* Nano Letters, 2015. **15**(10): p. 6324-6331.

237. Decker, R., et al., *Local Electronic Properties of Graphene on a BN Substrate via Scanning Tunneling Microscopy.* Nano Letters, 2011. **11**(6): p. 2291-2295.

238. Sachs, B., et al., *Adhesion and electronic structure of graphene on hexagonal boron nitride substrates.* Physical Review B, 2011. **84**(19).

239. Xue, J.M., et al., *Scanning tunnelling microscopy and spectroscopy of ultra-flat graphene on hexagonal boron nitride.* Nature Materials, 2011. **10**(4): p. 282-285.

240. Slotman, G.J., et al., *Phonons and electron-phonon coupling in graphene-h-BN heterostructures.* Annalen Der Physik, 2014. **526**(9-10): p. 381-386.

241. Yan, Z.Q., et al., *Phonon transport at the interfaces of vertically stacked graphene and hexagonal boron nitride heterostructures.* Nanoscale, 2016. **8**(7): p. 4037-4046.

242. Mao, R., et al., *Phonon engineering in nanostructures: Controlling interfacial thermal resistance in multilayer-graphene/dielectric heterojunctions.* Applied Physics Letters, 2012. **101**(11).

243. Chen, C.C., et al., *Thermal interface conductance across a graphene/hexagonal boron nitride heterojunction.* Applied Physics Letters, 2014. **104**(8).

244. Zhang, J.C., Y. Hong, and Y.A. Yue, *Thermal transport across graphene and single layer hexagonal boron nitride.* Journal of Applied Physics, 2015. **117**(13).

245. Liu, Y., et al., *Thermal Conductance of the 2D MoS2/h-BN and graphene/h-BN Interfaces.* Scientific Reports, 2017. **7**.

246. Daehee, K., et al., *Energy dissipation mechanism revealed by spatially resolved Raman thermometry of graphene/hexagonal boron nitride heterostructure devices.* 2D Materials, 2018. **5**(2): p. 025009.

247. Choi, D., et al., *Large Reduction of Hot Spot Temperature in Graphene Electronic Devices with Heat-Spreading Hexagonal Boron Nitride.* Acs Applied Materials & Interfaces, 2018. **10**(13): p. 11101-11107.

248. Fang, H., et al., *High-Performance Single Layered WSe2 p-FETs with Chemically Doped Contacts.* Nano Letters, 2012. **12**(7): p. 3788-3792.

249. Liu, W., et al., *Role of Metal Contacts in Designing High-Performance Monolayer n-Type WSe2 Field Effect Transistors.* Nano Letters, 2013. **13**(5): p. 1983-1990.

250. Kappera, R., et al., *Phase-engineered low-resistance contacts for ultrathin MoS2 transistors.* Nature Materials, 2014. **13**(12): p. 1128-1134.

251. Kang, J.H., W. Liu, and K. Banerjee, *High-performance MoS2 transistors with low-resistance molybdenum contacts.* Applied Physics Letters, 2014. **104**(9).

252. Akinwande, D., N. Petrone, and J. Hone, *Two-dimensional flexible nanoelectronics.* Nature Communications, 2014. **5**.

253. Korn, T., et al., *Low-temperature photocarrier dynamics in monolayer MoS2.* Applied Physics Letters, 2011. **99**(10).

254. Cakir, D. and F.M. Peeters, *Dependence of the electronic and transport properties of metal-MoSe2 interfaces on contact structures.* Physical Review B, 2014. **89**(24).

255. Pan, Y.Y., et al., *Interfacial Properties of Monolayer MoSe2-Metal Contacts.* Journal of Physical Chemistry C, 2016. **120**(24): p. 13063-13070.

256. Lee, E.J.H., et al., *Contact and edge effects in graphene devices.* Nature Nanotechnology, 2008. **3**(8): p. 486-490.

257. Mao, R., B.D. Kong, and K.W. Kim, *Thermal transport properties of metal/MoS2 interfaces from first principles.* Journal of Applied Physics, 2014. **116**(3).

258. Liu, J., G.M. Choi, and D.G. Cahill, *Measurement of the anisotropic thermal conductivity of molybdenum disulfide by the time-resolved magneto-optic Kerr effect.* Journal of Applied Physics, 2014. **116**(23).

259. Yan, Z.Q., et al., *The Role of Interfacial Electronic Properties on Phonon Transport in Two-Dimensional MoS2 on Metal Substrates.* Acs Applied Materials & Interfaces, 2016. **8**(48): p. 33299-33306.

260. Taube, A., et al., *Temperature-Dependent Thermal Properties of Supported MoS2 Monolayers.* Acs Applied Materials & Interfaces, 2015. **7**(9): p. 5061-5065.

261. Yalon, E., et al., *Temperature-Dependent Thermal Boundary Conductance of Monolayer MoS2 by Raman Thermometry.* ACS Applied Materials & Interfaces, 2017. **9**(49): p. 43013-43020.

262. Yasaei, P., et al., *Interfacial Thermal Transport in Monolayer MoS2- and Graphene-Based Devices.* Advanced Materials Interfaces, 2017. **4**(17).

263. Yalon, E., et al., *Energy Dissipation in Monolayer MoS2 Electronics.* Nano Letters, 2017. **17**(6): p. 3429-3433.

264. Jiang, P.Q., et al., *Probing Anisotropic Thermal Conductivity of Transition Metal Dichalcogenides MX2 (M = Mo, W and X = S, Se) using Time-Domain Thermoreflectance.* Advanced Materials, 2017. **29**(36).

265. Yarali, M., et al., *Effect of Metal Doping and Vacancies on the Thermal Conductivity of Monolayer Molybdenum Diselenide.* Acs Applied Materials & Interfaces, 2018. **10**(5): p. 4921-4928.

266. Zhequan, Y., Y. Mina, and K. Satish, *Influence of defects and doping on phonon transport properties of monolayer MoSe2.* 2D Materials, 2018.

267. Zhang, X., et al., *Measurement of Lateral and Interfacial Thermal Conductivity of Single- and Bilayer MoS2 and MoSe2 Using Refined Optothermal Raman Technique.* Acs Applied Materials & Interfaces, 2015. **7**(46): p. 25923-25929.

268. Hausmann, D.M. and R.G. Gordon, *Surface morphology and crystallinity control in the atomic layer deposition (ALD) of hafnium and zirconium oxide thin films.* Journal of Crystal Growth, 2003. **249**(1-2): p. 251-261.

269. Hackley, J.C. and T. Gougousi, *Properties of atomic layer deposited HfO2 thin films.* Thin Solid Films, 2009. **517**(24): p. 6576-6583.

270. Balk, P., *Dielectrics in Microelectronics - Problems and Perspectives.* Journal of Non-Crystalline Solids, 1995. **187**: p. 1-9.

271. Houssa, M., et al., *Electrical properties of high-κ gate dielectrics: Challenges, current issues, and possible solutions*. Materials Science and Engineering: R: Reports, 2006. **51**(4): p. 37-85.

272. Lee, S.M., D.G. Cahill, and T.H. Allen, *Thermal-Conductivity of Sputtered Oxide-Films.* Physical Review B, 1995. **52**(1): p. 253-257.

273. Hinz, M., et al., *High resolution vacuum scanning thermal microscopy of HfO(2) and SiO(2).* Applied Physics Letters, 2008. **92**(4).

274. Panzer, M.A., et al., *Thermal Properties of Ultrathin Hafnium Oxide Gate Dielectric Films.* Ieee Electron Device Letters, 2009. **30**(12): p. 1269-1271.

275. Scott, E.A., et al., *Thermal conductivity and thermal boundary resistance of atomic layer deposited high-k dielectric aluminum oxide, hafnium oxide, and titanium oxide thin films on silicon.* Apl Materials, 2018. **6**(5).

276. Scott, E.A., et al., *Thermal resistance and heat capacity in hafnium zirconium oxide (Hf1-xZrxO2) dielectrics and ferroelectric thin films.* Applied Physics Letters, 2018. **113**(19).

277. Todd, S.S., *Heat Capacities at Low Temperatures and Entropies at 298.16-Degrees-K of Hafnium Dioxide and Hafnium Tetrachloride.* Journal of the American Chemical Society, 1953. **75**(12): p. 3035-3036.

278. Zhou, W., et al., *Heat capacity of hafnia at low temperature.* Journal of Chemical Thermodynamics, 2011. **43**(6): p. 970-973.

279. Rupp, J. and R. Birringer, *Enhanced Specific-Heat-Capacity (Cp) Measurements (150-300 K) of Nanometer-Sized Crystalline Materials.* Physical Review B, 1987. **36**(15): p. 7888-7890.

280. Wagner, M., *Structure and Thermodynamic Properties of Nanocrystalline Metals.* Physical Review B, 1992. **45**(2): p. 635-639.

281. Wang, L., et al., *Enhancement of molar heat capacity of nanostructured Al2O3.* Journal of Nanoparticle Research, 2001. **3**(5-6): p. 483-487.

282. Denlinger, D.W., et al., *Thin-Film Microcalorimeter for Heat-Capacity Measurements from 1.5-K to 800-K.* Review of Scientific Instruments, 1994. **65**(4): p. 946-958.

283. Lai, S.L., et al., *Heat capacity measurements of Sn nanostructures using a thin-film differential scanning calorimeter with 0.2 nJ sensitivity.* Applied Physics Letters, 1997. **70**(1): p. 43-45.

284. Yu, J., et al., *Investigation of a microcalorimeter for thin-film heat capacity measurement.* Chinese Physics Letters, 2005. **22**(9): p. 2429-2432.

285. Ou, M.N., et al., *Thermal and electrical transport properties of a single nickel nanowire.* Physica Status Solidi B-Basic Solid State Physics, 2007. **244**(12): p. 4512-4517.

286. Tian, H.X., et al., *Volumetric Heat Capacity Enhancement in Thin Films of Amorphous Fluorocarbon Polymers.* Journal of Heat Transfer-Transactions of the Asme, 2012. **134**(8).

287. Schmidt, A.J., R. Cheaito, and M. Chiesa, *A frequency-domain thermoreflectance method for the characterization of thermal properties.* Review of Scientific Instruments, 2009. **80**(9).

288. Liu, J., et al., *Simultaneous measurement of thermal conductivity and heat capacity of bulk and thin film materials using frequency-dependent transient thermoreflectance method.* Review of Scientific Instruments, 2013. **84**(3).

289. Wei, C.D., et al., *Invited Article: Micron resolution spatially resolved measurement of heat capacity using dual-frequency time-domain thermoreflectance.* Review of Scientific Instruments, 2013. **84**(7).

290. Olson, D.H., et al., *Size Effects on the Cross-Plane Thermal Conductivity of Transparent Conducting Indium Tin Oxide (ITO) and Fluorine Tin Oxide (FTO) Thin Films.* IEEE Transactions on Components, Packaging and Manufacturing Technology, 2018: p. 1-1.

291. Williams, C.C. and H.K. Wickramasinghe, *Scanning Thermal Profiler.* Applied Physics Letters, 1986. **49**(23): p. 1587-1589.

292. Majumdar, A., J.P. Carrejo, and J. Lai, *Thermal Imaging Using the Atomic Force Microscope.* Applied Physics Letters, 1993. **62**(20): p. 2501-2503.

293. Gurrum, S.P., et al., *Size effect on the thermal conductivity of thin metallic films investigated by scanning joule expansion microscopy.* Journal of Heat Transfer-Transactions of the Asme, 2008. **130**(8).

294. Fletcher, P.C., B. Lee, and W.P. King, *Thermoelectric voltage at a nanometer-scale heated tip point contact.* Nanotechnology, 2012. **23**(3).

295. Gotsmann, B. and M.A. Lantz, *Quantized thermal transport across contacts of rough surfaces.* Nature Materials, 2013. **12**(1): p. 59-65.

296. Goodson, K.E. and M. Asheghi, *Near-field optical thermometry.* Microscale Thermophysical Engineering, 1997. **1**(3): p. 225-235.

297. Chapuis, P.O., et al., *Heat transfer between a nano-tip and a surface.* Nanotechnology, 2006. **17**(12): p. 2978-2981.

298. Chen, X.W. and X.W. Wang, *Near-field thermal transport in a nanotip under laser irradiation.* Nanotechnology, 2011. **22**(7).

299. Luo, K., et al., *Sensor nanofabrication, performance, and conduction mechanisms in scanning thermal microscopy.* Journal of Vacuum Science & Technology B, 1997. **15**(2): p. 349-360.

300. Leinhos, T., M. Stopka, and E. Oesterschulze, *Micromachined fabrication of Si cantilevers with Schottky diodes integrated in the tip.* Applied Physics a-Materials Science & Processing, 1998. **66**: p. S65-S69.

301. Mihalcea, C., A. Vollkopf, and E. Oesterschulze, *Reproducible large-area microfabrication of sub-100 nm apertures on hollow tips.* Journal of the Electrochemical Society, 2000. **147**(5): p. 1970-1972.

302. Shi, L., et al., *Design and batch fabrication of probes for sub-100 nm scanning thermal microscopy.* Journal of Microelectromechanical Systems, 2001. **10**(3): p. 370-378.

303. Shi, L. and A. Majumdar, *Thermal transport mechanisms at nanoscale point contacts.* Journal of Heat Transfer-Transactions of the Asme, 2002. **124**(2): p. 329-337.

304. Grosse, K.L., et al., *Nanoscale Joule heating, Peltier cooling and current crowding at graphene-metal contacts.* Nature Nanotechnology, 2011. **6**(5): p. 287-290.

305. McConnell, A.D., S. Uma, and K.E. Goodson, *Thermal conductivity of doped polysilicon layers.* Journal of Microelectromechanical Systems, 2001. **10**(3): p. 360-369.

306. Mavrokefalos, A., et al., *Four-probe measurements of the in-plane thermoelectric properties of nanofilms.* Review of Scientific Instruments, 2007. **78**(3).

307. Jang, W.Y., et al., *Thickness-Dependent Thermal Conductivity of Encased Graphene and Ultrathin Graphite.* Nano Letters, 2010. **10**(10): p. 3909-3913.

308. Seol, J.H., et al., *Two-Dimensional Phonon Transport in Supported Graphene.* Science, 2010. **328**(5975): p. 213-216.

309. Yarali, M., et al., *Effects of Defects on the Temperature-Dependent Thermal Conductivity of Suspended Monolayer Molybdenum Disulfide Grown by Chemical Vapor Deposition.* Advanced Functional Materials, 2017. **27**(46).

310. Cahill, D.G., *Thermal-Conductivity Measurement from 30-K to 750-K - the 3-Omega Method.* Review of Scientific Instruments, 1990. **61**(2): p. 802-808.

311. Lee, S.M. and D.G. Cahill, *Heat transport in thin dielectric films.* Journal of Applied Physics, 1997. **81**(6): p. 2590-2595.

312. Chen, Z., et al., *Thermal contact resistance between graphene and silicon dioxide.* Applied Physics Letters, 2009. **95**(16).

313. Freitag, M., et al., *Energy Dissipation in Graphene Field-Effect Transistors.* Nano Letters, 2009. **9**(5): p. 1883-1888.

314. Beechem, T., L. Yates, and S. Graham, *Invited Review Article: Error and uncertainty in Raman thermal conductivity measurements.* Review of Scientific Instruments, 2015. **86**(4).

315. Deem, H.W. and W.D. Wood, *Flash Thermal-Diffusivity Measurements Using a Laser.* Review of Scientific Instruments, 1962. **33**(10): p. 1107-&.

316. Guo, J.Q., X.W. Wang, and T. Wang, *Thermal characterization of microscale conductive and nonconductive wires using transient electrothermal technique.* Journal of Applied Physics, 2007. **101**(6).

317. Cahill, D.G., et al., *Nanoscale thermal transport.* Journal of Applied Physics, 2003. **93**(2): p. 793-818.

318. Hopkins, P.E., *Thermal Transport across Solid Interfaces with Nanoscale Imperfections: Effects of Roughness, Disorder, Dislocations, and Bonding on Thermal Boundary Conductance.* ISRN Mechanical Engineering, 2013. **2013**: p. 19.

319. Koh, Y.K., et al., *Comparison of the 3 omega method and time-domain thermoreflectance for measurements of the cross-plane thermal conductivity of epitaxial semiconductors.* Journal of Applied Physics, 2009. **105**(5).

320. Malen, J.A., et al., *Optical Measurement of Thermal Conductivity Using Fiber Aligned Frequency Domain Thermoreflectance.* Journal of Heat Transfer-Transactions of the Asme, 2011. **133**(8).

321. Yang, J., C. Maragliano, and A.J. Schmidt, *Thermal property microscopy with frequency domain thermoreflectance.* Review of Scientific Instruments, 2013. **84**(10).

322. Regner, K.T., S. Majumdar, and J.A. Malen, *Instrumentation of broadband frequency domain thermoreflectance for measuring thermal conductivity accumulation functions.* Review of Scientific Instruments, 2013. **84**(6).

323. Paddock, C.A. and G.L. Eesley, *Transient Thermoreflectance from Thin Metal-Films.* Journal of Applied Physics, 1986. **60**(1): p. 285-290.

324. Clemens, B.M., G.L. Eesley, and C.A. Paddock, *Time-Resolved Thermal Transport in Compositionally Modulated Metal-Films.* Physical Review B, 1988. **37**(3): p. 1085-1096.

325. Capinski, W.S. and H.J. Maris, *Improved apparatus for picosecond pump-and-probe optical measurements.* Review of Scientific Instruments, 1996. **67**(8): p. 2720-2726.

326. Cahill, D.G., *Analysis of heat flow in layered structures for time-domain thermoreflectance.* Review of Scientific Instruments, 2004. **75**(12): p. 5119-5122.

327. Chiritescu, C., et al., *Ultralow thermal conductivity in disordered, layered WSe2 crystals.* Science, 2007. **315**(5810): p. 351-353.

328. Koh, Y.K. and D.G. Cahill, *Frequency dependence of the thermal conductivity of semiconductor alloys.* Physical Review B, 2007. **76**(7).

329. Schmidt, A.J., X.Y. Chen, and G. Chen, *Pulse accumulation, radial heat conduction, and anisotropic thermal conductivity in pump-probe transient thermoreflectance.* Review of Scientific Instruments, 2008. **79**(11).

330. Minnich, A.J., et al., *Thermal Conductivity Spectroscopy Technique to Measure Phonon Mean Free Paths.* Physical Review Letters, 2011. **107**(9).

331. Wilson, R.B. and D.G. Cahill, *Anisotropic failure of Fourier theory in time-domain thermoreflectance experiments.* Nature Communications, 2014. **5**.

332. Koh, Y.K., et al., *Heat-Transport Mechanisms in Superlattices.* Advanced Functional Materials, 2009. **19**(4): p. 610-615.

333. Luckyanova, M.N., et al., *Coherent Phonon Heat Conduction in Superlattices.* Science, 2012. **338**(6109): p. 936-939.

334. Ravichandran, J., et al., *Crossover from incoherent to coherent phonon scattering in epitaxial oxide superlattices.* Nature Materials, 2014. **13**(2): p. 168-172.

335. Cheaito, R., et al., *Interplay between total thickness and period thickness in the phonon thermal conductivity of superlattices from the nanoscale to the microscale: Coherent versus incoherent phonon transport.* Physical Review B, 2018. **97**(8).

336. Cahill, D.G., K.E. Goodson, and A. Majumdar, *Thermometry and thermal transport in micro/nanoscale solid-state devices and structures.* Journal of Heat Transfer-Transactions of the Asme, 2002. **124**(2): p. 223-241.

337. Feser, J.P. and D.G. Cahill, *Probing anisotropic heat transport using time-domain thermoreflectance with offset laser spots.* Review of Scientific Instruments, 2012. **83**(10).

338. Feser, J.P., J. Liu, and D.G. Cahill, *Pump-probe measurements of the thermal conductivity tensor for materials lacking in-plane symmetry.* Review of Scientific Instruments, 2014. **85**(10).

339. Jiang, P.Q., X. Qian, and R.G. Yang, *Time-domain thermoreflectance (TDTR) measurements of anisotropic thermal conductivity using a variable spot size approach.* Review of Scientific Instruments, 2017. **88**(7).

340. Jiang, P.Q., X. Qian, and R.G. Yang, *A new elliptical-beam method based on time-domain thermoreflectance (TDTR) to measure the in-plane anisotropic thermal conductivity and its comparison with the beam-offset method.* Review of Scientific Instruments, 2018. **89**(9).

341. Thomsen, C., H.J. Maris, and J. Tauc, *Picosecond Acoustics as a Non-Destructive Tool for the Characterization of Very Thin-Films.* Thin Solid Films, 1987. **154**(1-2): p. 217-223.

342. Grahn, H.T., H.J. Maris, and J. Tauc, *Picosecond Ultrasonics.* Ieee Journal of Quantum Electronics, 1989. **25**(12): p. 2562-2569.

343. Tas, G., et al., *Picosecond ultrasonics study of the modification of interfacial bonding by ion implantation.* Applied Physics Letters, 1998. **72**(18): p. 2235-2237.

344. Schmidt, A., et al., *An optical pump-probe technique for measuring the thermal conductivity of liquids.* Review of Scientific Instruments, 2008. **79**(6).

345. Sun, B. and Y.K. Koh, *Understanding and eliminating artifact signals from diffusely scattered pump beam in measurements of rough samples by time-domain thermoreflectance (TDTR).* Review of Scientific Instruments, 2016. **87**(6).

346. Press, W.H., *Numerical recipes : the art of scientific computing*. 3rd ed. 2007, Cambridge, UK ; New York: Cambridge University Press. xxi, 1235 p.

347. Bougher, T.L., et al., *Thermal Boundary Resistance in GaN Films Measured by Time Domain Thermoreflectance with Robust Monte Carlo Uncertainty Estimation.* Nanoscale and Microscale Thermophysical Engineering, 2016. **20**(1): p. 22-32.

348. Yang, J., E. Ziade, and A.J. Schmidt, *Uncertainty analysis of thermoreflectance measurements.* Review of Scientific Instruments, 2016. **87**(1).

349. Brown, D.B., et al., *Oxidation limited thermal boundary conductance at metal-graphene interface.* Carbon, 2018. **139**: p. 913-921.

350. Carslaw, H.S. and J.C. Jaeger, *Conduction of heat in solids*. 2nd ed. 1986, Oxford Oxfordshire

New York: Clarendon Press ;

Oxford University Press. viii, 510 p.

351. Poularikas, A.D., *The handbook of formulas and tables for signal processing*. The electrical engineering handbook series. 1999, Boca Raton, Fla.

New York, NY: CRC Press ;

Springer : IEEE Press.

352. Feldman, A., *Algorithm for solutions of the thermal diffusion equation in a stratified medium with a modulated heating source.* High Temperatures-High Pressures, 1999. **31**(3): p. 293-298.

353. Hopkins, P.E., et al., *Criteria for Cross-Plane Dominated Thermal Transport in Multilayer Thin Film Systems During Modulated Laser Heating.* Journal of Heat Transfer-Transactions of the Asme, 2010. **132**(8).

354. Huxtable, S.T., D.G. Cahill, and L.M. Phinney, *Thermal contact conductance of adhered microcantilevers.* Journal of Applied Physics, 2004. **95**(4): p. 2102-2108.

355. Huxtable, S., et al., *Thermal conductivity imaging at micrometre-scale resolution for combinatorial studies of materials.* Nature Materials, 2004. **3**(5): p. 298-301.

356. O'Hara, K.E., X.Y. Hu, and D.G. Cahill, *Characterization of nanostructured metal films by picosecond acoustics and interferometry.* Journal of Applied Physics, 2001. **90**(9): p. 4852-4858.

357. Chernatynskiy, A. and S.R. Phillpot, *Phonon-mediated thermal transport: Confronting theory and microscopic simulation with experiment.* Current Opinion in Solid State & Materials Science, 2013. **17**(1): p. 1-9.

358. Volz, S.G. and G. Chen, *Molecular dynamics simulation of thermal conductivity of silicon nanowires.* Applied Physics Letters, 1999. **75**(14): p. 2056-2058.

359. Berber, S., Y.K. Kwon, and D. Tomanek, *Unusually high thermal conductivity of carbon nanotubes.* Physical Review Letters, 2000. **84**(20): p. 4613-4616.

360. Hu, J.N., X.L. Ruan, and Y.P. Chen, *Thermal Conductivity and Thermal Rectification in Graphene Nanoribbons: A Molecular Dynamics Study.* Nano Letters, 2009. **9**(7): p. 2730-2735.

361. Chen, L., X.J. Wang, and S. Kumar, *Thermal Transport in Fullerene Derivatives Using Molecular Dynamics Simulations.* Scientific Reports, 2015. **5**.

362. Henry, A.S. and G. Chen, *Spectral phonon transport properties of silicon based on molecular dynamics Simulations and lattice dynamics.* Journal of Computational and Theoretical Nanoscience, 2008. **5**(2): p. 141-152.

363. Lindsay, L. and D.A. Broido, *Optimized Tersoff and Brenner empirical potential parameters for lattice dynamics and phonon thermal transport in carbon nanotubes and graphene.* Physical Review B, 2010. **81**(20).

364. Wei, Z.Y., Y.F. Chen, and C. Dames, *Negative correlation between in-plane bonding strength and cross-plane thermal conductivity in a model layered material.* Applied Physics Letters, 2013. **102**(1).

365. Prasher, R., *Acoustic mismatch model for thermal contact resistance of van der Waals contacts.* Applied Physics Letters, 2009. **94**(4).

366. Prasher, R.S. and P.E. Phelan, *A scattering-mediated acoustic mismatch model for the prediction of thermal boundary resistance.* Journal of Heat Transfer-Transactions of the Asme, 2001. **123**(1): p. 105-112.

367. Little, W.A., *The Transport of Heat between Dissimilar Solids at Low Temperatures.* Canadian Journal of Physics, 1959. **37**(3): p. 334-349.

368. Reddy, P., K. Castelino, and A. Majumdar, *Diffuse mismatch model of thermal boundary conductance using exact phonon dispersion.* Applied Physics Letters, 2005. **87**(21).

369. Beechem, T., et al., *Role of interface disorder on thermal boundary conductance using a virtual crystal approach.* Applied Physics Letters, 2007. **90**(5).

370. Hopkins, P.E., et al., *Effects of surface roughness and oxide layer on the thermal boundary conductance at aluminum/silicon interfaces.* Physical Review B, 2010. **82**(8).

371. Hopkins, P.E., J.C. Duda, and P.M. Norris, *Anharmonic Phonon Interactions at Interfaces and Contributions to Thermal Boundary Conductance.* Journal of Heat Transfer-Transactions of the Asme, 2011. **133**(6).

372. Dames, C. and G. Chen, *Theoretical phonon thermal conductivity of Si/Ge superlattice nanowires.* Journal of Applied Physics, 2004. **95**(2): p. 682-693.

373. Snyder, N.S., *Heat Transport through Helium .2. Kapitza Conductance.* Cryogenics, 1970. **10**(2): p. 89-&.

374. Monachon, C., et al., *Qualitative link between work of adhesion and thermal conductance of metal/diamond interfaces.* Journal of Applied Physics, 2014. **115**(12).

375. Debye, P., *The theory of specific warmth.* Annalen Der Physik, 1912. **39**(14): p. 789-839.

376. Chen, G. and T.F. Zeng, *Nonequilibrium phonon and electron transport in heterostructures and superlattices.* Microscale Thermophysical Engineering, 2001. **5**(2): p. 71-88.

377. Duda, J.C., et al., *Extension of the diffuse mismatch model for thermal boundary conductance between isotropic and anisotropic materials.* Applied Physics Letters, 2009. **95**(3).

378. Auld, B.A., *Acoustic fields and waves in solids*. 2nd ed.. ed. 1990, Malabar, Fla.: Malabar, Fla. : R.E. Krieger.

379. Li, H.K., W.D. Zheng, and Y.K. Koh, *Anisotropic model with truncated linear dispersion for lattice and interfacial thermal transport in layered materials*. Physical Review Materials, 2018. **2**(12).

380. Liu, N., et al., *The Origin of Wrinkles on Transferred Graphene.* Nano Research, 2011. **4**(10): p. 996-1004.

381. Li, X.S., et al., *Large-Area Synthesis of High-Quality and Uniform Graphene Films on Copper Foils.* Science, 2009. **324**(5932): p. 1312-1314.

382. Pirkle, A., et al., *The effect of chemical residues on the physical and electrical properties of chemical vapor deposited graphene transferred to SiO2.* Applied Physics Letters, 2011. **99**(12).

383. Lin, Y.C., et al., *Graphene Annealing: How Clean Can It Be?* Nano Letters, 2012. **12**(1): p. 414-419.

384. Friebertshauser, P.E. and J.W. Mccamont, *Electrical Properties of Titanium Zirconium and Hafnium Films from 300 Degrees K to 1.3 Degrees K.* Journal of Vacuum Science & Technology, 1969. **6**(1): p. 184-+.

385. Singh, B. and N.A. Surplice, *Electrical Resistivity and Resistance-Temperature Characteristics of Thin Titanium Films.* Thin Solid Films, 1972. **10**(2): p. 243-&.

386. Ferrari, A.C., et al., *Raman spectrum of graphene and graphene layers.* Physical Review Letters, 2006. **97**(18).

387. Tuinstra, F. and J.L. Koenig, *Raman Spectrum of Graphite.* Journal of Chemical Physics, 1970. **53**(3): p. 1126-&.

388. Ferrari, A.C. and J. Robertson, *Interpretation of Raman spectra of disordered and amorphous carbon.* Physical Review B, 2000. **61**(20): p. 14095-14107.

389. Cancado, L.G., et al., *Quantifying Defects in Graphene via Raman Spectroscopy at Different Excitation Energies.* Nano Letters, 2011. **11**(8): p. 3190-3196.

390. Ashcroft, N.W. and N.D. Mermin, *Solid state physics*. 1976, New York,: Holt. xxi, 826 p.

391. Nan, C.W., et al., *Effective thermal conductivity of particulate composites with interfacial thermal resistance.* Journal of Applied Physics, 1997. **81**(10): p. 6692-6699.

392. Kumar, G.S., G. Prasad, and R.O. Pohl, *Experimental Determinations of the Lorenz Number.* Journal of Materials Science, 1993. **28**(16): p. 4261-4272.

393. McCafferty, E. and J.P. Wightman, *An X-ray photoelectron spectroscopy sputter profile study of the native air-formed oxide film on titanium.* Applied Surface Science, 1999. **143**(1-4): p. 92-100.

394. Jablonski, C.J.P.a.A., *NIST Electron Inelastic-Mean-Free-Path Database - Version 1.2*. 2010, Gaithersburg, MD: National Institute of Standards and Technology.

395. Gries, W.H., *A universal predictive equation for the inelastic mean free pathlengths of x-ray photoelectrons and Auger electrons.* Surface and Interface Analysis, 1996. **24**(1): p. 38-50.

396. Nesbitt, H.W., D. Legrand, and G.M. Bancroft, *Interpretation of Ni2p XPS spectra of Ni conductors and Ni insulators.* Physics and Chemistry of Minerals, 2000. **27**(5): p. 357-366.

397. Strohmeier, B.R., *An Esca Method for Determining the Oxide Thickness on Aluminum-Alloys.* Surface and Interface Analysis, 1990. **15**(1): p. 51-56.

398. Payne, B.P., et al., *Structure and growth of oxides on polycrystalline nickel surfaces.* Surface and Interface Analysis, 2007. **39**(7): p. 582-592.

399. Biesinger, M.C., et al., *X-ray photoelectron spectroscopic chemical state quantification of mixed nickel metal, oxide and hydroxide systems.* Surface and Interface Analysis, 2009. **41**(4): p. 324-332.

400. Hammer, B. and J.K. Norskov, *Why Gold Is the Noblest of All the Metals.* Nature, 1995. **376**(6537): p. 238-240.

401. Zheng, W.D., et al., *Achieving Huge Thermal Conductance of Metallic Nitride on Graphene Through Enhanced Elastic and Inelastic Phonon Transmission.* Acs Applied Materials & Interfaces, 2018. **10**(41): p. 35487-35494.

402. Lee, S.M. and D.G. Cahill, *Influence of interface thermal conductance on the apparent thermal conductivity of thin films.* Microscale Thermophysical Engineering, 1997. **1**(1): p. 47-52.

403. Pandey, H.N., *The Theoretical Elastic Constants and Specific Heats of Rutile.* physica status solidi (b), 1965. **11**(2): p. 743-751.

404. George, P.K. and E.D. Thompson, *Debye Temperature of Nickel from 0 to 300 Degrees K.* Journal of Physics and Chemistry of Solids, 1967. **28**(12): p. 2539-&.

405. Coy, R.A., C.W. Tompson, and E. Gurmen, *Phonon Dispersion in Nio.* Solid State Communications, 1976. **18**(7): p. 845-847.

406. Leroy, W.P., et al., *Solid-state formation of titanium carbide and molybdenum carbide as contacts for carbon-containing semiconductors.* Journal of Applied Physics, 2006. **99**(6).

407. Huard, B., et al., *Evidence of the role of contacts on the observed electron-hole asymmetry in graphene.* Physical Review B, 2008. **78**(12).

408. Politou, M., et al., *Transition metal contacts to graphene.* Applied Physics Letters, 2015. **107**(15).

409. Nemanich, R.J. and S.A. Solin, *1st-Order and 2nd-Order Raman-Scattering from Finite-Size Crystals of Graphite.* Physical Review B, 1979. **20**(2): p. 392-401.

410. Yan, J., et al., *Electric field effect tuning of electron-phonon coupling in graphene.* Physical Review Letters, 2007. **98**(16).

411. Das, A., et al., *Monitoring dopants by Raman scattering in an electrochemically top-gated graphene transistor.* Nature Nanotechnology, 2008. **3**(4): p. 210-215.

412. Geick, R., C.H. Perry, and Rupprech.G, *Normal Modes in Hexagonal Boron Nitride.* Physical Review, 1966. **146**(2): p. 543-&.

413. Nemanich, R.J., S.A. Solin, and R.M. Martin, *Light-Scattering Study of Boron-Nitride Micro-Crystals.* Physical Review B, 1981. **23**(12): p. 6348-6356.

414. Arenal, R., et al., *Raman spectroscopy of single-wall boron nitride nanotubes.* Nano Letters, 2006. **6**(8): p. 1812-1816.

415. Song, L., et al., *Large Scale Growth and Characterization of Atomic Hexagonal Boron Nitride Layers.* Nano Letters, 2010. **10**(8): p. 3209-3215.

416. Chiu, M.H., et al., *Spectroscopic Signatures for Interlayer Coupling in MoS2-WSe2 van der Waals Stacking.* Acs Nano, 2014. **8**(9): p. 9649-9656.

417. Lui, C.H., et al., *Observation of interlayer phonon modes in van der Waals heterostructures.* Physical Review B, 2015. **91**(16).

418. Wang, K., et al., *Interlayer Coupling in Twisted WSe2/WS2 Bilayer Heterostructures Revealed by Optical Spectroscopy.* ACS Nano, 2016. **10**(7): p. 6612-6622.

419. Jin, C., et al., *Interlayer electron-phonon coupling in WSe2/hBN heterostructures.* Nat Phys, 2017. **13**(2): p. 127-131.

420. Smith, G.C., *Surface analysis by electron spectroscopy measurement and interpretation*, in *Updates in applied physics and electrical technology*. 1994, Plenum Press,: New York. p. 1 online resource (xi, 156 pages).

421. Xinxia, L., et al., *Thermal conduction across a boron nitride and SiO 2 interface.* Journal of Physics D: Applied Physics, 2017. **50**(10): p. 104002.

422. Aljishi, R. and G. Dresselhaus, *Lattice-Dynamical Model for Graphite.* Physical Review B, 1982. **26**(8): p. 4514-4522.

423. Bosak, A., et al., *Elasticity of hexagonal boron nitride: Inelastic x-ray scattering measurements.* Physical Review B, 2006. **73**(4).

424. Stassis, C., et al., *Lattice-Dynamics of Hcp-Ti.* Physical Review B, 1979. **19**(1): p. 181-188.

425. Serrano, J., et al., *Vibrational properties of hexagonal boron nitride: Inelastic X-ray scattering and ab initio calculations.* Physical Review Letters, 2007. **98**(9).

426. Li, H., W. Zheng, and Y. Kan Koh *Anisotropic model with truncated linear dispersion for lattice and interfacial thermal transport in layered materials*. ArXiv e-prints, 2018.

427. Chen, G., *Thermal conductivity and ballistic-phonon transport in the cross-plane direction of superlattices.* Physical Review B, 1998. **57**(23): p. 14958-14973.

428. Wolfe, J.P., *Imaging phonons : acoustic wave propagation in solids*. 1998, Cambridge, U.K. ; New York: Cambridge University Press. xiii, 411 p.

429. Tohei, T., et al., *Debye temperature and stiffness of carbon and boron nitride polymorphs from first principles calculations.* Physical Review B, 2006. **73**(6).

430. Li, X.F., et al., *Isoelectronic Tungsten Doping in Monolayer MoSe2 for Carrier Type Modulation.* Advanced Materials, 2016. **28**(37): p. 8240-8247.

431. Li, X.F., et al., *Suppression of Defects and Deep Levels Using Isoelectronic Tungsten Substitution in Monolayer MoSe2.* Advanced Functional Materials, 2017. **27**(19).

432. Cheaito, R., et al., *Thermal boundary conductance accumulation and interfacial phonon transmission: Measurements and theory.* Physical Review B, 2015. **91**(3).

433. Humbert, A., et al., *Low energy interband transitions in aluminium.* J. Physique Lett., 1977. **38**(24): p. 479-481.

434. Castellanos-Gomez, A., N. Agrait, and G. Rubio-Bollinger, *Optical identification of atomically thin dichalcogenide crystals.* Applied Physics Letters, 2010. **96**(21).

435. Abdallah, W.A. and A.E. Nelson, *Characterization of MoSe2(0001) and ion-sputtered MoSe2 by XPS.* Journal of Materials Science, 2005. **40**(9-10): p. 2679-2681.

436. Sood, A., et al., *Direct Visualization of Thermal Conductivity Suppression Due to Enhanced Phonon Scattering Near Individual Grain Boundaries.* Nano Letters, 2018. **18**(6): p. 3466-3472.

437. Zhu, J., et al., *Ultrafast thermoreflectance techniques for measuring thermal conductivity and interface thermal conductance of thin films.* Journal of Applied Physics, 2010. **108**(9).

438. Cahill, D.G., M. Katiyar, and J.R. Abelson, *Thermal-Conductivity of Alpha-Sih Thin-Films.* Physical Review B, 1994. **50**(9): p. 6077-6081.

439. Collins, K.C., S. Chen, and G. Chen, *Effects of surface chemistry on thermal conductance at aluminum-diamond interfaces.* Applied Physics Letters, 2010. **97**(8).

440. Kanungo, T., et al., *An efficient k-means clustering algorithm: Analysis and implementation.* Ieee Transactions on Pattern Analysis and Machine Intelligence, 2002. **24**(7): p. 881-892.

441. Chung, D.H. and G. Simmons, *Pressure and Temperature Dependences of Isotropic Elastic Moduli of Polycrystalline Alumina.* Journal of Applied Physics, 1968. **39**(11): p. 5316-&.

442. Hu, S.Y., et al., *Temperature dependence of absorption edge anisotropy in 2H-MoSe2 layered semiconductors.* Solid State Communications, 2006. **139**(4): p. 176-180.

443. Kumar, S., et al., *Conduction Channel Formation and Dissolution Due to Oxygen Thermophoresis/Diffusion in Hafnium Oxide Memristors.* Acs Nano, 2016. **10**(12): p. 11205-11210.

444. Duda, J.C., et al., *Influence of interfacial properties on thermal transport at gold:silicon contacts.* Applied Physics Letters, 2013. **102**(8).

445. Kuo, C.T., R. Kwor, and K.M. Jones, *Study of Sputtered Hfo2 Thin-Films on Silicon.* Thin Solid Films, 1992. **213**(2): p. 257-264.

446. Teren, A.R., et al., *Comparison of precursors for pulsed metal-organic chemical vapor deposition of HFO2 high-K dielectric thin films.* Thin Solid Films, 2005. **478**(1-2): p. 206-217.

447. Luo, X.H. and A.A. Demkov, *Structure, thermodynamics, and crystallization of amorphous hafnia.* Journal of Applied Physics, 2015. **118**(12).

448. Lee, J.B. and S.H. Lee, *Thermal Boundary Resistance Effect on Non-Equilibrium Energy Transport in Metal-Dielectric Thin Films Heated by Femtosecond Pulse Lasers.* Materials Transactions, 2011. **52**(7): p. 1492-1499.

449. Lince, J.R., D.J. Carre, and P.D. Fleischauer, *Schottky-Barrier Formation on a Covalent Semiconductor without Fermi-Level Pinning - the Metal-Mos2(0001) Interface.* Physical Review B, 1987. **36**(3): p. 1647-1656.

450. English, C.D., et al., *Improved Contacts to MoS2 Transistors by Ultra-High Vacuum Metal Deposition.* Nano Letters, 2016. **16**(6): p. 3824-3830.

451. McDonnell, S., et al., *MoS2-Titanium Contact Interface Reactions.* Acs Applied Materials & Interfaces, 2016. **8**(12): p. 8289-8294.

452. Freedy, K.M., et al., *Unraveling Chemical Interactions between Titanium and Graphene for Electrical Contact Applications.* ACS Applied Nano Materials, 2018. **1**(9): p. 4828-4835.

453. Yan, R.S., et al., *Thermal Conductivity of Monolayer Molybdenum Disulfide Obtained from Temperature-Dependent Raman Spectroscopy.* Acs Nano, 2014. **8**(1): p. 986-993.

454. Liang, X.L., et al., *Toward Clean and Crackless Transfer of Graphene.* Acs Nano, 2011. **5**(11): p. 9144-9153.

455. Zhan, Y.J., et al., *Large-Area Vapor-Phase Growth and Characterization of MoS2 Atomic Layers on a SiO2 Substrate.* Small, 2012. **8**(7): p. 966-971.

456. Lee, Y.H., et al., *Synthesis of Large-Area MoS2 Atomic Layers with Chemical Vapor Deposition.* Advanced Materials, 2012. **24**(17): p. 2320-2325.

457. Ohta, T., et al., *Controlling the electronic structure of bilayer graphene.* Science, 2006. **313**(5789): p. 951-954.

458. Ji, Q.Q., et al., *Epitaxial Monolayer MoS2 on Mica with Novel Photoluminescence.* Nano Letters, 2013. **13**(8): p. 3870-3877.

459. Gong, Y.J., et al., *Band Gap Engineering and Layer-by-Layer Mapping of Selenium-Doped Molybdenum Disulfide.* Nano Letters, 2014. **14**(2): p. 442-449.

460. Li, H., et al., *Growth of Alloy MoS2xSe2(1–x) Nanosheets with Fully Tunable Chemical Compositions and Optical Properties.* Journal of the American Chemical Society, 2014. **136**(10): p. 3756-3759.

461. Mann, J., et al., *2-Dimensional Transition Metal Dichalcogenides with Tunable Direct Band Gaps: MoS2(1–x)Se2x Monolayers.* Advanced Materials, 2014. **26**(9): p. 1399-1404.

462. Yuan, H.T., et al., *Zeeman-type spin splitting controlled by an electric field.* Nature Physics, 2013. **9**(9): p. 563-569.

463. Suh, J., et al., *Doping against the Native Propensity of MoS2: Degenerate Hole Doping by Cation Substitution.* Nano Letters, 2014. **14**(12): p. 6976-6982.